

Understanding and improving ultrasonic inspection of jet-engine titanium alloy

by

Linxiao Yu

A dissertation submitted to the graduate faculty  
in partial fulfillment of the requirements for the degree of

DOCTOR OF PHILOSOPHY

Major: Materials Science and Engineering

Program of Study Committee:  
R. Bruce Thompson, Major Professor  
Scott Chumbley  
William Q. Meeker, Jr.  
Alan M. Russell  
Lester W. Schmerr, Jr.

Iowa State University

Ames, Iowa

2004

UMI Number: 3158386

### INFORMATION TO USERS

The quality of this reproduction is dependent upon the quality of the copy submitted. Broken or indistinct print, colored or poor quality illustrations and photographs, print bleed-through, substandard margins, and improper alignment can adversely affect reproduction.

In the unlikely event that the author did not send a complete manuscript and there are missing pages, these will be noted. Also, if unauthorized copyright material had to be removed, a note will indicate the deletion.

**UMI<sup>®</sup>**

---

UMI Microform 3158386

Copyright 2005 by ProQuest Information and Learning Company.

All rights reserved. This microform edition is protected against unauthorized copying under Title 17, United States Code.

ProQuest Information and Learning Company  
300 North Zeeb Road  
P.O. Box 1346  
Ann Arbor, MI 48106-1346

Graduate College  
Iowa State University

This is to certify that the doctoral dissertation of  
  
Linxiao Yu  
  
has met the dissertation requirements of Iowa State University

Signature was redacted for privacy.

**Committee Member**

Signature was redacted for privacy.

**Committee Member**

Signature was redacted for privacy.

**Committee Member**

Signature was redacted for privacy.

**Committee Member**

Signature was redacted for privacy.

**Major Professor**

Signature was redacted for privacy.

**For the Major Program**

## TABLE OF CONTENTS

ACKNOWLEDGEMENTS .....	v
ABSTRACT.....	vii
GENERAL INTRODUCTION.....	1
VARIABILITY OF THE BACKSCATTERED ULTRASONIC GRAIN NOISE IN Ti-6Al-4V FORGING.....	2
SPATIAL CORRELATION OF THE BACKSCATTERED ULTRASONIC GRAIN NOISE.....	4
MICROSTRUCTURE-INDUCED ULTRASONIC SIGNAL FLUCTUATIONS.....	5
DISSERTATION ORGANIZATION .....	7
REFERENCES .....	9
CHAPTER 1. A MODEL CORRELATING BACKSCATTERED ULTRASONIC GRAIN NOISE TO THE INHOMOGENEOUS PLASTIC DEFORMATION IN Ti-6Al-4V FORGING .....	15
ABSTRACT.....	15
1. INTRODUCTION .....	16
2. EXPERIMENTAL MOTIVATIONS .....	21
3. REVIEW OF THE THEORY .....	23
4. TWO-POINT CORRELATION OF ELASTIC CONSTANTS IN TEXTURED TWO-PHASE MICROSTRUCTURE.....	26
5. COMPARISON BETWEEN THEORY AND EXPERIMENT .....	29
6. SUMMARY AND CONCLUSION .....	33
ACKNOWLEDGEMENTS .....	34
REFERENCES .....	34
CHAPTER 2. THE SPATIAL CORRELATION OF THE BACKSCATTERED ULTRASONIC GRAIN NOISE: THEORY AND EXPERIMENTAL VALIDATION.....	49
ABSTRACT.....	49
1. INTRODUCTION .....	50
2. THEORY FOR BACKSCATTERED ULTRASONIC GRAIN NOISE SPATIAL CORRELATION.....	52

2. 1 THEORY IN GENERAL FORM .....	52
2. 2 THEORY FOR A GAUSSIAN BEAM.....	58
3. EXPERIMENTAL VALIDATION OF THE THEORY .....	60
3.1 DO GRAIN NOISE SPATIAL CORRELATIONS DEPEND ON THE DISTANCE FROM FOCAL PLANE?.....	60
3.2 HOW DO THE TRANSDUCER SPECTRAL CHARACTERISTICS AFFECT GRAIN NOISE SPATIAL CORRELATION?.....	62
3.3 HOW DO THE TRANSDUCER FOCAL PARAMETERS AFFECT GRAIN NOISE SPATIAL CORRELATION?.....	64
3.4 HOW DOES THE GRAIN SIZE AFFECT THE GRAIN NOISE SPATIAL CORRELATION?.....	64
4. DISCUSSION .....	65
5. SUMMARY .....	66
ACKNOWLEDGEMENTS .....	67
REFERENCES .....	67
APPENDIX: THEORY FOR BACKSCATTERED ULTRASONIC GRAIN NOISE SPATIAL CORRELATION .....	80
CHAPTER 3. MICROSTRUCTURE-INDUCED ULTRASONIC SIGNAL FLUCTUATIONS IN TITANIUM ALLOY .....	89
ABSTRACT.....	89
1. INTRODUCTION .....	90
2. MICROSTRUCTURE-INDUCED BEAM DISTORTIONS .....	92
3. MODELING APPROACH.....	94
3.1 PREDICTION OF P/E OF BACK-WALL SIGNAL USING THROUGH- TRANSMITTED FIELD .....	95
3.2 STATISTICAL VARIABLES CHARACTERIZING DISTORTED FIELDS .....	97
3.3 PREDICTION OF BACK-WALL SPECTRUM AMPLITUDE FLUCTUATION.....	102
4. COMPARISON BETWEEN THEORY AND EXPERIMENT .....	103
5. SIMULATION OF ULTRASONIC FLAW SIGNAL FLUCTUATIONS .....	104
6. SUMMARY AND FUTURE WORK .....	107
ACKNOWLEDGEMENTS .....	108
REFERENCES .....	108
GENERAL CONCLUSIONS.....	124

## ACKNOWLEDGEMENTS

I would like to express my deep gratitude for my advisor, Professor R. Bruce Thompson, who has guided, encouraged and supported me in many different ways during my Ph.D. study. With his excellent guidance and helpful suggestions, my research has come so far. I am very grateful that I had the opportunity to study under his supervision.

It was a distinct privilege to work with Dr. Frank J. Margetan over the past few years, during which time I learned a lot from him, not only various skills in ultrasonic NDE but also tricks to fix my old car. He contributed many helpful suggestions to my research. Everything would have been much harder without his supports.

I would also like to thank Dr. Lester W. Schmerr, Dr. William Q. Meeker, Dr. Alan M. Russell and Dr. Scott Chumbley for serving on my thesis committee and for many helpful comments and guidance on my research.

I am also grateful to many other faculty and staff members at the center for NDE and the department of MSE, especially Dr. David Cann, who gave me a lot help when I prepared my qualification examination; Dr. Kristen Constant, who served as my PFF (Preparing Future Faculty) mentor; Dr. David Hsu, Mr. John Peters and Mr. Daniel J. Barnard, for their help in my experiments.

Dr. Andrei Degtyar from United Technologies Pratt & Whitney provided the results of deformation simulation, which is one of the most important components for the modeling study in the Chapter 1 of this thesis. I sincerely appreciated his efforts.

I want to take this opportunity to thank many other people I have worked with. They have extended my knowledge and kindly offered me various help. Only a few are named here: Dr. Yanming Guo, Mr. Pranaam Haldipur, Mr. Anxiang Li, Mr. Jon Friedl and Dr. Hak-Joon Kim. I wish them all the best.

The time I spent with the Chinese Students and Scholars Friendship Association (CSSFA) at Ames is memorable. We worked together to celebrate Chinese festivals, to exchange our common concerns, and to help new comers. Special thanks go to Bingbing, Rujun, Finglei and Yu Lin.

Last but not least, I would like to thank my wife, Yurong Wang, and my daughter, Julia, for their continuous love and support. Very special thank you must go to my parents for their utmost supports and encouragements that have made me go this far.

## ABSTRACT

Commercial titanium alloy is widely used in the rotating components of aircraft engines. To ensure the safety and longer lifetime of these critical parts, the demand to detect smaller defects becomes more and more important. Ultrasonic inspection is a routine non-destructive evaluation (NDE) method adopted by the aircraft engine manufacturers. However, the detection of smaller defects in such materials is made difficult by the complicated ultrasound-microstructure interactions, such as the high backscattered grain noise levels and serious signal fluctuations. The high grain noise acts to mask small flaw signals and severe signal fluctuations may cause confusions in flaw detection or characterization. The objective of this research is to develop a more complete understanding of these phenomena to guide solutions that would address those problems.

In Chapter 1, the relationships between ultrasonic properties (velocity, attenuation, and backscattered grain noise) and the microstructure are investigated for a series of specimens cut from representative Ti-6Al-4V forgings. Close correlation between the ultrasonic properties and the forging deformation parameters are observed. A model was developed to correlate backscattered grain noise levels with microstructural variations that arise from the inhomogeneous plastic deformation during forging. The microstructural information include the global average grain volume, local grain elongation, local grain orientation relative to the incident beam and the local texture. The model is used to predict the FOM (Figure of Merit), GPN (Gated-Peak-Noise) and the noise angular dependence in the forging specimens. In all cases, the experiments and predictions agree reasonably well.

The spatial correlation of backscattered ultrasonic grain noise has important implications in practical inspections. In Chapter 2 of this thesis, an existing backscattered grain noise theory based on the single scattering assumption and the “Born” approximation is extended, leading to a formal theory predicting the spatial correlation of the backscattered grain noise.



A special form of the theory for a Gaussian beam is also presented to demonstrate that the material microstructure and the overlap of the incident beam are the important physical parameters controlling the grain noise spatial correlation. To validate the theory, a series of experiments are designed to collect grain noise signals from a waspalloy alloy specimen, which has locally-uniform equiaxed microstructure. The theory is numerically evaluated and the results are compared with the experiments. Excellent agreements between predictions and measurements are observed.

Ultrasonic signal fluctuations in billet titanium alloys (Ti-6Al-4V and Ti-5Al-2Sn-2Zr-4Cr-4Mo) are studied in Chapter 3. The microstructure-induced beam distortions are first explicitly demonstrated, including two types of amplitude distortion: the lateral “drift” of the center-of-energy about its expected position; the distortion of pressure amplitude about its expected pattern; and two types of wave-front distortion (“wrinkling” and “tilting”). An analytical relationship is then derived to correlate the back-wall P/E spectrum at one transducer location to the through-transmitted field. Based on the analytical relationship and the statistical descriptions of various beam distortion effects, a quantitative Monte-Carlo model is developed to predict the back-wall amplitude fluctuations seen in ultrasonic P/E inspections. The modeling approach is demonstrated on specimens of jet-engine titanium alloys, and predicted back-wall fluctuation levels at 3 frequencies for both planar and focused transducer are shown to be in good agreements with experiments. In the last section of this Chapter, the same modeling approach is used to simulate the flaw (small reflector) signal fluctuation. The predicted fluctuation levels are compared with that deduced from the simulated data, which was generated by an independent modeling study. Qualitative agreements are observed. As a novel way of modeling ultrasonic signal fluctuations, the approach outlined in this paper suggests many possibilities for future research.

## GENERAL INTRODUCTION

Commercial titanium alloy is widely used in the rotating components of aircraft engines. To ensure the safety and longer lifetime of these critical parts, the demand to detect smaller defects becomes more and more important. Ultrasonic inspection is a routine NDE method adopted by the aircraft engine manufacturers. However, the detection of smaller defects in such materials is made difficult by the complicated ultrasound-microstructure interactions. One of the adverse influences of the interactions is the high backscattered grain noise level accompanying with the ultrasonic inspections of some titanium alloys. The high grain noise deteriorates the signal to noise ratio (S/N) of pulse/echo inspections and consequently may lead to the missing detection of an existing flaw. This grain noise will be correlated in space, since a small translation of the transducer will only cause a small change in the noise signals whereas a large translation can lead to totally independent noise signals. The details of grain noise spatial correlation are important components in the practical inspections, for example in de-noising image processing. The other adverse influence of ultrasound-microstructure interactions is the microstructure-induced signal fluctuations. For example, nominally-identical standard defects, such as arrays of flat-bottom-holes (FBH) located at a given depth, can have quite different responses in the inspection. Ultrasonic signal fluctuations have direct impact on flaw detection, flaw characterization and the estimation of the probability of detection (POD).

The objective of this research is to develop a more complete understanding of these phenomena and to guide solutions that would improve the inspections of jet-engine titanium alloy. Specifically, this thesis covers the following three research topics: the experimental and model studies of the ultrasonic properties variations in Ti-6Al-4V forging, with the emphasis on the backscattered ultrasonic grain noise; the theoretical investigation of the spatial correlation of the backscattered ultrasonic grain noise and the experimental validation

of the theory; and the experimental and model studies of the microstructure-induced signal fluctuations. The detailed discussion for each research topic is given below.

## **VARIABILITY OF THE BACKSCATTERED ULTRASONIC GRAIN NOISE IN Ti-6Al-4V FORGING**

The microstructure influences ultrasonic pulse/echo inspections in three basic ways: (1) the attenuation of sound energy acts to decrease the amplitude of echoes from possible defects; (2) backscattered noise from grain boundaries acts to mask echoes from small or subtle flaws; and (3) velocity inhomogeneities cause distortions of propagating sound beams, which in turn lead to fluctuations in echo amplitudes. As one of the sub-tasks of the Engine Titanium Consortium (ETC) project, which was initialized to improve the Ti-6Al-4V forging inspections, we carried out an experimental investigation [1, 2] of the ultrasonic properties of representative titanium forgings. The goal of our research was to gain the fundamental understanding of the ultrasonic properties (velocity, attenuation, backscattered grain noise) of titanium forgings and document the manner in which the material ultrasonic properties depend upon position and inspection direction. The experimental investigation laid out a foundation to guide the development and application of improved inspection systems. Additional efforts were made to model the variability of the backscattered grain noise throughout the forging, which provides a basis for the development of algorithms to interpret the received signals, and to quantify the inspection capability, for example, to determine POD.

Backscattering is a fundamental character of ultrasonic wave propagation in polycrystalline materials. The backscattered ultrasonic grain noise in a polycrystalline material is caused by the mismatches of the acoustic properties along the grain boundaries in the material. The mismatches are primarily associated with the anisotropy of the elastic constants in grains or crystallites. Because of the important implications in NDE and

materials characterization, backscattered ultrasonic grain noise has been an active research topic in the past decade in the NDE community [1-22]. The theoretical foundation for the backscattered ultrasonic grain noise was laid out by Rose [3-5], which relates backscattered ultrasonic grain noise levels to the physical properties of the microstructure. Using a single-scattering assumption and the “Born” approximation, Rose developed a rigorous stochastic theory for the backscattered noise power, which led to explicit expressions for backscattering in randomly orientated, equiaxed, single-phase or multi-phase polycrystals. Han and Thompson’s work [11, 12] extended Rose’s theory to the case of duplex microstructures, which may contain texture and elongated microstructural features with correlations in grain orientation. The experimental measurement model for the backscattered ultrasonic grain noise was developed by Margetan et al. [6-10]. They modeled the received backscattered grain noise power to be equal to the sum of the power backscattered from the individual crystallites, by assuming that the phases of these signals would be random. In this model, they defined a characteristic material parameter, the so-called “figure of merit (*FOM*)”, to measure the noise generation capability of the material, which was shown to be identical to the square root of the backscattering coefficient ( $\eta$ ) used in Rose’s paper [3-5].

According to the grain noise theory [3-5, 11, 12], the total backscattering is controlled by grain morphology, grain orientation and elastic anisotropy, which may vary throughout the microstructure. Thus any thermo-mechanical processing (TMP) leading to the variations of material microstructure may influence the backscattered grain noise. Through their manufacturing processing, aircraft forging disks typically experience heavy inhomogeneous plastic deformation; for example, the strain magnitude and metal flow direction vary substantially at different locations within the forging disks of interest. We expect that the microstructure in the forging varies with location, such as the grain elongation, grain orientation relative to the incident beam and the local texture [23-29]. All of the above mentioned microstructure characteristics can greatly affect the measured grain noise. In this

part of our research, we give a review of our experimental investigations and demonstrate that the measured grain noise signals have close correlations with the deformation parameters. We developed new ideas of how to extract useful microstructural information from the forging simulation software, DEFORM<sup>TM</sup>, a commercial software package produced by Scientific Forming Technologies Corporation, Columbus, Ohio. A model is then developed to correlate the grain noise signals with the microstructural variations due to the inhomogeneous plastic deformation associated with the forging processing. The grain noise levels predicted by the model at various locations are compared with experiments. Reasonably good agreements are observed.

## **SPATIAL CORRELATION OF THE BACKSCATTERED ULTRASONIC GRAIN NOISE**

One of the interesting outcomes of the complicated ultrasound-microstructure interactions is that the backscattered ultrasonic grain noise signals have evident correlations in space. For example, a routine industrial UT (ultrasonic testing) operation for aircraft engine billet inspection is to make ultrasonic C-scan images composed of spatial maps of Gated-Peak-Signals. The collected images have clear “high-noise” and “low-noise” bands over the billet circumferential direction [30, 31].

The noise spatial correlation quantifies the semblance or coherency between the noise waveforms at different spatial coordinates. For a homogeneous microstructure, the grain noise spatial correlation intuitively depends on the diameter of the incident beam, i.e., the larger beam size, the larger distance one has to move the incident beam from the previous transducer position to insonify a sufficient different grain aggregate to obtain a “different” signal. However, the experimental investigations on the backscattered grain noise from titanium forging [32] and backscattered ultrasonic signals from porosities in casting aluminum [33] indicate the spatial correlation length (SCL) of the backscattered signal is

much smaller than the beam diameter. This implies there are other important physical parameters controlling the spatial correlation of the backscattered signals.

The spatial correlation of backscattered ultrasonic grain noise has important implications in practical ultrasonic inspections. For example, the spatial correlation of the backscattered grain noise is a crucial component in designing advanced de-noising algorithm in image processing [34, 35], and the grain noise SCL is a crucial quantity in some critical simulations [2] to evaluate the distribution of the gated-peak noise (GPN), which in turn is indispensable for the estimation of POD or frequency of false calls [36-38]. To understand the experimental mystery and to get more details of the spatial correlation of the backscattered grain noise, it is desirable to have a physics-based modeling tool to predict the grain noise spatial correlation of different inspection scenarios.

In this part of our research, we extended the existing backscattered grain noise theory [3-5, 11, 12] to study the correlation, leading to a formal theory to predict the spatial correlation of the backscattered grain noise in different experimental circumstances. The theory was derived in its general form and also presented in a special form for a Gaussian beam. The theory indicates, for a given inspection system, that the material microstructure and the overlap of the incident sound field (both the amplitude and phase profiles) are the important controlling physical parameters for the spatial correlation of the backscattered grain noise. The theory is numerically evaluated and the results are compared with the measurements. Excellent agreements between the predictions and experiments are observed.

## **MICROSTRUCTURE-INDUCED ULTRASONIC SIGNAL FLUCTUATIONS**

Jet-engine titanium alloy typically has duplex microstructure containing features with different scales. The large-scale components, the so called “macrograins”, have large dimensions compared to the incident sonic wavelength [17, 39, 40]. Differences in the average ultrasonic velocities between neighboring macrograins act to significantly distort the

amplitude and phase profiles of the incident sonic beam. As a result, these distortions can lead to large ultrasonic signal fluctuations in some circumstances [39-42]. For example, in pulse/echo (P/E) inspections, the measured ultrasonic signals from nominally-identical standard defects, such as arrays of flat-bottom-holes (FBH) located at a given depth, can change dramatically at different locations. Similarly, when we scan a transducer parallel to the surface of a flat titanium billet specimen, the received back-wall signals can vary significantly.

The stochastic nature of the ultrasonic response has obvious implications in practical non-destructive testing/evaluation (NDT/E). Back-wall signal fluctuation may lead to inaccuracy in the DAC (Distance-amplitude-correction) when using back wall signal to estimate the attenuation difference between the calibration standard and the part to be inspected. The flaw signal fluctuations may broaden the flaw signal distribution curve in the estimation of probability of detection (POD) [37, 38]. Because of the flaw signal fluctuation, a weak flaw signal may be caused by a defect as dangerous as one producing a strong flaw signal.

The microstructure-induced ultrasonic signal fluctuations in jet-engine titanium alloys have been investigated by several researchers. The experimental investigations by Panetta and Margetan et. al. [17, 30, 39-41] documented the fluctuation phenomena in a jet-engine titanium alloy for both the FBH and back-wall signal. By comparing the attenuation measured by pulse/echo and pitch/catch methods, they concluded that the ultrasonic signal fluctuations in jet-engine titanium are the results of microstructure-induced phase aberration of the incident beam. They also demonstrated that the signal fluctuation levels have close correlation with the beam focal conditions inside the metal specimen. The ray model developed by Margetan et. al. [42] confirmed that the back-wall fluctuation arising from beam distortions can be quantitatively related to the velocity inhomogeneities in a Ti-6Al-4V sample with enlarged grain. The numerical simulations of the influences of the inhomogeneities on the incident ultrasonic beam, performed by Roberts, Ahmed and Li, et. al

[43-46], provided many physical insights into this problem. Particularly, the simulation study carried out by Li et. al. [46] provided the statistical information regarding the various beam distortion effects produced by different microstructures. The statistical information regarding the various beam distortion effects are key parameters to be used in our work.

In this part of our research, we first explicitly demonstrate various beam distortions induced by the microstructure, i.e., two types of amplitude distortion: the lateral “drift” of the center-of-energy about its expected position; the distortion of pressure amplitude about its expected pattern; and two types of wave-front distortion (“wrinkling” and “tilting”). An analytical relationship is then derived to correlate the back-wall P/E spectrum at one transducer location to the through-transmitted field. Based on the analytical relationship and the statistical description of various beam distortions, a quantitative statistical model is developed to predict the back-wall amplitude fluctuations seen in ultrasonic P/E inspections. The modeling approach is demonstrated on specimens of jet-engine Titanium alloys, and predicted back-wall fluctuation levels at 3 frequencies for both planar and focused transducer are shown to be in good agreements with experiments. In the last section of this paper, the same modeling approach is used to simulate the flaw (small reflector) signal fluctuation. The predicted fluctuation levels are qualitatively agreed with that obtained from the simulated data, which was generated by independent modeling study. This work provides a new perspective to describe the microstructure-induced beam distortion phenomena and suggests many possibilities for future research.

## **DISSERTATION ORGANIZATION**

This dissertation consists of 3 main chapters, preceded by the present general introduction and followed by a general conclusion. Each chapter corresponds to a to-be-submitted journal article. The first chapter is on the variability of the backscattered ultrasonic grain noise in Ti-6Al-4V forging. The grain noise spatial correlation is discussed



in chapter 2. The third chapter 3 is on the microstructure-induced ultrasonic signal fluctuation.

The first chapter is in the form of a paper to be submitted for publication in the *International Journal of Plasticity*. In this paper, we first reviewed the typical microstructure of Ti-6Al-4V forging and various microstructural features that may influence the backscattered grain noise, such as the grain morphology, grain orientation and deformation texture. Special attention was given to how the forging processes may change the microstructural features. The experimental investigations of the ultrasonic properties are then summarized and the correlations between the measured grain noise signals and deformation parameters are demonstrated. After the review of the related theories, we described our modeling approach, including the way we deduced useful microstructural information from forging simulation software, DEFORM<sup>TM</sup>, and how the texture and the presence of two phases may affect the elastic anisotropy variability. The grain noise levels predicted by the model at various locations are compared with experiments. The progresses achieved at different stages of this part of the work have been reported in a number of technical articles [1, 2, 19].

The theoretical investigation of the spatial correlation of the backscattered ultrasonic grain noise and the experimental validation of the theory are presented in chapter 2. It will be submitted for publication in *Journal of Acoustical Society of America*. In this chapter, we first introduced the definition and the significance of grain noise spatial correlation. Following the theoretical frame developed by earlier researchers [3-5, 11, 12], a formal theory is then developed to predict the spatial correlation of the backscattered grain noise in different experimental circumstances. The theory was derived in its general form and also presented in a special form for a Gaussian beam, which can manifest the important controlling physical parameters for the spatial correlation of the backscattered grain noise. The theory is numerically evaluated for several experimental scenarios and a series of

experiments are designed to verify the theory. The predicted results are compared with the measurements, and excellent agreements are observed.

Chapter 3 considers the microstructure-induced ultrasonic signal fluctuations. It will be submitted to the *Journal of Nondestructive Evaluation*. Some progresses of this part of work have been previously published in conference proceedings [46, 47]. In this study, we first explicitly demonstrate various beam distortions induced by the microstructure. An analytical relationship is then derived to correlate the back-wall P/E spectrum at one transducer location to the through-transmitted field. By introducing the appropriate random variables to describe the distorted sound field, we developed a quantitative Monte-Carlo model to predict the back-wall amplitude fluctuations seen in ultrasonic P/E inspections. The modeling approach is demonstrated for both planar and focused probe. In the last section of this paper, the same modeling approach is used to simulate the flaw signal fluctuation. The predicted fluctuation levels are compared with that obtained from the simulated data, which was generated by an independent modeling study. Qualitative agreements are observed.

## REFERENCES

1. Linxiao Yu, Frank J. Margetan, R.B. Thompson and Andrei Degtyar, "Survey of ultrasonic properties of aircraft Engine Titanium forgings", in *Review of Progress in QNDE*, Vol.21B, eds. D.O. Thompson and D.E. Chimenti (Plenum, New York, 1998), p.1510.
2. F. J. Margetan, E. Nieters, L. Brasche, L. Yu, A. Degtyar, H. Wasan, M. Keller and A. Kinney, "Fundamental studies of titanium forging materials - Engine Titanium Consortium II", FAA Technical Center, Atlantic City, N. J., (2004, in review).
3. J. H. Rose, "Ultrasonic backscattering from polycrystalline aggregates using time-domain linear theory", in *Review of Progress in Quantitative NDE*, Vol. 10B, eds. D.O. Thompson and D.E. Chimenti (Plenum, New York, 1991) p. 1715-1720.

4. J. H. Rose, "Ultrasonic backscatter from microstructure", in *Review of Progress in Quantitative NDE*, Vol. 11B, eds. D.O. Thompson and D.E. Chimenti (Plenum, New York, 1992) p. 1677-1684.
5. J. H. Rose, "Theory of ultrasonic backscatter from multiphase polycrystalline solid", in *Review of Progress in Quantitative NDE*, Vol. 12B, eds. D.O. Thompson and D.E. Chimenti (Plenum, New York, 1993) p. 1719-1726.
6. F. J. Margetan, T. A. Gray, and R. B. Thompson, "A techniques for quantitatively measuring microstructure induced ultrasonic noise" in *Review of Progress in Quantitative NDE*, Vol. 10B, eds. D.O. Thompson and D.E. Chimenti (Plenum, New York, 1991) p. 1721-1728.
7. Margetan, F. J., Thompson, R. B., and Yalda-Mooshabad, I., "Backscattered microstructural noise in ultrasonic tone-burst measurements", in *Journal of Nondestructive Evaluation*, Vol. 13, pp. 111-136, 1994.
8. F. J. Margetan, R. B. Thompson and I. Yalda-Mooshabad, "Modeling ultrasonic microstructural noise in titanium alloy" in *Review of Progress in Quantitative NDE*, Vol. 12B, eds. D.O. Thompson and D.E. Chimenti (Plenum, New York, 1991) p. 1735-1742.
9. F. J. Margetan and R. B. Thompson, "Microstructural noise in titanium alloys and its influence on the detectability of hard-alpha inclusion" in *Review of Progress in Quantitative NDE*, Vol. 11B, eds. D.O. Thompson and D.E. Chimenti (Plenum, New York, 1992) p. 1717-1724.
10. F. J. Margetan, Kim Y. Han, I. Yalda, Scot Goettsch and R.B Thompson, "The practical application of grain noise models in titanium billet and forgings", in *Review of Progress in QNDE*, Vol. 14B, eds. D.O. Thompson and D.E. Chimenti (Plenum, New York, 1995) p. 2129.
11. Han, Y. K. and Thompson, R. B., "Ultrasonic backscattering in duplex microstructures: theory and application to titanium alloys", in *Metallurgical Transactions*, Vol. 28A, pp. 91-104 (1997).
12. Han, Y. K., "Relationship between the ultrasonic grain noise and microstructure in two-phase microstructure", Ph.D. Thesis, Iowa State University, Ames, IA, 1994.

13. Thompson, R. B., Margetan, F. J., Rose, J. H., and Han, K. Y., "Influence of microstructure on ultrasonic backscattering noise in titanium alloys," in *Nondestructive Testing and Evaluation*, Vol. 8-9, pp. 485-496, 1992.
14. Yalda-Mooshabad, I. and R. B. Thompson, "Influence of texture and grain morphology on the two-point correlation of elastic constants: theory and implication on ultrasonic attenuation and backscattering", in *Review of Progress in QNDE*, Vol. 14B, eds. D.O. Thompson and D.E. Chimenti (Plenum, New York, 1996) p.1939.
15. Yalda-Mooshabad, I., Thompson, R. B., and Margetan, F., "Predicting ultrasonic grain noise in polycrystals: a Monte Carlo model," in *J. Acoust. Soc. Am.*, Vol. 99, pp. 3445-3455, 1996.
16. F. J. Margetan, P. Haldipur, Linxiao Yu, R. B. Thompson, A. Degtyar, and H. Wasan, "Backscattered ultrasonic noise measurements in jet-engine nickel alloys", in *Review of Progress in QNDE*, Vol. 20B, eds. D.O. Thompson and D.E. Chimenti (AIP, 2001), p. 1314-1321.
17. Paul Panetta, "Backscattering and attenuation during the propagation of ultrasonic waves in duplex titanium alloys", Ph.D. thesis, Iowa State University, Ames, IA, 1999.
18. Yanming Gau, "Effects of material microstructure and surface geometry on ultrasonic scattering and flaw detection", Ph.D. thesis, Iowa State University, Ames, IA, 2003.
19. Linxiao Yu, R.B. Thompson, Frank J. Margetan and Andrei Degtyar, "Modeling ultrasonic grain noise within ti-6al-4v forgings", in *Review of Progress in QNDE*, Vol.22B, eds. D.O. Thompson and D.E. Chimenti (AIP, 2003), p.1339-1346.
20. Anxiang Li, Ron Roberts, Pranaam Haldipur, Frank J. Margetan, and R. B. Thompson, "Computational study of grain scattering effects in ultrasonic measurements", in *Review of Progress in QNDE*, Vol. 22B, eds. D.O. Thompson and D.E. Chimenti (AIP, 2003), p.117-124.
21. G. Ghoshal and J.A. Turner, "Numerical model of ultrasonic backscatter response in polycrystals", to appear in *Review of Progress in QNDE*, Vol. 24, eds. D.O. Thompson and D.E. Chimenti (AIP, 2005).

22. P. Haldipur, F. J. Margetan, R. B. Thompson, "Looking for multiple scattering effects in backscattered ultrasonic grain noise from jet-engine nickel alloys", to appear in *Review of Progress in QNDE*, Vol. 24, eds. D.O. Thompson and D.E. Chimenti (AIP, 2005).
23. J. C. Williams and E. A. Starke, Jr., Deformation, processing, and structure, ed. G. Krauss (Metals Park, OH: ASM, 1984), p.279-354.
24. Frank Larson and Anthone Zarkades, Properties of textured titanium alloys, Metal and Ceramics Information Center, Columbus, Ohio, Metals and Ceramics Information Center, 1974.
25. A. W. Bowen, "Controlled textured titanium alloys", in *Titanium '80, Science and Technology: Proceedings of the Fourth International Conference on Titanium*, edited by H. Kimura, O. Izumi. International Conference on Titanium (4th: 1980: Kyoto, Japan). Warrendale, Pa.: Metallurgical Society of AIME, c1980, pp. 947-954.
26. E.W. Collings, The physical metallurgy of titanium alloys, Metals Park, OH : American Society for Metals, c1984.
27. Babareko, A.A. and Egiz, I.V., "Texture formation in titanium alloy in the process of martensitic transformations during rolling", in *Phys. Met. Metall.*, Vol 69, No. 2, 1990, pp. 130-135.
28. Semiatin, S.L., Seetharaman, V., Weiss, I., "The thermo-mechanical processing of alpha/beta titanium alloys". in *J. Mat.* 33, 1997.
29. Scott E. Schoenfeld and Bimal Kad, "Texture effects on shear response in Ti-6Al-4V plates", in *International Journal of Plasticity*, Vol.18, Issue 4, April 2002, Pages 461-486.
30. F. J. Margetan, M. Gigliotti, L. Brasche and W. Leach, "Fundamental studies: inspection properties for engine titanium alloys", FAA Technical Center, Atlantic City, N. J., Report DOT/FAA/AR-02/114, December 2002.
31. Pranaam Haldipur, F. J. Margetan, Linxiao Yu, and R. B. Thompson, "A study of ultrasonic property variations within jet-engine nickel alloy billets", in *Review of Progress in QNDE*, Vol.21B, eds. D.O. Thompson and D.E. Chimenti, (AIP, Melville NY, 2002) pp. 1502-1509.

32. Linxiao Yu, F. J. Margetan and R. B. Thompson, Unpublished experimental results of the grain noise correlation in titanium alloy forging materials, performed at the Center for NDE at Iowa State University, Ames, Iowa, 2002.
33. D. K. Hsu, D. O. Thompson and R. B. Thompson, "Evaluation of porosity in aluminum alloy casting by single-sided access ultrasonic backscatter", in *Review of Progress in QNDE*, eds. D.O. Thompson and D.E. Chimenti, Vol.5B (1986), p. 1633.
34. Aleksandar Dogandzi and Nawanat Eua-Anant, "Defect detection in correlated noise", in *Review of Progress in QNDE*, Vol. 23A, eds. D.O. Thompson and D.E. Chimenti (AIP, 2004). P.628-635.
35. Walker F. William, "Significance of correlation in ultrasonic signal processing", in *Proc. SPIE Vol. 4325, Medical Imaging 2001: Ultrasonic Imaging and Signal Processing*, eds. Michael F. Insana; K. Kirk Shung. P159-171.
36. F.J. Margetan, I. Yalda, R.B. Thompson, "Predicting gated peak-to-peak grain noise distributions for ultrasonic inspection of metal", in *Review of Progress in QNDE*, eds. D.O. Thompson, D.E. Chimenti (Eds.), Vol. 15B, Plenum Press, New York, 1996, p. 1509.
37. R.B. Thompson, Frank J. Margetan, "Use of elastodynamic theories in the stochastic description of the effect of microstructure on ultrasonic flaw and noise signals", in *Wave motion* 36 (2002) p.347-365.
38. Alan P. Berens, Metal Handbook, Vol. 17, 9th Edition: Nondestructive Evaluation and Quality Control. ASM International, Materials Park, Ohio 44073. p. 689-701.
39. Panetta, P. D., Margetan, F. J., Yalda, I., and Thompson, R. B., "Ultrasonic attenuation measurements in jet-engine titanium alloys", in *Review of Progress in QNDE*, edited by D. O. Thompson and D. E. Chimenti, Vol. 15B, Plenum Press, New York, NY, 1996, pp. 1525-1532.
40. P. D. Panetta, F. J. Margetan, I. Yalda and R. B. Thompson, "Observation and interpretation of microstructurally induced fluctuations of back-surface signals and ultrasonic attenuation in

- titanium alloys”, in *Review of Progress in QNDE*, Vol. 16B, D.O. Thompson and D.E. Chimenti, eds., (Plenum Press, N.Y., 1997), p. 1547-1554.
41. F. J. Margetan, H. Wasan, and R. B. Thompson, “An experimental study of microstructure-induced ultrasonic signal fluctuations in jet-engine titanium alloys”, in *Review of Progress in QNDE*, Vol.19B, eds. D.O. Thompson and D.E. Chimenti, (AIP, Melville NY, 2000) pp.1433-1440.
  42. F.J. Margetan, P.D. Panetta, and R.B. Thompson, "Ultrasonic signal attenuation in engine titanium alloys", in *Review of Progress in QNDE*, Vol.17B, eds. D.O. Thompson and D.E. Chimenti, (Plenum, New York, 1998) p. 1469-1476.
  43. S. Ahmed, R. Roberts and F. J. Margetan, “ Ultrasonic beam fluctuation and flaw signal variance in inhomogeneous media”, in *Review of Progress in QNDE*, Vol. 19B, eds. D.O. Thompson and D.E. Chimenti, (AIP, 2000) p. 985-991.
  44. Anxiang Li, Ron Roberts, Frank J. Margetan, and R. B. Thompson, “Study of the effect of microstructure on ultrasonic signal attenuation” , in *Review of Progress in QNDE*, Vol. 20, eds. D.O. Thompson and D.E. Chimenti, (AIP 2001) p. 1322-1329.
  45. Anxiang Li, Ron Roberts, Frank J. Margetan, and R. B. Thompson, “Influence of forward scattering on ultrasonic attenuation measurement”, in *Review of Progress in QNDE*, Vol. 21, eds. D.O. Thompson and D.E. Chimenti, (AIP 2002) p. 51-58.
  46. Anxiang Li, Linxiao Yu, Ron Roberts, F. J. Margetan, and R. B. Thompson, “A 2-D numerical simulation study of microstructure-induced ultrasonic beam distortions”, in *Review of Progress in QNDE*, Vol. 23, eds. D.O. Thompson and D.E. Chimenti, (AIP 2004) p. 1178-1186.
  47. Linxiao Yu, R. B. Thompson, F. J. Margetan and Yurong Wang, “A Monte-Carlo model for microstructure-induced ultrasonic signal fluctuations in titanium alloy inspections”, in *Review of Progress in Quantitative NDE*, Vol. 23, edited by D. O. Thompson and D. E. Chimenti. (AIP, 2004), p. 1170-1177.

## CHAPTER 1. A MODEL CORRELATING BACKSCATTERED ULTRASONIC GRAIN NOISE TO THE INHOMOGENEOUS PLASTIC DEFORMATION IN Ti-6Al-4V FORGING

A paper to be submitted to the International Journal of Plasticity

Linxiao Yu, R. B. Thompson, and F. J. Margetan

Center for Nondestructive Evaluation, Iowa State University

Ames, IA 50011

Andrei Degtyar

United Technologies Pratt & Whitney,

East Hartford, CT 06108, USA

**ABSTRACT.** In ultrasonic inspections of metals, echoes from internal defects can be masked by so-called “grain noise”, which arises from the scattering of sound waves by the metal microstructure. In pulse/echo inspections, backscattered ultrasonic grain noise is an important factor in determining the probability of detection (POD) for defects of a given type and size. Large variations of backscattered ultrasonic grain noise with position and inspection direction have been observed within Ti-6Al-4V forgings used for rotating jet-engine components. Such noise variations are believed to be correlated with the microstructural variations that arise from the inhomogeneous plastic deformation that occurs when a billet blank is forged. To quantify defect detection sensitivity throughout a forging, one needs to know how the grain noise varies with position. A modeling approach is developed to predict the backscattered grain noise from microstructure variations which themselves are deduced from a plastic deformation model of the forging process. One begins with circular/elliptical elements in the billet, whose elongations and orientations are specified. These elements are followed through the forging process which changes their shapes and orientations and introduces deformation texture. The local microstructure morphology and texture at a location in the forging are deduced by using DEFORM<sup>TM</sup>. There are three principal model inputs: the average volume of each scattering element; and two



parameters that quantify the elastic property variation between nearby scatters. The predicted grain noise levels by the model at various locations are compared with experiments. Reasonably good agreements are found.

## 1. INTRODUCTION

Commercial Ti-6Al-4V alloy is widely used in the rotating components of aircraft engines. The failure of such parts can be quite catastrophic because of the large amount of kinetic energy. To ensure the safety and longer lifetime of these critical parts working in the hostile environments of high temperature and high stress, the need to detect smaller defects becomes more and more important. Ultrasonic inspection is one of the non-destructive evaluation (NDE) methods widely used by the aircraft engine manufacturers because of its capability to penetrate to the interior of a component. But the detection of smaller defects is made difficult by such issues as the presence of a high level of noise signals backscattered from the two-phased ( $\alpha + \beta$ ) microstructure. Sometimes, the backscattered noise level is comparable or even higher than the small defect response. The inspection sensitivity, a quantity that describes the smallest defect a system can detect, and the probability of flaw detection (POD), a property that plays a central role in the statistical management of part lifetimes, are directly related to the backscattered grain noise [1, 2].

Fundamentally, the backscattered ultrasonic grain noise in polycrystalline material is the result of inhomogeneous acoustic properties in the material. The inhomogeneities are primarily associated with the anisotropy of the elastic constants in grains or crystallites. The total backscattering will be controlled by grain morphology, grain orientation and elastic anisotropy of the microstructure. In current theories based on the single scattering approximation [20-23], the later is described by a quantity  $\langle \delta C_{ij} \delta C_{kl} \rangle$ , an ensemble average of the deviation of elastic constants from their isotropic values, which can be influenced by

the presence of texture. Detailed discussions about these quantities will be given in the later section of this paper.

Large variations of backscattered ultrasonic grain noise with position and inspection direction have been observed within Ti-6Al-4V forgings intended for use in rotating jet-engine components [3, 4]. Such noise variations are believed to be correlated with the local microstructural variations that arise from thermo-mechanical processing (TMP). Historically, TMP has been used as the primary means of changing the shapes and sizes of materials, transforming, for example, cast ingot into a desired wrought product. However, varying the details of the TMP has also become an increasingly common way of controlling the microstructure and hence mechanical properties, e.g. by imposing restrictions on the working temperature range and the amount of work [5]. A variety of microstructural characteristics of the final product (grain size, degree of recrystallization, grain aspect ratio, texture, etc.) are sensitive to the TMP details. For example, if there is negligible recrystallization during TMP, the grain aspect ratio is primarily determined by the initial grain structure and the directional metal flow.

The typical manufacturing TMP of a rotating component is shown in Figure 1. A cast ingot is first worked into a cylindrical billet having a reduced diameter and then forged to a shape near that of the forging product. The billet microstructure will depend on the microstructure of the casting and the TMP history. In the casting, the grains are typically equiaxial. Because of the sharp reduction in diameter, the billet typically has a microstructure with elongated macrograins (prior  $\beta$  grains), consisting primarily of  $\alpha$  colonies of hexagonal crystallites created by solid-state transformations with orientations determined in part by that of the prior  $\beta$  grain [6]. The final microstructure in the forging is dependent on the specific forging processing, such as the working temperature, amount of work, deforming rate, cooling rate and subsequent heat treatment. Except for the working temperature range ( $\alpha + \beta$  forging), we do not have access to the other TMP parameters for

the samples that we studied, which are hold as proprietary by the engine manufacturers. But we expect that the microstructure in the finial forging is much more complicated than that in the billet because the strain magnitude and metal flow direction vary substantially at different locations within the forging.

Besides the microstructure morphology, the large inhomogeneous plastic deformation during forging introduces a preferred orientation of crystallites or texture by crystallite slipping, twinning or their combination. Such deformation-dependent texture will cause the elastic anisotropy variability factor,  $\langle \delta C_{ij} \delta C_{kl} \rangle$ , to vary with position and direction inside the forging. This variation influences the backscattered grain noise. Detailed description will be presented later. The deformation texture in Ti-6Al-4V alloy has been the subject of a number of studies [5, 7-12]. These textures are most conveniently represented by pole figures which describe the statistical distribution of grain orientations using a stereographic plot to depict the angular distribution of the poles of a particular crystallographic plane. For Ti-6Al-4V, the texture is usually represented by the pole figure of the hexagonal basal plane, (0001). The extent or intensity of texture is dependent on the amount of work. The type of texture depends on working method and working temperature. Figure 2, provided by reference [5], summaries the possible deformation textures in Ti-6Al-4V under the different combination of types of working and working temperature ranges. The resulted textures are represented by the basal plane pole figures (the circular plots). The cross-hatchings in the central sketches indicate the temperature range of working as a function of time. Pole figures in the upper row are results under the unidirectional working during rolling and pole figures in the bottom row are results under axisymmetrical forging. When axisymmetrical load is applied just below the  $\beta$  transus temperature and slow cooling while working, as the forging processing for the rotating components of interest in this paper, the resulted textures become rotationally symmetric about the axis of principle strain associated with forging loading (or normals of the metal flow lines), i.e., the texture is spread into a circularly symmetric

distribution of basal poles around the circumference of the (0001) pole figure. Specifically, under the TMP conditions highlighted in Figure 2, the hexagonal crystallites in the final product tend to have their basal plane normals parallel with metal flow directions.

Because of the influence of the inhomogeneous plastic deformation, the overall microstructure within the forging is expected to have localized variations in grain morphology, grain orientation and texture. However, since such forgings are often large, it is difficult to get a detailed picture of how the microstructure varies throughout the forging by the traditional metallographic approach. This paper describes an approach whereby useful microstructural information can be deduced from forging simulation software, such as DEFORM<sup>TM</sup>, a commercial software package produced by Scientific Forming Technologies Corporation, Columbus, Ohio.

Examples of DEFORM<sup>TM</sup> outputs are shown in Figure 3, for the case of a jet-engine forging produced from a cylindrical billet. Figure 3a is the “strain map”, which illustrates how the magnitude of the forging strain varies with position. The geometry shown in Figure 3a is the half cross-section of the forging to be simulated. The left end is close to the forging central line. Figure 3b displays a “net map”, which indicates how 7:1 ellipsoid-like elements (be enlarged to show the details) in the billet would be modified by the forging process. Again, the geometry shown in the right part of Figure 3b is the half cross-section of the forging to be simulated. The forging diameter is about 6” and the maximum thickness is about 3.5”. Here the 7:1 aspect ratio in the billet has been motivated by the general shape of billet macrograins [3, 4]. If one had started with circles in the billet, the resulting local element aspect ratio in the forging could instinctively be regarded as a measure of local strain. We define this quantity as effective strain  $\varepsilon_e$ , which plays an important role in our modeling in the later section of this paper. By starting with ellipsoids, we take into account the deformation that occurred in passing from the ingot to the billet. Note in Figure 3b that the forging process changes both the elongations and orientations of the elements. The

rectangular and circular boxes in the figure indicate the locations where coupons (numbered from #1 to #8) were cut for the ultrasonic property measurements. The notations used to describe the coupon locations and inspection surfaces are also marked, including “ID” (internal diameter), “OD” (outer diameter), “TOP” (top), “BOTTOM” (bottom), “WEB” (web).

In the current work, a modeling approach is developed to predict the backscattered grain noise from microstructure variations which are in turn deduced from a plastic deformation model of the forging process. One begins with hypothesized scattering elements in the billet, whose elongations and orientations are specified. These elements are followed through the forging process that changes their shapes and orientations and introduces deformation texture. The local scattering element geometry and texture at a specific position in the forging are deduced by using DEFORM<sup>TM</sup>. There are three principal model inputs whose quantitative values are determined by fitting the model predictions with a subset of the experimental data: the global average volume of each scattering element which is assumed to be fixed all over the forging and two parameters that quantify the elastic property variation between nearby scattering elements. These parameters are inherently controlled by the crystallite anisotropy of the microstructure and the local texture.

In section II, some experimental results are reviewed, which motivate the modeling work in this paper. In Section III, we will briefly review the related theory and identify the quantities which determine the backscattered grain noise level. The condition that must be satisfied to ensure the validity of the theory for this textured microstructure is also stated. In section IV, we will discuss how the texture and the presence of two phases may affect the elastic anisotropy variability. A few concepts in quantitative texture analysis are reviewed, with emphasis given to the way by which we model these effects. The experimental and predicted results are compared in section V. Summary and conclusions are presented in section VI.

## 2. EXPERIMENTAL MOTIVATIONS

Ultrasonic properties (velocity, attenuation and backscattered grain noise) were measured in all the 7 rectangular coupons shown in Figure 3b. The detailed measurements and result analysis were summarized in reference [3, 4]. For completeness, we present the related experiment and results in this paper. The experimental setup for the noise measurement is shown in Figure 4a. The ultrasonic beam is focused in the top half of the coupon thickness. The backscattered noise signal from a uniform microstructure varies with the depth because of the changing cross-section of the focused beam, as indicated by the curve and accompanying scale in Figure 4a. The four large surfaces of each coupon were scanned and often yielded substantially different noise levels. One example of the noise anisotropy and inhomogeneity is illustrated in Figure 4b. The two C-scan images show the gated-peak-to-peak backscattered grain noise seen through different faces of the same coupon at the same gain setting (35dB). For reference purpose, Figure 4c shows the C-scan image of a #1 FBH located 0.5 inches deep in an IN100 block, acquired at the same water path.

For the case considered in Figure 4b, the noise C-scan for the “OD” direction is obviously non-uniform. To better handle such cases when quantifying noise levels, we split each image into left and right halves and record the noise statistics separately for each half. This leads to 8 combinations of inspection direction and quadrant for each coupon (numbered as shown in Figure 4d). Peak and average noise values were deduced for each combination and are plotted in Figure 5. The noise levels are referenced to a (hypothetical) #1 FBH in Ti 6Al-4V material located at the focal plane (0.31” deep) which lies within the gate used for

the noise measurements. The amplitude of such a FBH reference signal was estimated from the measured reference (#1 FBH, 0.5" deep in IN100) by making model-based adjustments for material property and depth differences. We note in Figure 5 that the noise level clearly varies with coupon position and inspection direction.

Even with the large variability shown in Figure 5, close correlations between the measured ultrasonic properties and deformation parameters are observed [3, 4]. Figure 6 summarizes results for one case, namely the correlation between noise anisotropy and net element projection ratio. Figure 3b illustrates that the DEFORM<sup>TM</sup> simulation can show how 7:1 ellipsoidal elements in the billet would be modified by the forging process. As shown in Figure 6a, we define  $Y/X$  as the projection ratio of an ellipsoidal element onto the two inspection directions. The noise anisotropy (NA) is defined as the ratio of the average noise levels seen in a local region from the two inspection directions. We know that the backscattered noise level from a local region is expected to depend in part on the cross-sectional view that the grain/scatterer presents to the sonic beam [23]. Thus, if we can assume the element projection from the DEFORM<sup>TM</sup> simulation is proportional to the grain/scatterer projection ratio, we would find strong correlation between  $Y/X$  and NA. The results are shown in Figure 6b for all the 7 rectangular coupons. There are four plotted points for each coupon, corresponding to the quadrants showing in Figure 4d. A clear trend is well demonstrated. This experimental observation indicates that the net map produced by the DEFORM<sup>TM</sup> contains useful information of the resulting microstructure produced by the forging processing. The microstructural information is essential in FOM/grain noise predictions. This paper is a natural extension of the earlier work [3] and the objective is to get a quantitative understanding of the variability of the absolute grain noise levels within the forging, as influenced by the inhomogeneous plastic deformation associated with the forging processing.

### 3. REVIEW OF THE THEORY

Because of its great importance in nondestructive evaluation and materials characterization, ultrasonic backscattering has been investigated by many authors [13-23]. A series of papers by Rose [20-22] relate backscattered noise levels to the physical properties of the microstructure. Using a single-scattering assumption and the “Born” approximation, Rose developed a rigorous stochastic theory for the backscattered noise power, which led to explicit expressions for backscattering in randomly orientated, equiaxed, single-phase [21] and multi-phase [22] polycrystals. Han and Thompson’s work [23] extended Rose’s theory to the case of duplex microstructures, which may contain texture and elongated microstructural features with correlations in grain orientation. The expressions used in our work are consistent with those in Reference [23].

A commonly used measure of a microstructure’s noise generating capability is the backscattering power coefficient  $\eta(\omega)$ , i.e., the differential scattering cross section per unit volume in the backward direction [25, 26]. Some authors prefer to use the square root of  $\eta(\omega)$ , the so-called grain noise figure-of-merit ( $FOM(\omega)$ ) [15-19], since it is directly proportional to the noise voltage observed on an oscilloscope during ultrasonic inspection. Generally speaking,  $FOM$  is a measure of the noise generation capability of material. In the theories of Rose, Han and Thompson, under the assumption that the solid density is independent of position,  $FOM(\omega)$  and  $\eta(\omega)$  for longitudinal waves propagating in the  $S_3$ -direction are related to microstructure features by:

$$FOM(\omega)^2 = \eta(\omega) = \frac{k^4}{(4\pi\rho V_l^2)^2} \int d^3\vec{S} \left\langle \delta C_{33}(\vec{r}) \delta C_{33}(\vec{r}') \right\rangle e^{2ikS_3} \quad (1)$$

where  $\omega$  is the angular frequency,  $k$  is the magnitude of the wave vector of the incident wave,  $\rho$  is the density of the solid,  $V_l$  is the longitudinal wave velocity,  $\vec{S} = \vec{r} - \vec{r}'$  is a vector defined by the two points  $\vec{r}$  and  $\vec{r}'$  in the solid medium,  $S_3$  is the component of  $\vec{S}$  in the



direction of wave propagation (3-direction),  $\delta C_{33}(\vec{r})$  is the local deviation of the elastic constant from its Voigt average  $\delta C_{33}(\vec{r}) = (C_{33} - C_{33}^{Voigt})$ , and the notation  $\langle \dots \rangle$  denotes an ensemble average.  $\langle \delta C_{33}(\vec{r}) \delta C_{33}(\vec{r}') \rangle$  is known as the two-point correlation of elastic constants, which describes the correlation in the perturbation in the elastic stiffnesses. Detailed discussions about this term can be found in a number of earlier works [20-23]. For single phase samples which have a macroscopically homogeneous and a randomly oriented microstructure,  $\langle \delta C_{33}(\vec{r}) \delta C_{33}(\vec{r}') \rangle$  can be written in the form of:

$$\langle \delta C_{33}(\vec{r}) \delta C_{33}(\vec{r}') \rangle = \langle \delta C_{33} \delta C_{33} \rangle W(\vec{r} - \vec{r}') \quad (2)$$

where  $\langle \delta C_{33} \delta C_{33} \rangle$  is a constant controlled by the crystallite elastic anisotropy, and  $W(\vec{r} - \vec{r}')$  is the probability that two points separated by the distance of  $\vec{r} - \vec{r}'$  in the solid are in the same crystallite. More specifically,  $\langle \delta C_{33} \delta C_{33} \rangle$  is the average over solid angle of  $(C_{33} - C_{33}^{Voigt})$  for a single crystal [23]. Thus equation (1) can be rewritten in this case as:

$$FOM(\omega)^2 = \eta(\omega) = \left( \frac{\omega^2}{4\pi\rho V_l^2} \right)^2 \langle \delta C_{33} \delta C_{33} \rangle \int d^3\vec{S} W(\vec{S}) e^{2ikS_3} \quad (3)$$

According to Reference [23, 24], for the elongated ellipsoidal scattering element depicted in Figure 7, which is assumed to be axially symmetric about the z-axis with semi-axes  $a_m$  and  $c_m$ , respectively, equation (2) can be specifically written as in equation (4-7). The  $W(\vec{r} - \vec{r}')$  term has been assumed to be an exponentially decreasing function of  $\vec{r} - \vec{r}'$ , with the rates of decrease in different directions tied to the parameters  $a_m$  and  $c_m$  through Equation (6).

$$FOM(\omega)^2 = \eta(\omega) = \left( \frac{k^2}{4\pi\rho V_l^2} \right)^2 \langle \delta C_{33} \delta C_{33} \rangle \int_0^{2\pi} \int_0^\pi \frac{2 \sin \theta}{A^3} d\theta d\phi \quad (4)$$

$$A = \frac{\{1 + (R^2 - 1) \cos \theta^2\}^{1/2}}{(3VR/4\pi)^{1/3}} - 2ik (\sin \theta \sin \phi \sin \tau + \cos \theta \cos \tau) \quad (5)$$

$$R = \frac{a_m}{c_m} : \text{Aspect ratio of the scattering element} \quad (6)$$

$$V = \frac{4\pi a_m^3}{3R} : \text{Average volume of the scattering element} \quad (7)$$

Equations (1) through (7) indicate, for a randomly orientated medium with possible grain elongation in an axis-symmetric form, that the backscattered noise level is determined by the scatterer's geometric features and elastic property variations. The geometric features include the scattering element aspect ratio ( $R$ ), its orientation with respect to the incident beam ( $\tau$ ), and the average volume ( $V$ ). It is our hypothesis that local values for  $R$  and  $\tau$  can be directly deduced from DEFORM<sup>TM</sup> if the aspect ratio and orientation of the scattering elements in the billet are specified. Global values of average volume ( $V$ ) will be deduced by fitting with the experimental data.

The elastic property variations of the medium enter through the  $\langle \delta C_{33}(\vec{r}) \delta C_{33}(\vec{r}') \rangle$  term. For a randomly orientated medium,  $\langle \delta C_{33} \delta C_{33} \rangle$  is a constant controlled by the crystallite elastic anisotropy and can be move out of the volume integral as in equation (3) and its sequels. However, for a medium having preferred crystallite orientation,  $\langle \delta C_{33}(\vec{r}) \delta C_{33}(\vec{r}') \rangle$  is much more complicated. In particular, it will depend on position if the texture is not uniform. It can be sees from Figure 3a, because of the continuous nature of the forging processing, the deformation strain magnitude varies gradually from point-to-point within the forging. However, it changes quite a lot from ID (center) side to OD (edge) side due to the

large dimension of the forging (radius is about 6 inches). If the variation gradient and the texture intensity are small enough, it might be sensible to assume that Equation (3) is still valid within a local volume of the solid, but that  $\langle \delta C_{33} \delta C_{33} \rangle$  varies with the texture which is determined by the deformation strain within the forging. The texture effect on  $\langle \delta C_{33} \delta C_{33} \rangle$  will be presented in the next section.

Note that equation (4) contains a complicated two-dimensional integral, which can only be evaluated numerically. Since the calculated result of this two-dimensional integral are the intermediate input of a numerical optimization procedure, high computation efficiency is desired. To achieve this goal, an adaptive algorithm using a recursive technique was developed to perform the numerical integration. The algorithm is capable of detecting and locating the region where the integrand was most appreciable, and then clustering the integration grid points only in that region.

#### 4. TWO-POINT CORRELATION OF ELASTIC CONSTANTS IN TEXTURED TWO-PHASE MICROSTRUCTURE

When texture intensity and its variation are small, the texture effect on the two-point correlation function of elastic constants is through the  $\langle \delta C_{33} \delta C_{33} \rangle$  term. Because of the presence of texture,  $\langle \delta C_{33} \delta C_{33} \rangle$  may change with inspection direction. To quantify the texture effects on  $\langle \delta C_{33} \delta C_{33} \rangle$ , we adopt the quantitative approach of texture analysis developed by Roe [27, 28]. The intensity and type of texture is most conveniently discussed in terms of the crystallite orientation distribution function, or so called ODF, which gives the probability of a given crystallite in the sample having a specified orientation with respect to the sample axes. Specifically, the orientation of a crystallite in a microstructure is represented by a set of Euler angles  $\theta, \psi, \phi$ . The ODF is represented by  $w(\xi, \psi, \phi)$  (where  $\xi = \cos \theta$ ), and  $w(\cos \theta, \psi, \phi) \sin \theta d\theta d\psi d\phi$  is the probability of finding a crystallite orientated in the angular range of  $d\theta d\psi d\phi$ . Obviously,

$$\int_0^{2\pi} \int_0^{2\pi} \int_{-1}^1 w(\xi, \psi, \phi) d\xi d\psi d\phi = 1 \quad (8)$$

Once  $w(\xi, \psi, \phi)$  is specified, the effect of texture can be evaluated. In our case,  $\langle \delta C_{33} \delta C_{33} \rangle$  with texture can be evaluated by equation (9):

$$\langle \delta C_{33} \delta C_{33} \rangle = \int_0^{2\pi} \int_0^{2\pi} \int_{-1}^1 [\delta C_{33}(\xi, \psi, \phi) \delta C_{33}(\xi, \psi, \phi)] w(\xi, \psi, \phi) d\xi d\psi d\phi \quad (9)$$

The  $\delta C_{33}(\xi, \psi, \phi)$  in equation (9) is the local deviation of the elastic constant from its Voigt average of the macroscopically homogeneous alpha phase microstructure, i.e.,  $\delta C_{33}(\xi, \psi, \phi) = C_{33}(\xi, \psi, \phi) - C_{33}^{Voigt}$  [30].

As show in Figure 2, because of the axisymmetric load, the typical texture in a  $\alpha + \beta$  forging is represented by the circularly symmetric distribution of basal poles around the circumference of the (0001) pole figure. In other words, the basal plane normals of the crystallites are prone to symmetrically align with the locally varying metal flow directions. Mathematically,  $w(\xi, \psi, \phi)$  is only a function of  $\xi$  or  $\theta$  ( $\xi = \cos \theta$ ). This is illustrated in Figure 8.

We do not know how exactly the orientation distribution of the basal poles changes with  $\theta$ . For mathematical simplicity, we assume  $w(\xi)$  is in the Gaussian form of  $w(\xi) = C e^{-(\xi/\Delta)^2}$ . By the normalization condition stated in equation (8), the constant C can be specified as in equation (10), where  $erf$  is the error function:

$$w(\xi) = \frac{1}{[4\pi^{5/2} \Delta \operatorname{erf}(\frac{1}{\Delta})]} e^{-(\xi/\Delta)^2} \quad (10)$$

Figure 9 shows how the shape of the one-variant ODF  $w(\xi)$  changes with  $\xi$  at different  $\Delta$ . Clearly,  $\Delta$  is a quantity determining the texture intensity. When a  $\Delta$  becomes very large, the texture vanishes, consistent with the fact that  $w(\xi)$  is a constant for a randomly orientated medium. The smaller  $\Delta$  corresponds to the heavier texture. We know the fact that the texture intensity is determined by the amount of work, or the deformation strain. Thus we can correlate local strain to the texture intensity through  $\Delta$ . Assume  $\Delta$  relates to the effective strain  $\varepsilon_e$  as:

$$\Delta = \frac{P_1}{\sqrt{\varepsilon_e}} \quad (11)$$

where  $P_1$  is a fitting parameter which can be deduced by fitting the theory predictions with a subset of our measurements. Then the ODF  $w(\xi)$  finally relates to  $\varepsilon_e$  as:

$$w(\xi) = \frac{\sqrt{\varepsilon_e}}{[4\pi^{5/2} P_1 \operatorname{erf}(\frac{\sqrt{\varepsilon_e}}{P_1})]} e^{-\xi^2 \varepsilon_e / P_1^2} \quad (12)$$

Texture effect on  $\langle \delta C_{33} \delta C_{33} \rangle$  can be evaluated by replacing  $w(\xi)$  in Equation (9) with the expression shown in Equation (12). A specific example is given below to explain how to evaluate the texture effects on  $\langle \delta C_{33} \delta C_{33} \rangle$ . As show in Figure 3b, coupon #2 is cut from the web region, where the heaviest deformation occurs. Both the net-map output of DEFORM<sup>TM</sup> (Figure 3b) and the forging macroetch (Figure 10a) indicate the local metal flow is roughly aligned with the forging radial direction. According to the earlier discussions with

Figure 2, the normals of the crystallites basal planes in this region tend to be aligned with the metal flow. Because of the presence of texture, the  $\langle \delta C_{33} \delta C_{33} \rangle$  term would be different when the incident ultrasonic beam propagates through different directions. We deduce the average local effective strain from the net-map and the exact value of  $\langle \delta C_{33} \delta C_{33} \rangle$  can be evaluated by using Equation (12) and (9) once  $P_1$  is known.

Even though the hexagonal  $\alpha$  phase is the dominate phase in the  $\alpha + \beta$  forging, the presence of  $\beta$  phase has a measurable, though less effect on the elastic variability term. The  $\beta$  phase has cubic crystal structure, which is much less anisotropic than the hexagonal crystal structure. In other words, the  $\langle \delta C_{ij} \delta C_{kl} \rangle$  for the two-phase microstructure is expected to be smaller than the pure  $\alpha$  structure. Mathematically, we introduce another fitting parameter  $P_2$  to account for this effect:

$$\langle \delta C_{ij} \delta C_{kl} \rangle_{\alpha + \beta} = P_2 \langle \delta C_{ij} \delta C_{kl} \rangle_{\alpha} \quad (13)$$

## 5. COMPARISON BETWEEN THEORY AND EXPERIMENT

As stated early, the global model parameter  $V$  is assumed to be constant throughout the forging, while the local variable  $\langle \delta C_{33} \delta C_{33} \rangle_{\alpha + \beta}$  is determined by the two fitting parameters  $P_1$ ,  $P_2$  and the local effective strain  $\varepsilon_e$ . Specifically, we calculate FOM for a particular inspection direction in the forging according to the following procedure, which include a process to find the unknown parameters by fitting the theory predictions to a subset of the measurements (steps 1-3) and then use of the theory to predict noise at other locations and directions (step 4): Step #1, Analyze the net maps and tabulate the quantities to be used in the calculation, including effective strain  $\varepsilon_e$  (run DEFORM<sup>TM</sup> starting with circular elements in billet), element elongation and orientation ( $R$  and  $\tau$ ) at that location (run DEFORM<sup>TM</sup> starting with elliptical elements with specified aspect ratio in billet). Step #2, Using quantities obtained in step #1, for any given values of  $V$ ,  $P_1$  and  $P_2$ , calculate the

FOM at one frequency following equations (9-12) and (4) to (7). Step #3, Repeat step #2 to calculate FOM at a series of frequencies. The results are used by a numerical optimization procedure to find the optimal  $V$ ,  $P_1$  and  $P_2$  to match a subset of the experimental data. Step #4, Using the optimal  $V$ ,  $P_1$  and  $P_2$ , calculate the FOM at other locations having different values of  $R$ ,  $\tau$  and  $\varepsilon_e$ .

$V$ ,  $P_1$  and  $P_2$  were chosen by fitting the model predictions to two sets of measured *FOM-vs.-Frequency* data (coupon #2, side 4 and coupon #8, side 1). The experimental *FOM-vs.-Frequency* data were deduced by comparing the mean spectrum of the backscattered grain noise to that of a back wall echo of a reference [2, 15-17]. Figure 10a shows the relative locations of two coupons (#2 and #8) to be used in the fitting. The background of Figure 10a is the macroetch of part of forging cross-section. The left end is close to the forging central line. *FOM-vs.-Frequency* curves measured through coupon #8 side 1 and #2 sides 4 were used for the fitting. The fitting parameters were found to be  $V = 0.382\text{E-}06 \text{ cm}^3$ ,  $P_1=2.7$  and  $P_2=0.6$ . The measured and fitted curves are compared in Figure 10b and 10c. Note that the large noise difference in these two coupons is well reproduced by the model.

Because of the presence of deformation texture, the bulk elastic stiffnesses of this forging are no longer those of an isotropic sample. The ultrasonic velocity, which is directly determined by material bulk elastic constants, has been measured in all the coupons for waves propagating in both radial and axial directions. The difference in the velocity between the radial and axial directions is shown to be proportionally related to the effective strain  $\varepsilon_e$  [4], i.e, the more deformation, the more velocity anisotropy. The consistency of our model with this observation has been studied by calculating the texture effect on the bulk elastic constants in the forging using Equation (14). We use the same  $P_1$  and  $P_2$  obtained from the optimization and the local effective strain  $\varepsilon_e$  is deduced from the net-map:

$$\langle C_{ij} \rangle = \int_0^{2\pi} \int_0^{2\pi} \int_{-1}^1 C_{ij}(\xi, \psi, \phi) w(\xi, \psi, \phi) d\xi d\psi d\phi \quad (14)$$

The velocity variation, defined as the percentage of absolute difference between the velocity measured in the radial and axial directions, in different coupons can then be evaluated. Figure 11 presents the experimental and predicted results on velocity variation. The label with each experimental data point is the coupon number (see Figure 3b). We can see that coupon #2, cut from the web region where the heaviest deformation occurs has, the largest velocity variation. The general good agreement in Figure 11 further demonstrates, from a different perspective, that our modeling approach on the deformation texture is reasonably accurate.

Once we find the optimal parameters ( $V$ ,  $P_1$  and  $P_2$ ), we can compare model predictions with the other available experimental data. Figure 12 summarizes the comparison of *FOM vs. Frequency* data, including data for the remaining three sides of coupon #8 and the remaining 1 side of coupon #2. Note that coupons #2 and #8 have very different deformations, as can be seen from the macroetch shown in Figure 10a and the net-map output of the DEFORM<sup>TM</sup> simulation shown in Figure 3. However, we can see that all model predictions are generally in good agreements with the experimental data. There is another interesting observation: in coupon #8, the measured noise levels through radial directions (side 1 and side 4) are high and the measured noise levels through axial directions (side 2 and side 5) are much lower. While in coupon #2, the higher noise level can be observed when inspected through axial direction (side 5) and the much lower noise can be seen through radial direction (side 4). This reversal of noise directionality is well predicted by the model. Full FOM-vs-frequency curves for all coupons are not available. However, average Gated-Peak Noise (GPN) amplitudes relative to a flat-bottomed hole reference were measured for C-scans over each quadrant of each coupon using a focused transducer [4]. To a good first approximation, the average GPN amplitude within a quadrant will be proportional to the average FOM value near the center frequency of the transducer [29]. For 7 selected coupons, whose locations are shown in Figure 3, measured FOM and GPN data are both available. As



shown in Figure 13a, these data were used to find an approximate scaling factor relating average GPN to FOM at 10 MHz. Using this scaling factor, GPN amplitudes could then be predicted from the model FOM values for each coupon quadrant. Predicted GPN amplitudes are compared with experiments in Figure 13b. Our simplified model treatment ignores the fact that ultrasonic attenuation varies throughout the forging [3, 4], and effectively ignores the frequency dependence of FOM. Nonetheless, we find a good correlation between measured and predicted GPN amplitudes, which each vary by a factor of 5 within the forging. If the model were exact, the points in Figure 13b would all lie along a diagonal line though the plot region. The largest departures from this ideal situation generally occur for coupons #5 and #6, where the macroetch indicates that the flow lines have a “swirling” appearance. The model predictions are quite sensitive to the scatterer orientation and shape parameters,  $\tau$  and  $R$ . Values for these deduced from DEFORM<sup>TM</sup> simulations may be less accurate in regions where the metal flow lines swirl.

To further test the model, another comparison was made based on the angular dependence of *FOM*. A cylindrical coupon 1.25” in diameter and 2.0” long was cut from the web region of the forging, as indicated in Figure 14a. As seen from the DEFORM<sup>TM</sup> simulation of Figure 3b, the resulted microstructure at that location is expected to be elongated in the radial direction. The predicted backscattered noise amplitude is largest when the scattering elements present the largest cross-sectional area to the incident beam. Thus the predicted FOM, regarded as a function of the orientation angle,  $\tau$ , is expected to have peaks at 90 and 270 degrees w.r.t. the forging’s radial direction. The cylindrical coupon was rotated on a turntable and scanned using a cylindrically focused transducer (central frequency is 5MHz). The resulting C-scan image of GPN amplitudes from the coupon’s interior is shown in Figure 14b. The angular profile of the GPN image, averaged over the linear scan direction, is compared in Figure 14c with the predicted *FOM*-versus- $\tau$  curve at 5MHz. As before, the experimental and model quantities are expected to be approximately

proportional to one another, although the scaling factor will be different from that used earlier because of the effect of the curved entry surface and the fact that transducers are different. Thus in Figure 14c we have simply scaled the predicted *FOM* curve to have similar amplitude to the measured GPN profile. The experimental curve is seen to have somewhat sharper peaks, but the overall level of agreement is reasonably good.

## 6. SUMMARY AND CONCLUSION

A model was developed to correlate backscattered grain noise levels with microstructural variations that arise from the inhomogeneous plastic deformation during forging. The model inputs include the average volume of the scattering elements, which is assumed as a constant throughout the forging, the geometrical features of the scattering element, and the local texture due to the inhomogeneous effective strain. The shapes and orientations of the scattering elements are deduced from DEFORM<sup>TM</sup> simulations for the forging, and vary throughout the entire forging. The three remaining modeling parameters, mean volume of the scattering elements  $V$  and the two parameters ( $P_1$  and  $P_2$ ) to quantify elastic property variability, were obtained by fitting a subset of the experimental FOM data. Model testing was done by comparing predictions with experimental data for: (1): *FOM* -vs-frequency for selected rectangular coupons; (2) velocity variation for all coupons throughout the forging; (3) mean GPN amplitudes within a suite of 7 rectangular coupons from different regions of the forging; and (4) angular dependence of grain noise for one cylindrical coupon cut from the web region of the forging. Reasonable good agreements between experiments and model predictions were achieved.

Through this research, we have gained fundamental understanding of the ultrasonic properties of Ti-6Al-4V forging. The experimental investigations laid out a foundation to guide the development and application of improved inspection system, and the modeling research provides a potential tool to quantify the inspection performance.

## ACKNOWLEDGEMENTS

This material is based upon work supported by the Federal Aviation Administration under Contract #DTFA03-98-D-00008, Delivery Order IA029 and performed at United Technologies Pratt & Whitney and at the Iowa State University Center for NDE as part of the Center for Aviation Systems Reliability program.

## REFERENCES

1. R.B. Thompson, Frank J. Margetan, "Use of elastodynamic theories in the stochastic description of the effect of microstructure on ultrasonic flaw and noise signals", *Wave motion* 36 (2002) 347-365.
2. F. J. Margetan, Kim Y. Han, I. Yalda, Scot Goettsch and R.B Thompson, "The practical application of grain noise models in titanium billet and forgings", *Review of Progress in QNDE*, Vol. 14B, eds. D.O. Thompson and D.E. Chimenti (Plenum, New York, 1995) p. 2129.
3. Linxiao Yu, Frank J. Margetan, R.B. Thompson and Andrei Degtyar, "Survey of ultrasonic properties of aircraft Engine Titanium forgings", *Review of Progress in QNDE*, Vol.21B, eds. D.O. Thompson and D.E. Chimenti (Plenum, New York, 1998), p.1510.
4. F. J. Margetan, E. Nieters, L. Brasche, L. Yu, A. Degtyar, H. Wasan, M. Keller and A. Kinney, Fundamental studies of titanium forging materials - Engine Titanium Consortium II, FAA Technical Center, Atlantic City, N. J., (2004, in review).
5. J. C. Williams and E. A. Starke, Jr., Deformation, Processing, and Structure, ed. G. Krauss (Metals Park, OH: ASM, 1984), p.279-354.
6. Paul Donald Panetta, "Backscattering and attenuation during the propagation of ultrasonic waves in duplex titanium alloys", PhD Dissertation, Department of Materials Science and Engineering, Iowa State University, 1999.

7. Frank Larson and Anthone Zarkades, Properties of Textured Titanium Alloys, Columbus, Ohio: Metals and Ceramics Information Center, 1974.
8. A. W. Bowen, "Controlled textured titanium alloys", Titanium '80, Science and Technology: *Proceedings of the Fourth International Conference on Titanium*, edited by H. Kimura, O. Izumi. International Conference on Titanium (4th: 1980: Kyoto, Japan). Warrendale, Pa.: Metallurgical Society of AIME, c1980, pp. 947-954.
9. E.W. Collings, The Physical Metallurgy of Titanium Alloys, Metals Park, OH: American Society for Metals, 1984.
10. Babareko, A.A. and Egiz, I.V., "Texture formation in titanium alloy in the process of martensitic transformations during rolling", *Phys. Met. Metall.*, Vol 69, No. 2, 1990, pp. 130-135.
11. Semiatin, S.L., Seetharaman, V., Weiss, I., "The thermomechanical processing of Alpha/Beta titanium alloys", *J. Mat.* 33, 1997.
12. Scott E. Schoenfeld and Bimal Kad, "Texture effects on shear response in Ti-6Al-4V plates", *International Journal of Plasticity*, Volume 18, Issue 4, April 2002, Pages 461-486.
13. K. Goebbels, "Structural analysis by scattered ultrasonic radiation", *Research Techniques in Nondestructive Testing*, Academic Press, New York, NY, 1980, pp. 87-157.
14. B. R. Tittmann and L. Ahlberg: "Attenuation and grain noise parameters in Ni-base alloy", *Review of Progress in Quantitative NDE*, Vol. 2A, eds. D.O. Thompson and D.E. Chimenti (Plenum, New York, 1983) p. 129-145.
15. F. J. Margetan, T. A. Gray, and R. B. Thompson: "A techniques for quantitatively measuring microstructure induced ultrasonic noise", *Review of Progress in Quantitative NDE*, Vol. 10B, eds. D.O. Thompson and D.E. Chimenti (Plenum, New York, 1991) p. 1721-1728.

16. F. J. Margetan and R. B. Thompson: "Microstructural noise in titanium alloys and its influence on the detectability of hard-alpha inclusion", *Review of Progress in Quantitative NDE*, Vol. 11B, eds. D.O. Thompson and D.E. Chimenti (Plenum, New York, 1992) p. 1717-1724.
17. F. J. Margetan, R. B. Thompson and I. Yalda-Mooshabad: "Modeling ultrasonic microstructural noise in titanium alloy", *Review of Progress in Quantitative NDE*, Vol. 12B, eds. D.O. Thompson and D.E. Chimenti (Plenum, New York, 1991) p. 1735-1742.
18. I. Yalda-Mooshabad, F. J. Margetan and R. B. Thompson: "Monte-Carlo simulation of ultrasonic grain noise", *Review of Progress in Quantitative NDE*, Vol. 12B, eds. D.O. Thompson and D.E. Chimenti (Plenum, New York, 1992) p. 1727-1735.
19. F. J. Margetan, R. B. Thompson and I. Yalda-Mooshabad: "Backscattered microstructural noise in ultrasonic tone-burst measurements", *Journal of Nondestructive Evaluation*, 1994, 13(3), p. 111.
20. J. H. Rose: "Ultrasonic backscattering from polycrystalline aggregates using time-domain linear theory", *Review of Progress in Quantitative NDE*, Vol. 10B, eds. D.O. Thompson and D.E. Chimenti (Plenum, New York, 1991) p. 1715-1720.
21. J. H. Rose: "Ultrasonic backscatter from microstructure", *Review of Progress in Quantitative NDE*, Vol. 11B, eds. D.O. Thompson and D.E. Chimenti (Plenum, New York, 1992) p. 1677-1684.
22. J. H. Rose: "Theory of ultrasonic backscatter from multiphase polycrystalline solid", *Review of Progress in Quantitative NDE*, Vol. 12B, eds. D.O. Thompson and D.E. Chimenti (Plenum, New York, 1993) p. 1719-1726.
23. Y. K. Han and Thompson, "Ultrasonic backscattering in duplex microstructures: Theory and application to titanium alloys", *Metallurgical and materials transactions*, Vol. 28A, p.91.

24. S. Ahmed and R. B. Thompson: "Influence of columnar microstructure on ultrasonic backscattering", *Review of Progress in QNDE*, Vol. 14, pp. 1617-24.
25. R. A. Sigelmann and J. M. Reid: "Analysis and measurement of ultrasonic backscattering from an ensemble of scatterers excited by sine-wave bursts", *J. Acoust. Soc. Am.*, 1973, Vol. 53, pp. 1351-1355.
26. E. L. Madsen, M. F. Insana, and J. A. Zagzebski: "Method of data reduction for accurate determination of acoustic backscatter coefficients", *J. Acoust. Soc. Am.* 1984, Vol. 76, pp. 912-923.
27. R. J. Roe, "Description of crystallite orientation in polycrystalline materials. III. General solution to pole figure inversion", *J. of Appl. Phys.*, 36(6), (1965) p. 2024.
28. R. J. Roe, "Inversion of pole figures for materials having cubic crystal symmetry", *J. of Appl. Phys.*, 37(5), (1964) p. 2069.
29. F. J. Margetan, I. Yalda-Mooshabad, R. Bruce Thompson, "Predicted gated-peak grain noise distributions for ultrasonic inspections of metals", *Review of Progress in QNDE*, Vol. 15B, eds. D.O. Thompson and D.E. Chimenti (Plenum, New York, 1996) p.1509-1516.
30. I. Yalda-Mooshabad and R. B. Thompson, "Influence of texture and grain morphology on the two-point correlation of elastic constants: theory and implication on ultrasonic attenuation and backscattering" *Review of Progress in QNDE*, Vol. 14B, eds. D.O. Thompson and D.E. Chimenti (Plenum, New York, 1996) p.1939-1946.

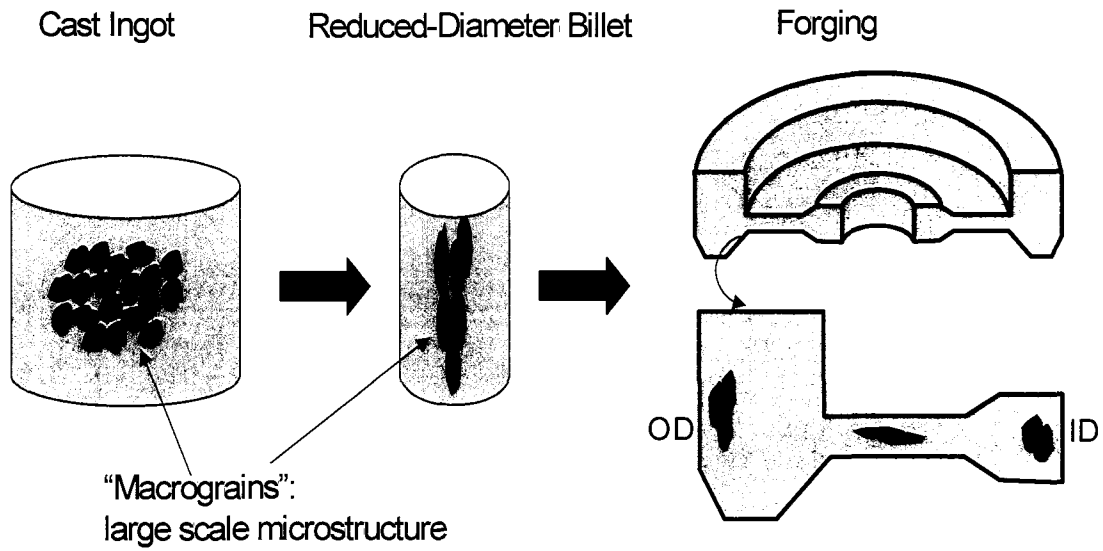


**FIGURE 1.** Typical manufacturing thermo-mechanical processing of forging.

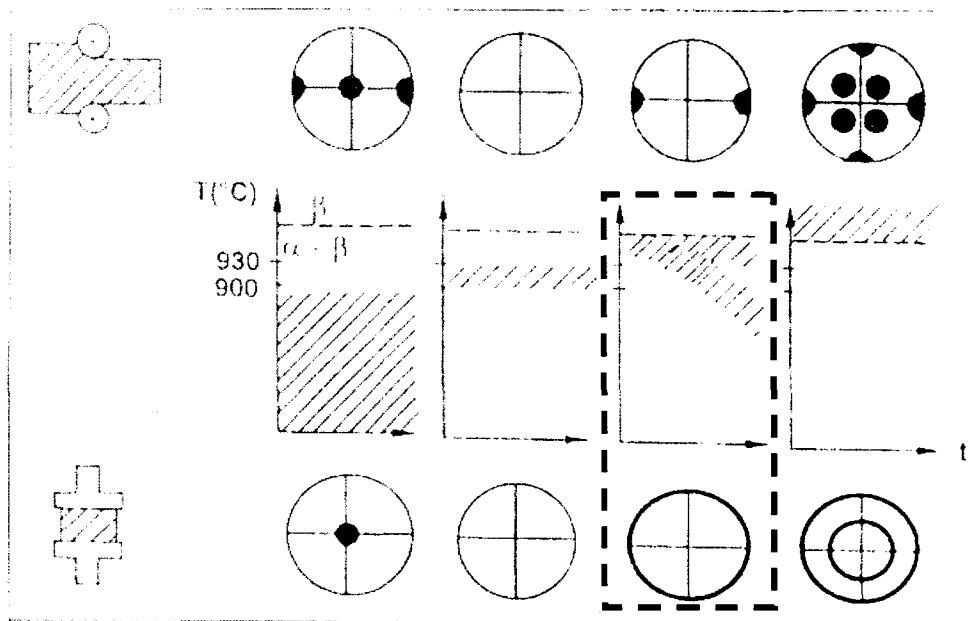


**FIGURE 2.** Schematic representation of the relationship among working method (rolling at top, axisymmetric forging at bottom), working temperature and texture for Ti-6Al-4V. Courtesy of Ref. [5].

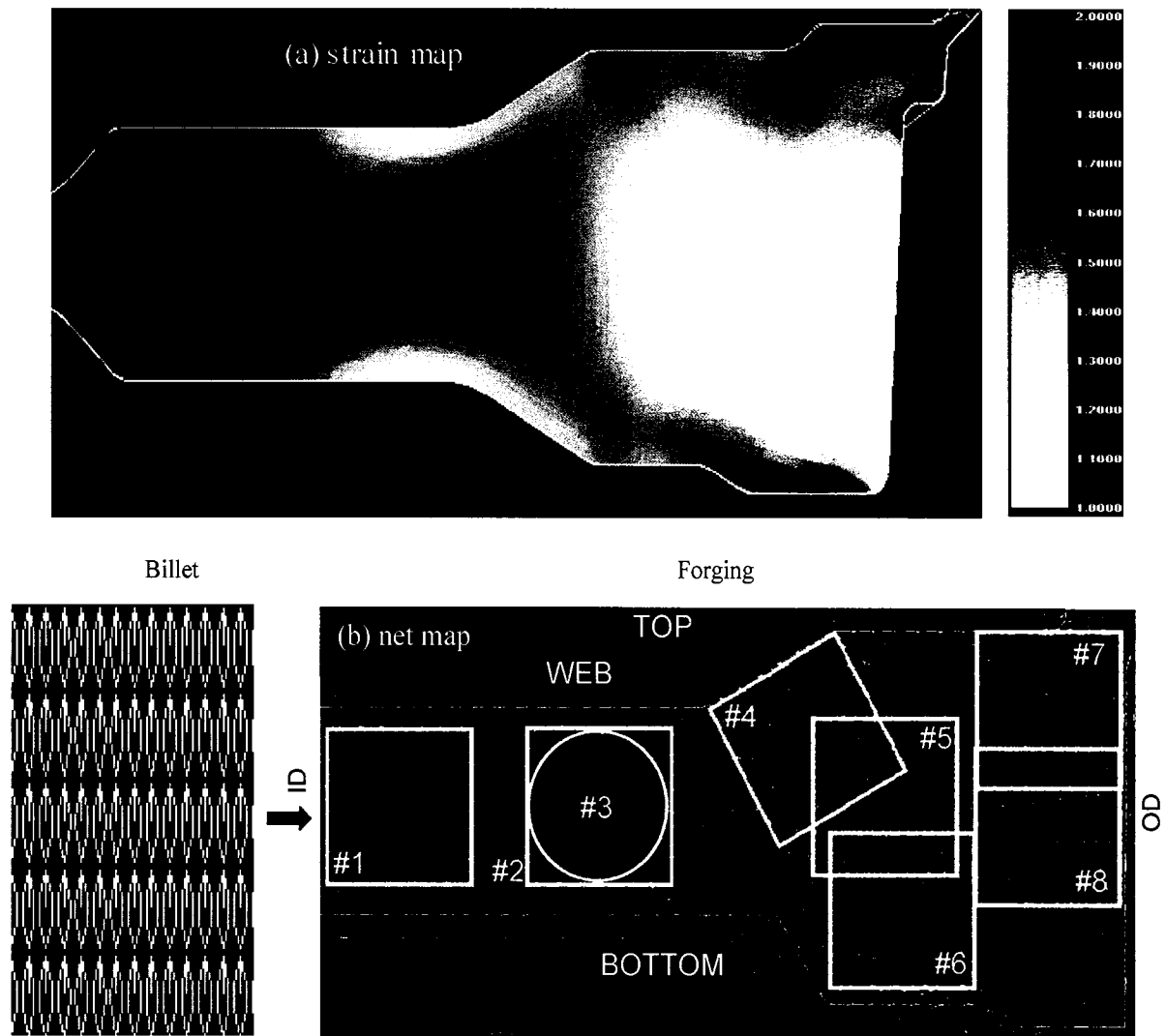


**FIGURE 3.** DEFORM simulation for a axisymmetric forged disk, showing one-half of the cross-section in the radial-axial plane. a). Strain map; b). Net map, starting from 7:1 ellipsoids in the billet.



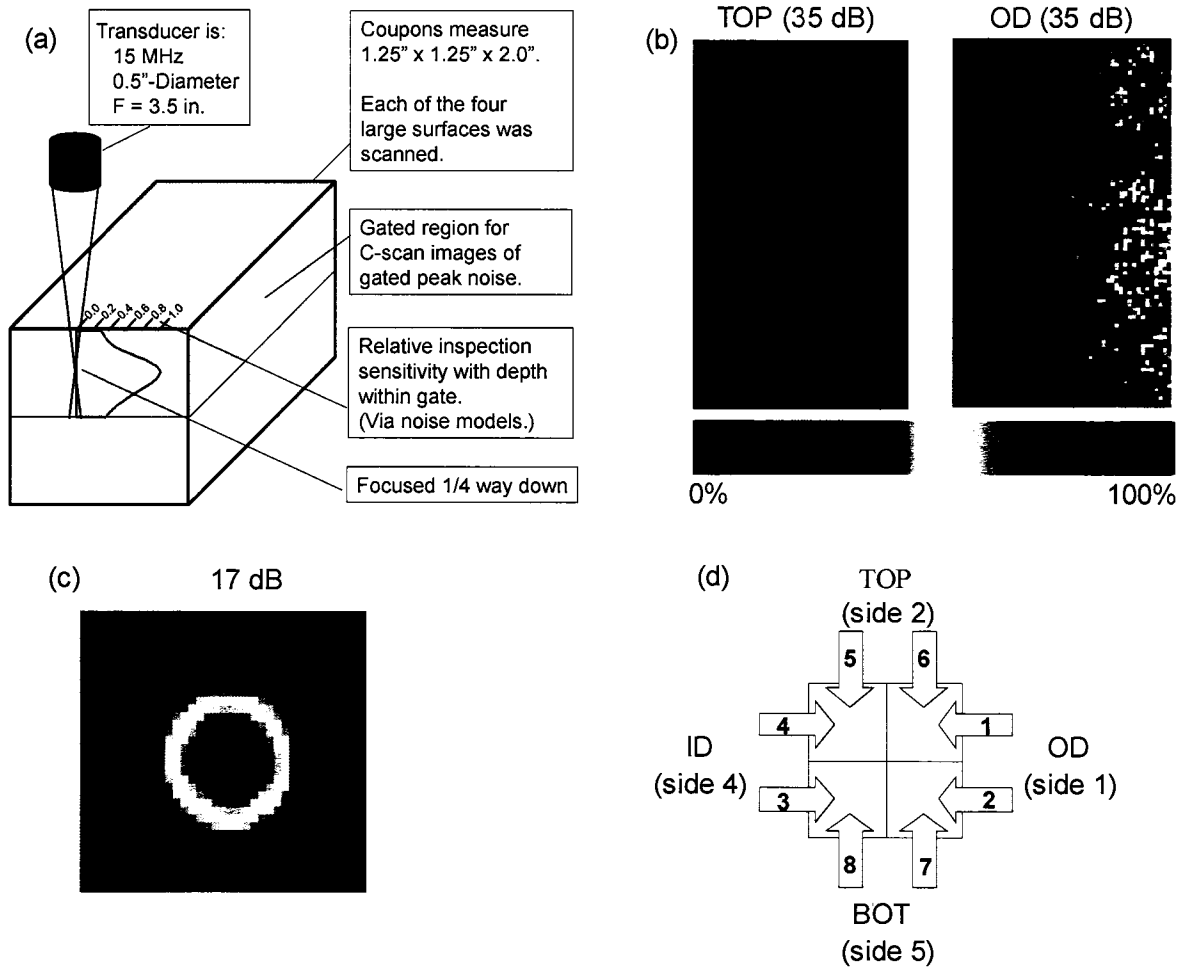


**FIGURE 4.** (a) Experiment setup for grain noise acquisition. (b). C-scan images of the backscattered noise through the TOP and OD faces of coupon #5. (c). C-scan image of a #1 FBH in a low-attenuation IN100 reference block at the depth of 0.5". (d). The combinations of the inspection direction and quadrant.

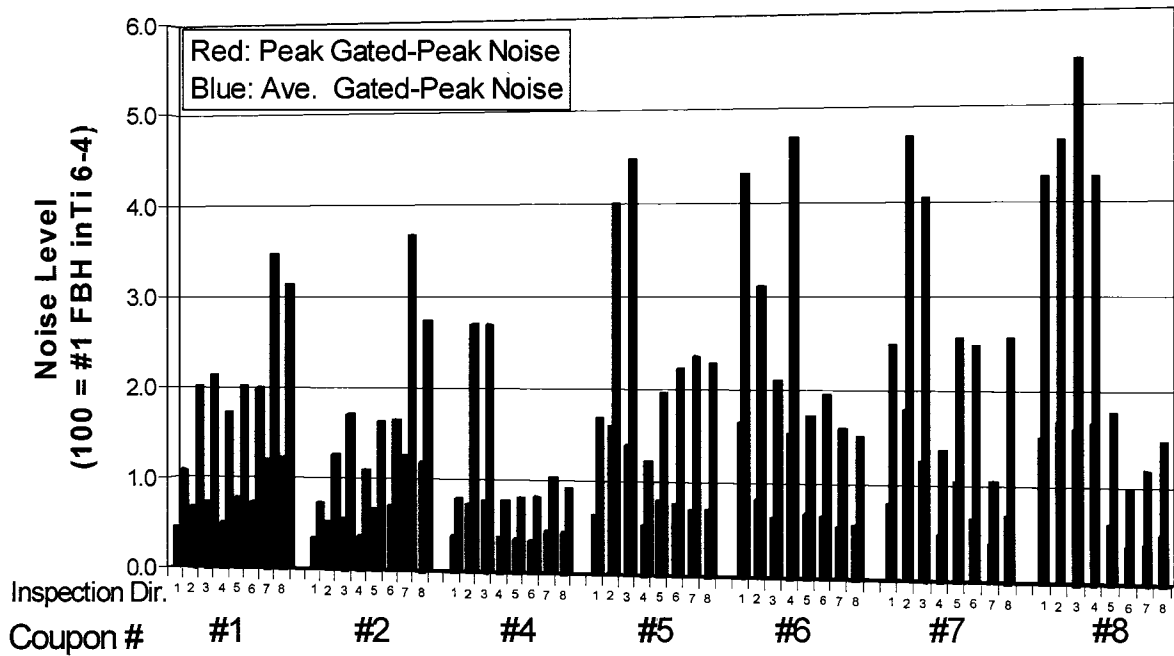


**FIGURE 5.** Peak (red bar) and average (blue bar) gated-peak noise levels in 7 coupons, relative to the estimated amplitude of a #1 FBH at the same depth. Results are shown for all inspection directions.

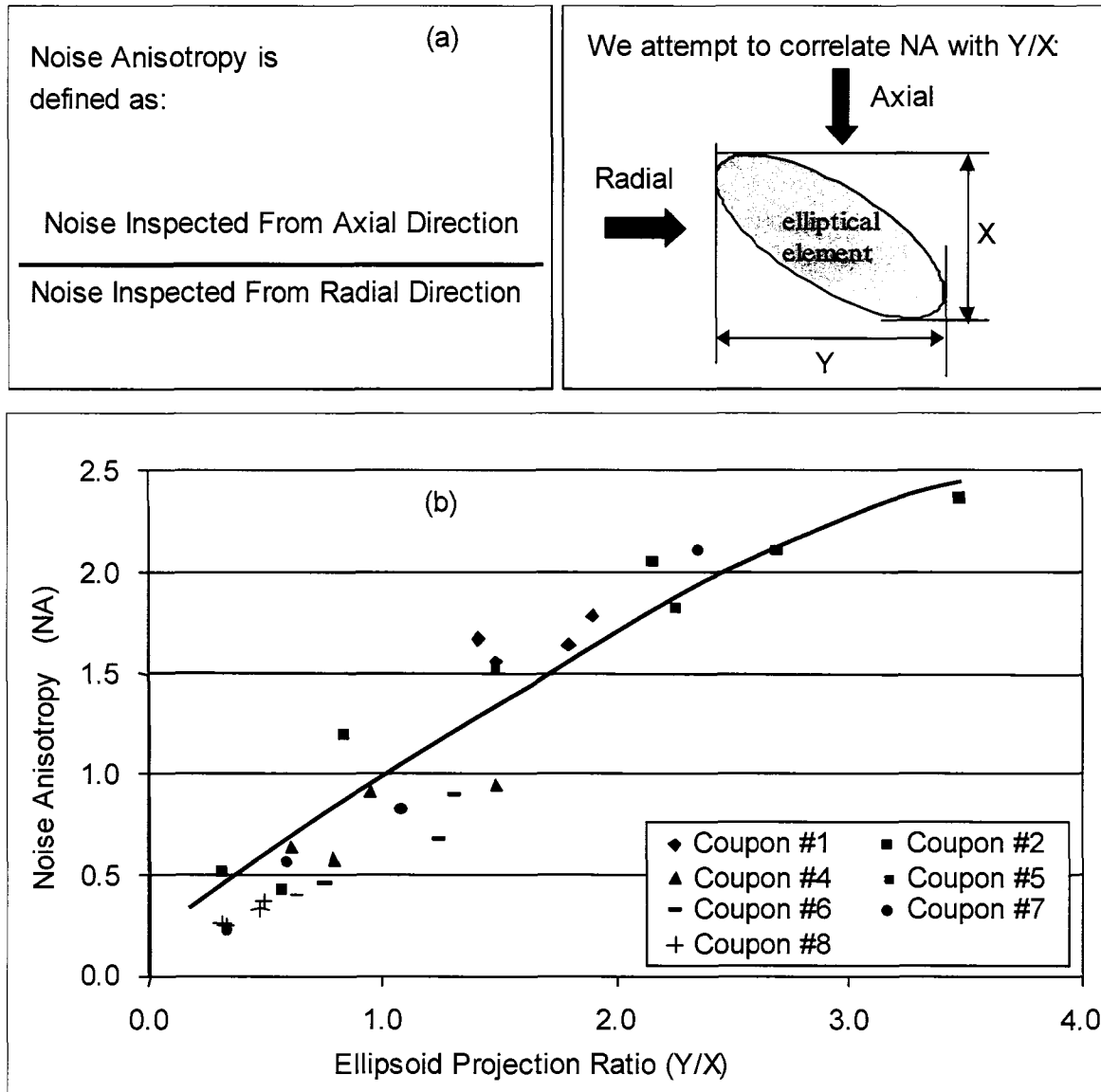


**FIGURE 6.** (a). The definitions of noise anisotropy (NA) and ellipsoid projection ratio (Y/X). (b) Correlation between noise anisotropy and ellipsoid projection ratio.

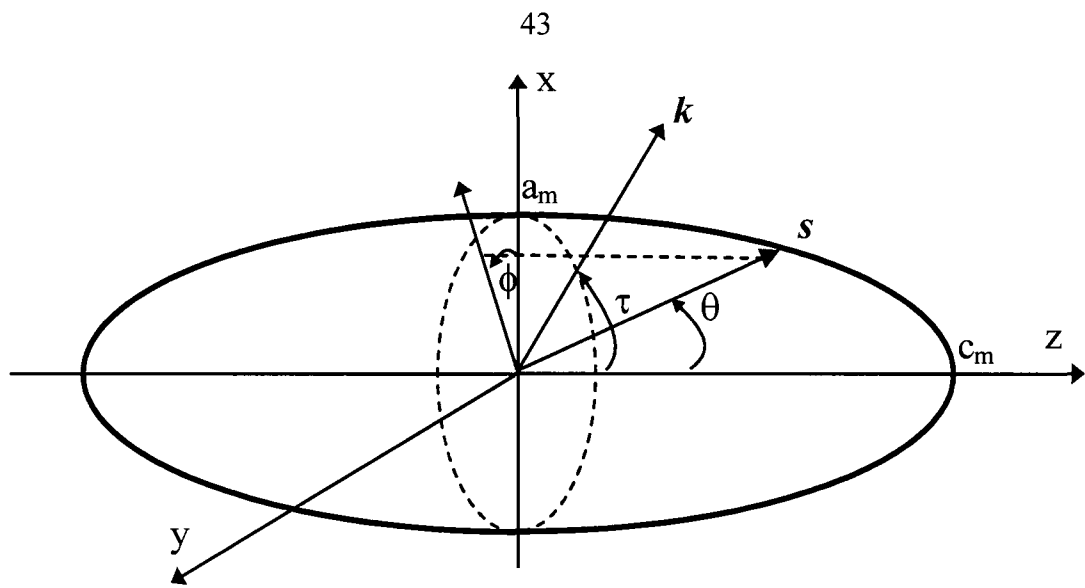


**FIGURE 7.** Geometry of an ellipsoidal scattering element, sonic beam propagation is assumed to be parallel to vector  $k$ .

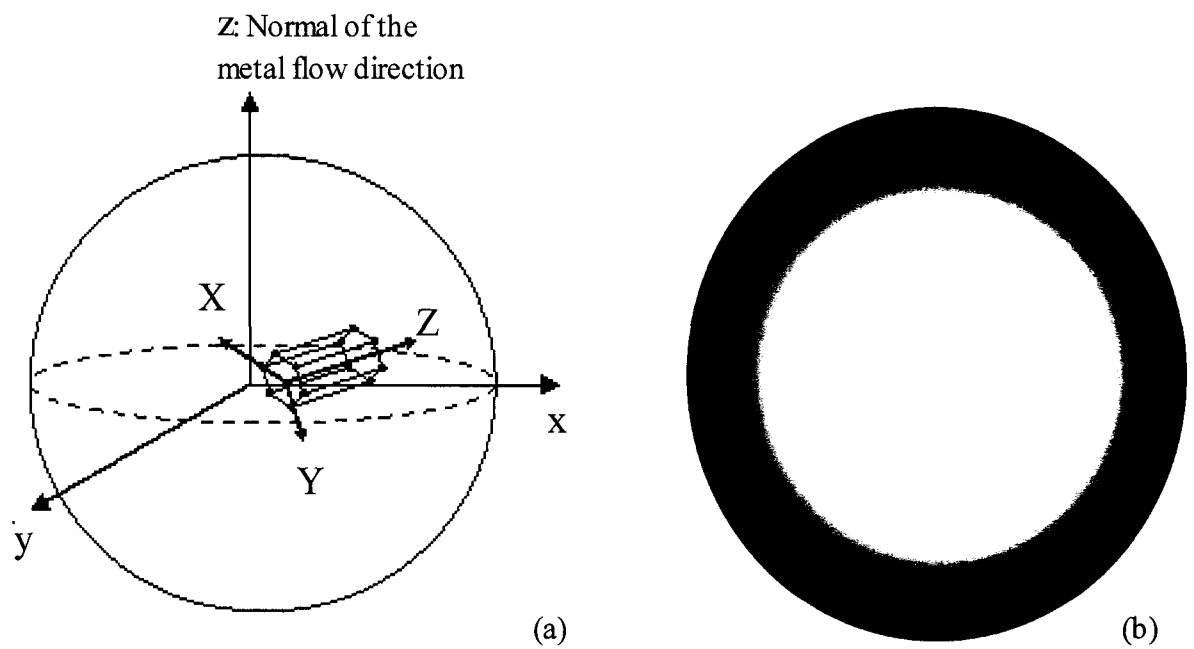


**FIGURE 8.** a). Crystallite alignment within forging (shown with stereographic projection sphere). b). The resulting (0001) pole figure.

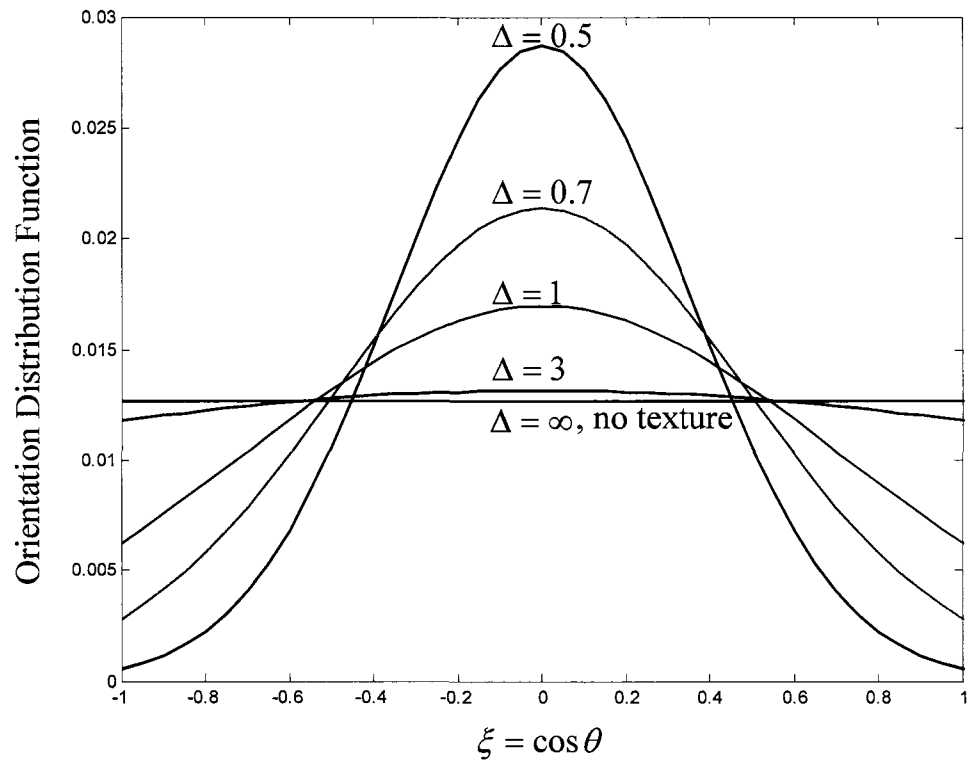


**FIGURE 9.** One-variant ODF at different  $\Delta$

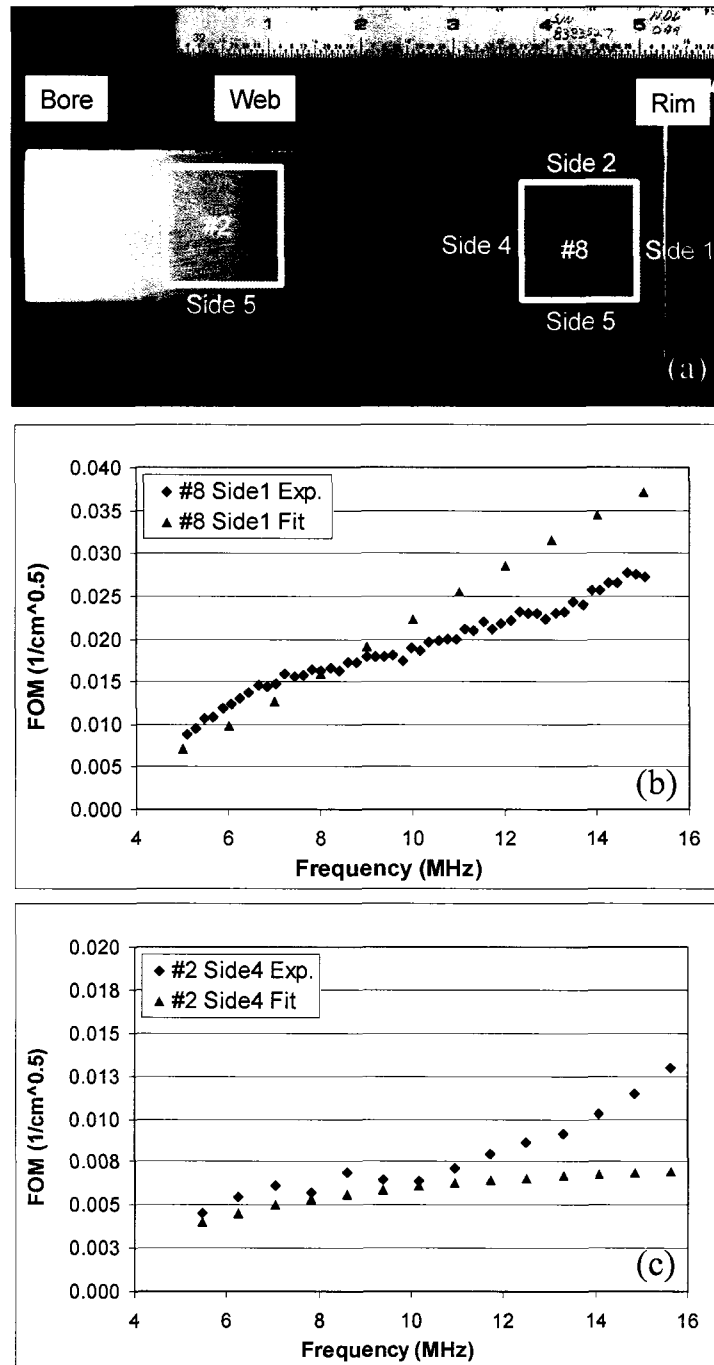


**FIGURE 10.** (a). Relative locations of two coupons used in fitting. (b-c) Comparison of measured and predicted FOM-vs-frequency curves for the optimal choices of the model parameters. (b) Data from coupon #8 sides 1, (c) Data from coupon #2 side 4.

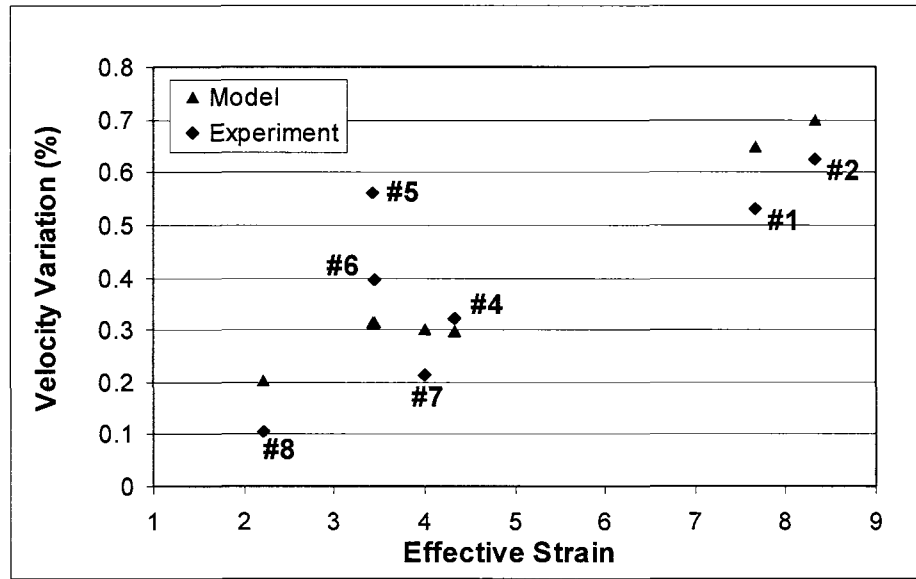


**FIGURE 11.** Velocity variation via effective strain: experiment and model prediction.

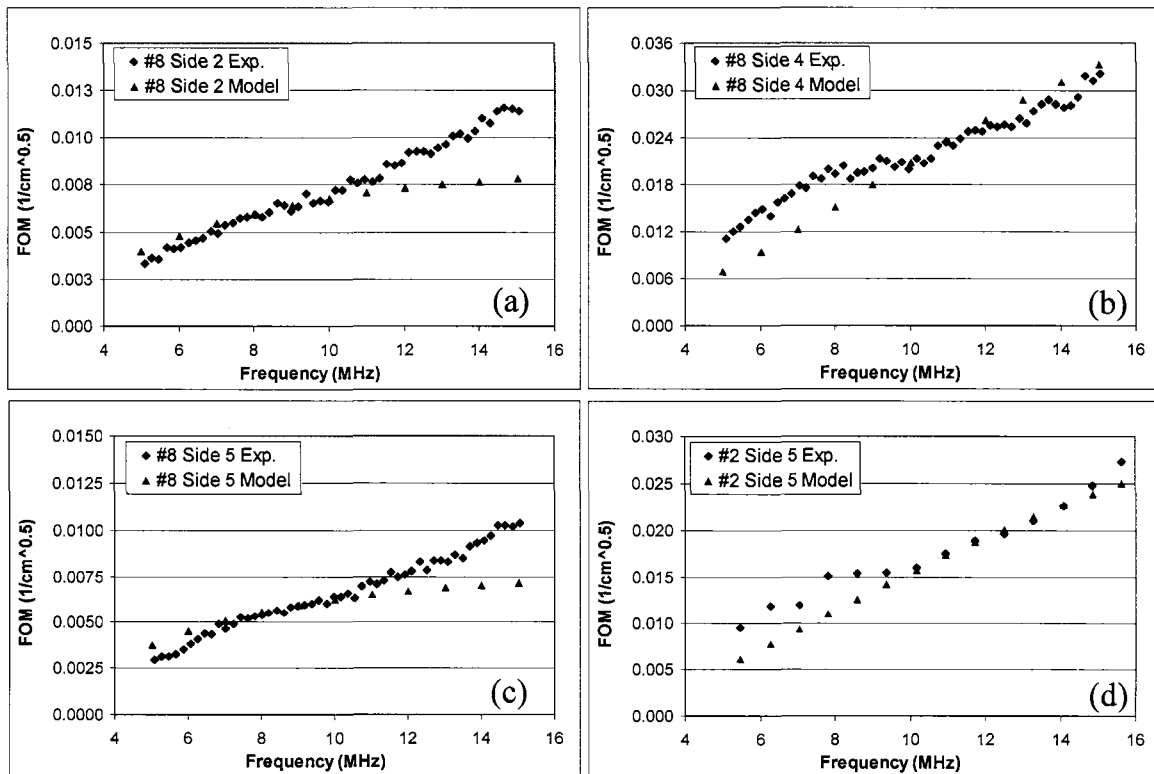


**FIGURE 12.** Comparison of experiments and model predictions, FOM vs. frequency. (a). Coupon #8 side 2; (b). Coupon #8 side 4; (c). Coupon #8 side 5; (d). Coupon #2 side 4.

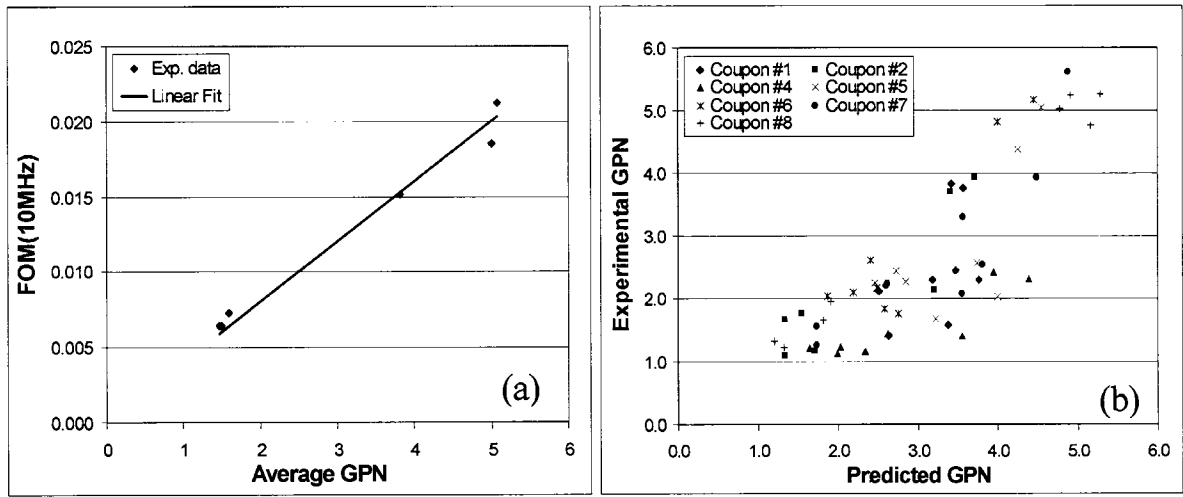


**FIGURE 13.** a). An approximation scaling factor which relates average GPN with FOM at 10MHz, as deduced from measured values for selected coupons. b). Comparison between measured and predicted average GPN amplitudes in each quadrant of each coupon.



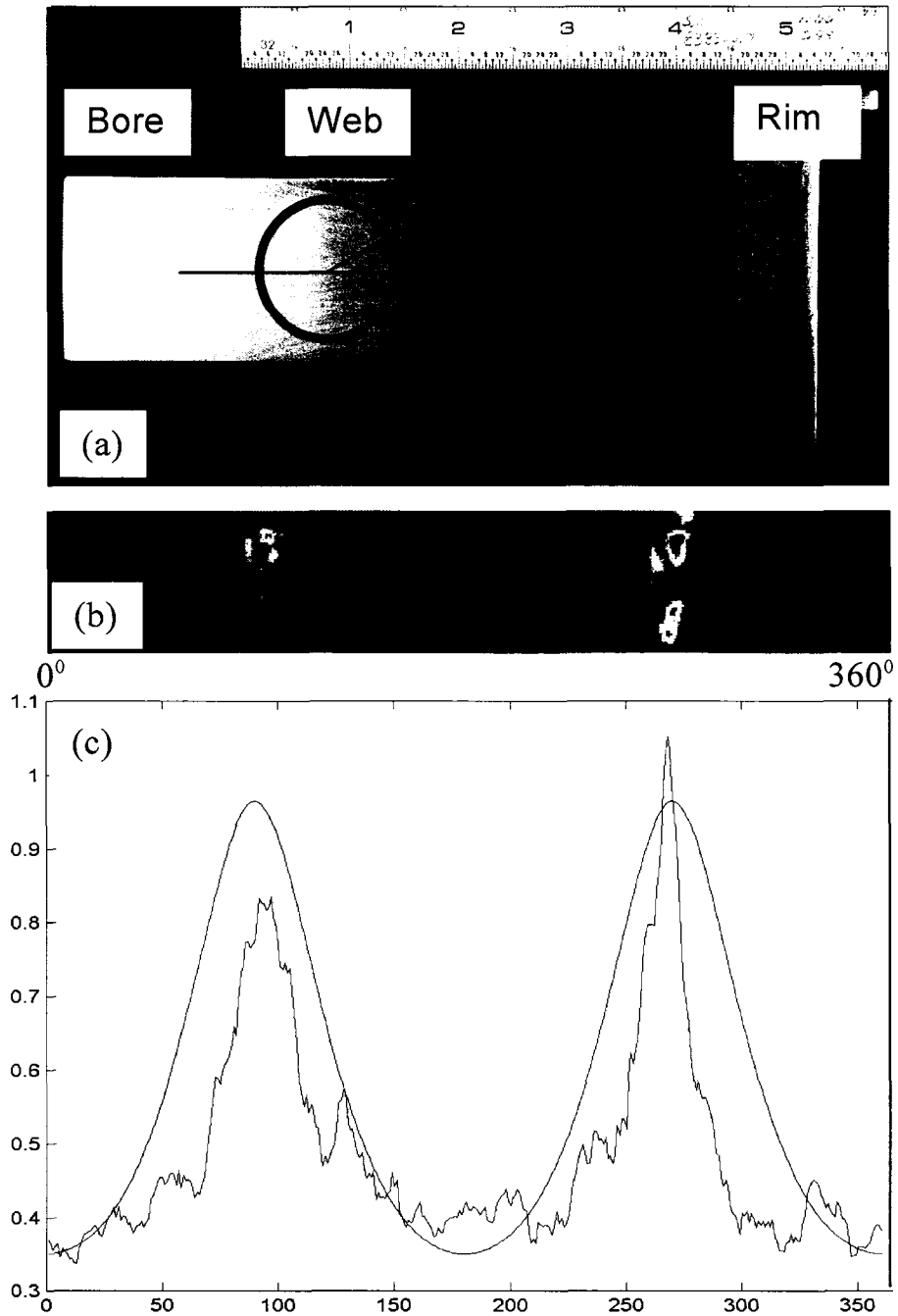


**FIGURE 14.** a). Cylindrical coupon location and the angle  $\tau$  definition. b). The experimental GPN angular dependence. c). The comparison between experiment and prediction.

## CHAPTER 2. THE SPATIAL CORRELATION OF THE BACKSCATTERED ULTRASONIC GRAIN NOISE: THEORY AND EXPERIMENTAL VALIDATION

A paper to be submitted to the Journal of the Acoustical Society of America

Linxiao Yu, R. B. Thompson, and F. J. Margetan

Center for Nondestructive Evaluation

Iowa State University

Ames, IA 50011

**ABSTRACT.** The correlation of backscattered ultrasonic grain noise has important implications in practical inspections. For example, the spatial correlation length (SCL) of the backscattered noise is a crucial quantity in designing advanced de-noising algorithm in image processing, and it is also an important component in some critical simulations to evaluate the distribution of the gated-peak noise (GPN), which in turn is indispensable for the estimation of probability of detection (POD) or frequency of false calls. In this paper, an existing backscattered grain noise theory based on the single scattering assumption and the “Born” approximation is extended to study the grain noise correlation in space, leading to a formal theory predicting the spatial correlation of the backscattered grain noise. A special form of the theory for a Gaussian beam is also presented to demonstrate that the specimen microstructure and the overlap of the incident beam are the important physical parameters controlling the grain noise spatial correlation. To validate the theory, a series of experiments are designed to collect grain noise signals from a waspalloy alloy specimen, which has locally-uniform equiaxed microstructure. The theory is numerically evaluated and the results are compared with the experiments. Excellent agreements between predictions and measurements are observed. Further discussions were given to show the details of how the beam overlap controls the grain noise spatial correlation.

## 1. INTRODUCTION

Because of the important implications in nondestructive evaluation (NDE) and materials characterization, backscattered ultrasonic grain noise has been an active research topic in the past decade in the NDE community. A great amount of research efforts was devoted to the theory development and validation, experiments and correlations, as well as numerical simulations [1-21]. In this paper, existing backscattered grain noise theory is extended to study the grain noise correlation in space, leading to a formal theory predicting the spatial correlation of the backscattered grain noise. A special form of the theory for a Gaussian beam is also presented to show that the specimen microstructure and the overlap of the incident beam are the important physical parameters controlling the grain noise spatial correlation.

Grain noise spatial correlation is illustrated in Figure 1. Backscattered ultrasonic grain noise waveforms were collected at different transducer locations,  $x$  and  $x'$ . The collected A-scan waveform pairs, with different transducer interval distances ( $|x-x'|$ ), are plotted in Figure 1b. We can see that when the two transducers are 0.02" (0.508 mm) apart, the collected grain noise waveforms are slightly misaligned. The waveform coherency decreases with the increase of the interval. When the two transducers are 0.1" (2.54 mm) apart, we even can not tell the similarity between these two waveforms.

We use the spatial correlation coefficient ( $SCC$ ), as defined in Eq. (1) [22], to quantify the semblance or coherency between the noise waveforms  $V(x, t)$  and  $V(x', t)$  acquired at  $x$  and  $x'$ . The definition measures the phase component similarity between the two waveforms because the influences of the signal amplitudes are removed by the normalization of signal energy (denominator). Obviously,  $SCC$  is a function of  $|x-x'|$ . When  $x = x'$ ,

$$SCC(x-x') = \frac{\int V(x, t) \times V(x', t) dt}{\sqrt{\int [V(x, t)]^2 dt \times \int [V(x', t)]^2 dt}} \quad (1)$$

$SCC = 1$ , which means the two grain noise waveforms are identical except the possible scaling difference.  $SCC$  decreases as  $|x - x'|$  increases.  $SCC = 0$  means the two signal are orthogonal, and  $SCC = -1$  means the two signal are identical but with opposite polarization. The length corresponding to  $SCC = 0.37$  ( $1/e$ ) is defined as the noise spatial correlation length ( $SCL$ ).

The spatial correlation of backscattered ultrasonic grain noise has important implications in practical ultrasonic inspections. For example, the C-scan image constructed by using the gated-peak signals (containing both flaw and noise signal) is the routine output in most industrial UT (ultrasonic testing) operations. The spatial correlation of the backscattered grain noise is a crucial quantity in designing advanced de-noising algorithm in image processing [23, 24]. In addition, grain noise  $SCL$  is an important component in some critical simulations [25] to evaluate the distribution of the gated-peak noise (GPN), which in turn is indispensable for the estimation of probability of detection (POD) or frequency of false calls [34]. Figure 2 shows the experimental and simulated GPN from a titanium alloy specimen with varying microstructure from one end to the other. Good qualitative agreements between experiment and simulation can be achieved only when using the appropriate  $SCL$ .

The theory developed in this paper is based on the single scattering assumption and the “Born” approximation, and it is capable of predicting the grain noise spatial correlations for different experimental scenarios (for example, different transducer parameters; different beam focal conditions within the metal; different grain size, etc). The paper is organized as follows. We first briefly show the derivation of the theory in the general form. A special form for a Gaussian beam is then presented, from which we can identify the important physical parameters controlling the grain noise spatial correlation. The theory is numerically evaluated for different experimental circumstances. To validate the theory, a series of experiments are designed to collect grain noise signals from a waspalloy alloy specimen, which has a single-phase uniform equiaxed microstructure. The predicted grain noise spatial

correlations are compared with the measurements. Excellent agreements between the predictions and experiments are observed. Further efforts are made to show the details of how the important physical parameters control the grain noise spatial correlation.

## **2. THEORY FOR BACKSCATTERED ULTRASONIC GRAIN NOISE SPATIAL CORRELATION**

### **2. 1 THEORY IN GENERAL FORM**

The theoretical foundation for the backscattered ultrasonic grain noise was laid out by Rose [1-3], who relates backscattered ultrasonic grain noise levels to the physical properties of the microstructure. Using the single-scattering assumption and the “Born” approximation, Rose developed a rigorous stochastic theory for the backscattered noise power, which led to explicit expressions for backscattering in randomly orientated, equiaxed, single-phase or multi-phase polycrystals. Han and Thompson’s work [12, 13] extended Rose’s theory to the case of duplex microstructures, which may contain texture and elongated microstructural features with correlations in grain orientation. The experimental measurement model for the backscattered ultrasonic grain noise was developed by Margetan et al. [4-8]. They modeled the received backscattered grain noise power to be equal to the sum of the power backscattered from the individual crystallites, by assuming that the phases of these signals would be random. In this model, they defined a characteristic material parameter, the so-called “figure of merit (*FOM*)”, to measure the noise generation capability of the material, which was shown to be identical to the square root of the backscattering coefficient ( $\eta$ ) used in Rose’s paper [1-3]. In the current paper, we will extend the earlier theoretical work [1-3, 12] to predict the spatial correlation of the backscattered ultrasonic grain noise. We will follow the procedures developed in earlier experimental investigations [4-8] to measure the backscattered grain noise. The spatial correlations of the measured grain noise signals will be compared with the predictions made by the theory.

The coordinate system used to derive the theory is shown in Figure 3. The grain noise signals from a metal specimen are collected using an immersion UT system. When the transducer central ray is aligned with the  $Z$ -axis, the transducer response  $\delta\Gamma$  at frequency  $f$  due to the presence of grain scatterer within a volume  $\Omega$  can be written as Eq. (2):

$$\delta\Gamma(f) = \frac{j\omega}{4P(\omega)} \int_{\Omega} d^3\vec{r} \left[ \omega^2 \delta\rho(\vec{r}) u_{1i}(\vec{r}) u_{2i}(\vec{r}) - \delta C_{ijkl}(\vec{r}) u_{1i,j}(\vec{r}) u_{2k,l}(\vec{r}) \right] \quad (2)$$

Here  $\omega$  is the angular frequency.  $P(\omega)$  is the exciting electrical power from the pulser.  $\delta\rho(\vec{r})$  and  $\delta C_{ijkl}(\vec{r})$ , as defined as in Eq. (3) and Eq. (4), are the variations of the density and elastic constant at the specified point  $\vec{r}$  from the homogeneous medium.  $C_{ijkl}(\vec{r})$  and  $\rho(\vec{r})$  are the spatially varying elastic constant tensor and density of the inhomogeneous medium at the location  $\vec{r}$ .  $C_{ijkl}^v$  and  $\rho^v$  are the counterparts of  $C_{ijkl}(\vec{r})$  and  $\rho(\vec{r})$  for the homogeneous medium.  $u_{1i}(\vec{r})$  and  $u_{2i}(\vec{r})$  are wave displacements that would exist at the location  $\vec{r}$  with (total) and without (incident) the inhomogeneities.  $u_{1i,j}(\vec{r})$  and  $u_{2k,l}(\vec{r})$  is the spatial derivatives of  $u_{1i}(\vec{r})$  and  $u_{2i}(\vec{r})$ . Note that the summation of convention is assumed for repeated subscript indices.

$$\delta\rho(\vec{r}) \equiv \rho(\vec{r}) - \rho^v \quad (3)$$

$$\delta C_{ijkl}(\vec{r}) \equiv C_{ijkl}(\vec{r}) - C_{ijkl}^v \quad (4)$$

$$u_{1i}(\vec{r}) = u_{2i}(\vec{r}) \quad (5)$$

In the “Born” approximation, stated in Eq. (5), one assumes that the total field (incident field plus scattered field) equal to the incident field. If one makes the additional assumption

that the density variations throughout the interested volume  $\Omega$  are negligible, Eq. (2) can be simplified as Eq. (6):

$$\delta\Gamma(f) = \frac{-j\omega}{4P(\omega)} \int_{\Omega} d^3\vec{r} \left[ \delta C_{ijkl}(\vec{r}) \varepsilon(\vec{r})^2 \right] \quad (6)$$

where,  $\varepsilon(\vec{r})$  is the elastic strain at the location  $\vec{r}$ .

As illustrated in Figure 3, backscattered grain noise signals,  $\delta\Gamma(t, \vec{x1})$  and  $\delta\Gamma(t, \vec{x2})$ , the Fourier transformations of  $\delta\Gamma(f, \vec{x1})$  and  $\delta\Gamma(f, \vec{x2})$  respectively, are acquired at two transducer positions  $(x1, 0, 0)$  and  $(x2, 0, 0)$ . The spatial correlation between the grain noise signals is defined as in Eq. (7), which can be further simplified as in Eq. (8) by changing variables and using the reality property of the grain noise signal. The “ $\langle \dots \rangle$ ” notation represents spatial ensemble average and the superscript “ $*$ ” represents complex conjugate.

$$\begin{aligned} C(\vec{x1}, \vec{x2}) &= \left\langle \int \delta\Gamma(t, \vec{x1}) \delta\Gamma(t, \vec{x2}) dt \right\rangle \\ &= \left\langle \int dt \int_{-\infty}^{\infty} df \int_{-\infty}^{\infty} df' \left[ \delta\Gamma(f, \vec{x1}) \delta\Gamma(f', \vec{x2}) e^{j2\pi t(f+f')} \right] \right\rangle \end{aligned} \quad (7)$$

$$\begin{aligned} C(\vec{x1}, \vec{x2}) &= \left\langle \int_{-\infty}^{\infty} df \int_{-\infty}^{\infty} df'' \left[ \delta\Gamma(f, \vec{x1}) \delta\Gamma^*(f'', \vec{x2}) \right] \delta(f - f'') \right\rangle \\ &= \left\langle \int_{-\infty}^{\infty} df \left[ \delta\Gamma(f, \vec{x1}) \delta\Gamma^*(f, \vec{x2}) \right] \right\rangle \end{aligned} \quad (8)$$

Put Eq. (6) into Eq. (8), we can find:

$$\begin{aligned} C(\vec{x1}, \vec{x2}) &= \left\langle \int_{-\infty}^{\infty} df \left\{ \left[ \frac{\omega^2}{16P(\omega)P(\omega)^*} \right] \right. \right. \\ &\quad \left. \left. \int_{-\infty}^{\infty} d^3\vec{r1} \left[ \delta C_{ijkl}(\vec{r1}) \varepsilon_0^2(\vec{r1} - \vec{x1}) \right] \int_{-\infty}^{\infty} d^3\vec{r2} \left[ \delta C_{ijkl}(\vec{r2}) \varepsilon_0^2(\vec{r2} - \vec{x2}) \right] \right\} \right\rangle \end{aligned} \quad (9)$$

Note that, the  $\vec{\varepsilon}(\vec{r})$  term in Eq. (6) is the general expression, and the  $\varepsilon_0(\vec{r1}-\vec{x1})$  and  $\varepsilon_0(\vec{r2}-\vec{x2})$  are the specific forms for transducer locations  $\vec{x1}$  and  $\vec{x2}$ . Assume the elastic strain is in the form of Eq. (10), and change integral variables as Eq. (11) - (12):

$$\varepsilon_0 = A(f) p(f, \vec{r}) e^{-jkz} \quad (10)$$

$$\vec{r} = \frac{\vec{r1} + \vec{r2}}{2} \quad (11)$$

$$\vec{s} = \vec{r2} - \vec{r1} \quad (12)$$

We can re-write Eq. (9) as Eq. (13):

$$C(\vec{x1}, \vec{x2}) = \int_{-\infty}^{\infty} df \left\{ \left[ \frac{\omega^2}{16P(\omega)P(\omega)^*} \right] A^2(f) A^{*2}(f) \right. \\ \left. \int_{-\infty}^{\infty} d^3\vec{r} \left\langle \int_{-\infty}^{\infty} d^3\vec{s} \left[ \delta C_{ijkl}(\vec{r} - \frac{\vec{s}}{2}) \delta C_{ijkl}(\vec{r} + \frac{\vec{s}}{2}) p^2(f, \vec{r} - \frac{\vec{s}}{2} - X1) p^{*2}(f, \vec{r} + \frac{\vec{s}}{2} - X2) e^{2jks_3} \right] \right\rangle \right\} \quad (13)$$

The  $A(f)$  term refers to the strain amplitude, and involves transducer efficiency, bandwidth, wave attenuation and transmission through the water/solid interface. The  $p(f, \vec{r})$  term accounts for beam spread. The plane wave propagation term,  $e^{-jkz}$ , is not included in  $p(f, \vec{r})$ . Eq. (13) is the exact expression for the backscattered grain noise spatial correlation, within the ‘‘Born’’ approximation. If the material elastic properties vary rapidly with respect to the wave field ( $p(f, \vec{r})$  term),  $C(\vec{x1}, \vec{x2})$  can be further approximated as:



$$\begin{aligned}
C(\vec{x1}, \vec{x2}) = & \int_{-\infty}^{\infty} df \left\{ \left[ \frac{\omega^2}{16P(\omega)P(\omega)^*} \right] A^2(f) A^{*2}(f) \right. \\
& \int_{-\infty}^{\infty} d^3\vec{r} \left[ p^2(f, \vec{r} - \vec{x1}) p^{*2}(f, \vec{r} - \vec{x2}) \right] \\
& \left. \left\langle \int_{-\infty}^{\infty} d^3\vec{s} \left[ \delta C_{ijkl}(\vec{r} - \frac{\vec{s}}{2}) \delta C_{ijkl}(\vec{r} + \frac{\vec{s}}{2}) e^{2jks_3} \right] \right\rangle \right\}
\end{aligned} \tag{14}$$

Note that, by this approximation, the first order effect of the grain size has been factored out of the integral of  $\int_{-\infty}^{\infty} d^3\vec{s} [ \ ]$  in Eq.(13). The  $\left\langle \int_{-\infty}^{\infty} d^3\vec{s} \left[ \delta C_{ijkl}(\vec{r} - \frac{\vec{s}}{2}) \delta C_{ijkl}(\vec{r} + \frac{\vec{s}}{2}) e^{2jks_3} \right] \right\rangle$  term in Eq.(14) is the spatial Fourier transformation of the two-point correlation of elastic constants, which is directly proportional to the backscattering coefficient  $\eta$ , or the square of *FOM* of the metal specimen. The *FOM* of a particular microstructure can be calculated using the program developed in earlier work [12, 13, 15, 16, 18]. Since  $p(f, \vec{r})$  are beam spread terms, the volume integral of  $p^2(\vec{r} - \vec{x1}) p^{*2}(\vec{r} - \vec{x2})$  that appears as a factor in Eq.(14) physically means the overlap of the incident ultrasonic beams at the two transducer positions, which can be evaluated using the Multi-Gaussian beam model [26]. Note that the  $\left[ \frac{\omega^2}{16P(\omega)P(\omega)^*} \right] A^2(f) A^{*2}(f)$  term in Eq.(14) contains the system and transducer efficiency. Since we do not have explicit expressions for these quantities that can be easily evaluated, the grain noise spatial correlation can not be directly computed using Eq.(14).

To overcome this problem, we follow the calibration procedure proposed in reference [27]. As shown in Figure 4, a fused quartz (FQ) specimen is used as a reference block, and the back-wall signal of the reference block (the incident beam is normal to the sample front

surface) is acquired using the same UT measurement system. According to the reference [27], the measured back-wall signal spectrum  $\Gamma_{Ref}(f)$  can be written as:

$$\Gamma_{Ref}(f) = \beta T_{01} T_{10} R_{11} D(Z_{0Ref}, Z_{1Ref}, f) e^{-j[k_0 Z_{0Ref} + k_1 Z_{1Ref}]} e^{-[2\alpha_0 Z_{0Ref}]} \quad (15)$$

Here  $\beta$  is the system and transducer efficiency. The subscript “Ref” indicates values for the reference experiment. The subscripts “0” and “1” indicate water and solid.  $T_{01}$  and  $T_{10}$  are the liquid-solid and solid-liquid interface plane wave transmission coefficients at normal incidence.  $R_{11}$  is the plane wave reflection coefficient of the back solid-liquid interface at normal incidence. The term  $D(Z_{0Ref}, Z_{1Ref}, f)$  accounts for the effects of diffraction, which can be evaluated by using the Multi-Gaussian beam model [26].  $k_0$  and  $k_1$  are the wave numbers in water and FQ respectively.  $Z_{0Ref}$  and  $Z_{1Ref}$  are the water path and thickness of the FQ.  $\alpha_0$  is the water attenuation. It is assumed that the attenuation of the FQ block is negligible.

If we write down the explicit expression for  $A(f)$  [35] and use the relationship between  $P(\omega)$  and  $\beta$  (as stated in Eq. (26) of reference [27]), we can extract the system and transducer efficiency and eventually get a computable expression for the spatial correlation of the backscattered ultrasonic grain noise as shown in Eq. (16). The detailed derivation of the theory can be found in the appendix of [35].

$$C(\vec{x1}, \vec{x2}) = const. \int_{-\infty}^{\infty} df \left\{ \left[ \frac{|\delta\Gamma_{Ref}(f)|^2 e^{-4\alpha_0 d} e^{-4\alpha_1 Z_c} FOM(f)^2}{k^2 |D(Z_{0Ref}, Z_{1Ref}, f)|^2} \right] \int_{-\infty}^{\infty} d^3 \vec{r} \left[ p^2(\vec{r} - \vec{x1}) p^{*2}(\vec{r} - \vec{x2}) \right] \right\} \quad (16)$$

The “*const*” term in Eq.(16) is a scaling factor, involving easily known quantities such as wave speed, densities, plane wave transmission and reflection coefficients. Since our definition of SCC in Eq. (7) is normalized to value of unity when  $\vec{x1} = \vec{x2}$ , this scaling factor is not important. The effect of specimen attenuation is approximated by the attenuation at the center of the time gate ( $e^{-4\alpha_1 Z_c}$ ) because the time gate (or the corresponding depth range) used in our calculation is very small (1us, or about 0.12”). The  $\alpha_1$  is the attenuation coefficient of the specimen and  $z_c$  is the depth corresponding to the center of the time gate. The “*d*” term is the water path difference used when acquiring the grain noise signal and the reference signal:

$$d = Z_0 - Z_{0Ref} \quad (17)$$

## 2. 2 THEORY FOR A GAUSSIAN BEAM

For many cases such as measurements made by a piston transducer, it will be necessary to evaluate Eq. (16) numerically. However, before doing so, we derived a special form of the theory for a Gaussian beam, which can provide us with more insights into the dominating physical parameters for the grain noise spatial correlation. For a Gaussian beam, the “*p*” term in Eq.(16) can be written as [28]:

$$p(x, y, z, \omega) = \left[ \frac{W_x(0)W_y(0)}{W_x(z)W_y(z)} \right]^{1/2} e^{j\{\psi_x(z)+\psi_y(z)-\psi_x(0)-\psi_y(0)\}} e^{-\frac{jk}{2} \left\{ \frac{x^2}{q_x(z)} + \frac{y^2}{q_y(z)} \right\}} \quad (18)$$

The spatial correlation will only depend on the relative values of  $\vec{x1}$  and  $\vec{x2}$ . Inserting Eq. (18) into Eq. (16), one finds:

$$C(0, x1) = \text{const.} \int_{-\infty}^{\infty} df \left\{ \left[ \frac{|\delta\Gamma_R(f)|^2 e^{-4\alpha_0 d} e^{-4\alpha_1 Z_c} FOM(f)^2}{k^2 |D(Z_{0R}, Z_{1R}, f)|^2} \right] \int_{-\infty}^{\infty} dx dy dz \left[ \frac{W_x(0)W_y(0)}{W_x(z)W_y(z)} \right]^2 e^{-\frac{2k\lambda y^2}{\pi W_y^2(z)}} e^{-\frac{k\lambda[x^2+(x-x1)^2]}{\pi W_x^2(z)}} e^{-\frac{jk[x^2-(x-x1)^2]}{\pi R_x^2(z)}} \right] \right\} \quad (19)$$

Here “ $W$ ” describes the widths of the Gaussian profile along the  $x$  and  $y$  directions at the transducer surface (initial values, denoted by 0) and at the depth of  $z$  inside the metal specimen (denoted by  $z$ ). “ $R$ ” describes the wave-front curvatures at these same positions. “ $\psi$ ” describes the “excess phases” due to the diffraction-induced beam width and wave-front curvature variations. The “ $q$ ” term appearing in Eq. (18) is a complex parameter incorporating both the wave-front curvature ( $R$ ) and beam width parameters ( $W$ ), which are explicitly shown in Eq. (19).

In Eq. (19), the  $\frac{|\delta\Gamma_R(f)|^2 e^{-4\alpha_0 d} e^{-4\alpha_1 Z_c} FOM(f)^2}{k^2 |D(Z_{0R}, Z_{1R}, f)|^2}$  term is controlled by system and transducer efficiency, bandwidth, material microstructure, ultrasonic diffraction, attenuation and transmission through the water/solid interface. The

$\left[ \frac{W_x(0)W_y(0)}{W_x(z)W_y(z)} \right]^2 e^{-\frac{2k\lambda y^2}{\pi W_y^2(z)}} e^{-\frac{k\lambda[x^2+(x-x1)^2]}{\pi W_x^2(z)}}$  factor accounts for the diffraction-induced beam width

variation and the overlap of beam amplitude profiles. The  $e^{-\frac{jk[x^2-(x-x1)^2]}{\pi R_x^2(z)}}$  factor describes the diffraction-induced wave front curvature variation and the overlap of beam phase profiles. From Eq. (19), we can clearly see that the material microstructure and the overlap of the incident sound field (both the amplitude and phase profiles) are the dominating physical parameters for the spatial correlation of the backscattered grain noise. More over, as the

transducer separation increases ( $x_l$  grows), it is the beam related factors that change and hence control the shape of spatial correlation function of the backscattered grain noise.

### 3. EXPERIMENTAL VALIDATION OF THE THEORY

To verify the theory developed in section 2 and to further understand the effects of various physical parameters on the grain noise spatial correlations, we have designed several experiments. The experiments are intended to answer the following questions.

#### 3.1 DO GRAIN NOISE SPATIAL CORRELATIONS DEPEND ON THE DISTANCE FROM FOCAL PLANE?

As shown in Figure 5, we collected grain noise signal from a 2"-thick waspalloy block. The waspalloy specimen is selected because it has a relatively simple microstructure. The site of the specimen examined has a uniform, equiaxed microstructure, and the average grain diameter is about 47  $\mu\text{m}$  (measured from metallography). The 10 MHz transducer used in our experiment had a nominal diameter ( $D$ ) of 1" and a geometrical focal length (GFL) of 10". The measured values were  $D=1.005"$  and  $\text{GFL}=11.29"$ . The noise-free FQ was selected as a reference block. We selected the water path to focus the beam on the FQ back-wall. For the waspalloy specimen, the water path was chosen to focus the beam at the depth of  $\frac{1}{4}"$  above the back wall. The transducer was scanned in a rectangle area, and the grain noise waveforms were collected at each scanning position. Since the earlier experimental work [29, 30] indicated that the  $SCL$  of the backscattered signal is small relative to the transducer diameter, we used a very fine scan step size (0.005") when scanning the transducer.

The *SCC* of the measured grain noise signal can be evaluated using Eq. (1), but we have to be careful because Eq. (1) only involves one pair of measured noise signals as observed at two transducer positions. The output of Eq. (1) is a sample correlation, and the single sample correlation is not necessarily representative of the essential physical phenomena. In other words, the correlation between any pair of noise signal is a random variable, and there is no guarantee that each realization of the data will yield the same correlation. In our calculation of the *SCC* of the experimental noise data, an ensemble average was performed [31]. Specifically, the *SCC* of each pair of the noise data with the same separation distance ( $|x-x'|$ ) was spatially averaged. Also, we wished to eliminate the influence of the electronics noise. The electronics noise can be regarded as a random signal over time so that it can be reduced by averaging over time. In our experiments, the grain noise waveforms at each scanning location were averaged 1000 times.

The noise data at three depths (time gates) are used to calculate the noise spatial correlations. The width of each time gate is 1 us corresponding to the thickness of 0.12" in the metal. The relative locations of the three time gates are marked in the right graph of Figure 5. From top to bottom, the 1st time gate is centered at 0.82" below front wall and the 2nd one is centered at the half depth of the specimen (1" below front surface). The 3rd one is centered at 1.75" below front wall corresponding to the beam focal zone.

According to Eq. (16), we developed a numerical tool which is capable of predicting the grain noise spatial correlation for different experimental scenarios. The experimental and predicted grain noise spatial correlations are plotted in Figure 6. Figure 6(a) is for the first time gate. Figure 6(b) is for the case of half depth of the specimen. Figure 6(c) is for the case of focal zone. The measured and predicted *SCLs* (The length corresponding to *SCC* drops to 0.37, i.e.  $1/e$ ) for the 3 cases are summarized in Figure 6(d). For all the three cases, the agreements between experiment and prediction are outstanding.

The theory developed in the earlier section indicates the beam overlap (both the amplitude and phase profiles) is one of the dominating parameters for the noise spatial correlation. It is illuminating to demonstrate this by a specific example. We calculated the beam profiles at the central frequency of the probe along the central line of the selected time gate [32], and the results are plotted in Figure 6(e-f). The curves in 6(e) are normalized values of the square of the beam amplitudes. For each curve, the full width corresponding to half magnitude (FWHM) drop is essentially the beam diameter [33] (for the first time gate, there is a null at the center of the amplitude profile). The phase profiles for the 3 time gates are plotted in 6(f). The results plotted in Figure 6 indicate that noise spatial correlations depend on the distance from focal plane. In the focal zone, the *SCL* is actually largest while the beam width is the smallest. Since the phase profile for the third time gate is relatively flat over a large distance (about 3 times of the corresponding *SCL*), we believe the overlap of beam amplitude profiles, particular within the -6dB points, is the controlling factor in the focal zone. Out of the focal zone, the beam amplitude profile varies more slowly and the overlap of beam phase profiles is playing an important role.

### 3.2 HOW DO THE TRANSDUCER SPECTRAL CHARACTERISTICS AFFECT GRAIN NOISE SPATIAL CORRELATION?

We selected 3 transducers to collect the grain noise signals from the same 2"-thick waspalloy specimen used in last section. The site of the specimen where the data were collected has uniform equiaxed microstructure, and the average grain diameter is about 47 $\mu$ m (measured from metallography). The 3 transducers have the same nominal parameters (0.5" diameter and 3.5" focal length) except their central frequencies (5 MHz, 10 MHz and 15 MHz respectively) and associated bandwidths. The water paths are chosen to focus the beam at 0.82" below the front surface. The width of the time gate used in our data analysis is 1 $\mu$ s, centered at the focal zone. Figure 7 summarizes the experiment arrangements and results.

Figure 7(a) shows experiment setup. Figure 7(b) plots the spectra of the 3 transducer used in our experiments. Figure 7(c-e) plot the measured and predicted grain noise spatial correlations using the 3 transducers. We find excellent agreements between the experiments and predictions for all the three transducers. Figure 7(f) plots the measured and predicted grain noise  $SCLs$ . Grain noise spatial correlation strongly depends on the transducer spectral characteristics and the  $SCLs$  decrease quickly with the increase of transducer central frequency (further calculations indicated that the probe bandwidth does not contribute such large differences).

Similarly, we calculated the beam profiles (at the central frequency of the transducers) along the central line of the time gates of interest for the 3 transducers, and the results are plotted in Figure 8(a-c). The curves in 8(a) are the beam amplitude and phase profiles for the 5 MHz probe. The amplitude curve is the normalized value of the square of the beam amplitude. The amplitude and phase profiles for the 10 MHz and 15 MHz probes are plotted in 8(b) and 8(c) respectively. We note that the amplitude for the 5 MHz transducer case varies much slower than those for the 10 MHz and 15 MHz transducer. As a result the corresponding  $SCL$  for the 5 MHz transducer is much larger than those of the 10 and 15 MHz transducers. Because the time gate we selected is centered at focal zone, it is apparent that the phase profile for each transducer varies slowly within a large distance relative to the corresponding  $SCL$ , while the amplitude profile varies much rapidly. For example, the phase profile for the 15 MHz transducer is relative flat within a width of 3 times of the corresponding  $SCL$ , but the amplitude drops to only a few percent of its peak value over the same distance. The measured  $SCLs$  for the 3 transducers and the FWHMs (beam diameter or -6dB beam width) of the matching amplitude profiles are plotted together in 8(d). We can see that the curve is very close to a straight line with a slope of 1. This linear proportional relationship further demonstrates that the beam amplitude overlap is the crucial factor to determine the grain noise spatial correlation in the focal zone.



### 3.3 HOW DO THE TRANSDUCER FOCAL PARAMETERS AFFECT GRAIN NOISE SPATIAL CORRELATION?

To answer this question, we select two 10 MHz transducers with quite different focal parameters (probe #1, deep-focused and big aperture,  $D = 1.0''$ ,  $GFL = 10''$ ; probe #2, shallow-focused and small aperture,  $D = 0.5''$ ,  $GFL = 3.5''$ ). The specimen is the same 2''-thick waspalloy specimen and we worked on the site with average grain diameter of 47 $\mu$ m. Different water paths are chosen to focus the two transducers at the same depth in metal (0.82'' below the front surface). The time gate is centered at the focal zone.

The measured and predicted noise spatial correlations are plot in Figure 9(a-b). 9(a) is for probe #1 and 9(b) is for probe #2. In both cases, the agreements between the prediction and measurement are excellent. The *SCL* of the grain noise signals acquired by the shallow-focused transducer is about 2/3 of that of the deep-focused probe. The beam profiles (amplitude square and phase at the transducer central frequency) along the time gate central line are plotted in 9(c-d). Comparing 9(c) and 9(d), we can see that, because of the different transducer focal parameters, both the amplitude and phase for probe #2 change more rapidly than those of probe #1. Consequently, the *SCL* of the grain noise signal acquired probe #2 is smaller.

### 3.4 HOW DOES THE GRAIN SIZE AFFECT THE GRAIN NOISE SPATIAL CORRELATION?

We measured the backscattered grain noise signals from another site of the same waspalloy specimen, where the average grain diameter is 97 $\mu$ m. We used the same transducer as used in section 3.1 to collect the noise signals. The beam is focused 1.75'' below the front surface and the 1 us time gate is centered at the focal zone. The measured

and predicted grain spatial correlations for the 97  $\mu\text{m}$  case are plotted in Figure 10 (a) and the 47  $\mu\text{m}$  is shown in Figure 10 (b).

Again, the theory and experiments agree very well. The *SCLs* of the grain noise signals acquired at sites with different grain sizes are slightly different, but the overall trend of the spatial correlations are primarily controlled by beam pattern overlap. Grain size does not matter much as long as the approximation leading the simplification of Eq. (13) is appropriate.

#### 4. DISCUSSION

In section 3, we demonstrate that the developed theory is capable of predicting the spatial correlation of backscattered grain noise for different experimental scenarios. We also qualitatively illustrated that how the beam overlap can influence the predicted grain noise spatial correlation by showing the amplitude and phase profiles (at the central frequency) along the center line of the time gate of interest. In this section, a series of simulation were carried out to quantitatively show the individual contribution by the amplitude and phase overlaps.

We use the same specimen and transducer parameters as used in section 3.1. The transducer is assumed to behave as an ideal piston transducer and can be represented by multi-Gaussian beam model. The hypothetical transducer has 10 MHz central frequency and 6 MHz bandwidth. The reference signal is the response of the back-wall of a 2"-thick FQ block when we focused the beam on the back-wall. As illustrated in Figure 11, we focused the beam at 1" below the specimen front surface. Five time gates (1 $\mu\text{s}$  width) are selected symmetrically located around the focal plane (the 3<sup>rd</sup> time gate). For each time gate, we did the following calculations according to Eq. (16): (1). grain noise spatial correlation contributed only by the amplitude overlap, i.e. only the amplitude values in  $\int_{-\infty}^{\infty} d^3\vec{r} \left[ p^2(\vec{r} - \vec{x}_1) p^{*2}(\vec{r} - \vec{x}_2) \right]$  are used in the calculation; (2). grain noise spatial correlation contributed by the overall beam overlap (both amplitude and phase). The contribution by the

phase overlap can be regarded as the ratio of the results obtained in (2) and those obtained in (1).

The calculated noise spatial correlations are summarized in Figure 12 (a-c). Figure 12 (a) is the results of the overall beam overlap contribution. Figure 12 (b) is the results of only the amplitude overlap. The deduced phase overlap contribution is plotted in Figure 12(c). The *SCL* for each time gate is extracted from the matching curve. For some curves, for example the 4<sup>th</sup> and 5<sup>th</sup> time gates in Figure 12 (b) and (c), the calculated transducer interval is not long enough to deduce the *SCL* directly. For these curves, we first fit each of them into a quadratic form and then extract the *SCL* from the fitted curve. The resulting “*SCLs* - vs.-depth in metal” curves are plotted in Figure 12 (d). The overall beam overlap curve plotted in Figure 12 (d) indicates that the grain noise *SCL* increases with the depth in metal increases, and it reaches its maximum around the focal plane (the 3<sup>rd</sup> time gate). We also note that the rate of change below the focal zone is smaller than that above the focal zone. This is sensible because both the phase and amplitude vary more slowly below the focal zone. In the focal plane, the grain noise *SCL* contributed by the amplitude overlap is almost the same as that contributed by the overall beam overlap, while the *SCL* contributed by the phase overlap is much larger. This result confirmed that the amplitude overlap is the dominating factor in the focal zone. At the depths far away from focal zone, for example the 1<sup>st</sup> and 5<sup>th</sup> time gate, the phase overlap is the dominating factor.

## 5. SUMMARY

In this paper, we extended the existing backscattered grain noise theory to study the grain noise spatial correlation, leading to a formal theory which is capable of predicting the grain noise spatial correlations for different experimental scenarios. The theory was derived in its general form and also presented in a special form for a Gaussian beam. The theory indicates, under appropriate approximation, the material microstructure and the overlap of the incident

sound field (both the amplitude and phase profiles) are the important controlling physical parameters for the spatial correlation of the backscattered grain noise.

According to the theory, a numerical tool is developed to evaluate the grain noise spatial correlations for different circumstances. The grain noise signals are collected from a waspalloy specimen at several experimental setups. The developed theory is validated by the excellent agreements between the predictions and experiments. Physical insights of the results for different setups were discussed.

## ACKNOWLEDGEMENTS

This material is based upon work supported by the Federal Aviation Administration under Contract #DTFA03-98-D-00008, and performed at Iowa State University's Center for NDE as part of the Engine Titanium Consortium program, through the Airworthiness Assurance Center of Excellence.

## REFERENCES

1. J. H. Rose, "Ultrasonic backscattering from polycrystalline aggregates using time-domain linear theory", in *Review of Progress in Quantitative NDE*, Vol. 10B, eds. D.O. Thompson and D.E. Chimenti (Plenum, New York, 1991) p. 1715-1720.
2. J. H. Rose, "Ultrasonic backscatter from microstructure", in *Review of Progress in Quantitative NDE*, Vol. 11B, eds. D.O. Thompson and D.E. Chimenti (Plenum, New York, 1992) p. 1677-1684.
3. J. H. Rose, "Theory of ultrasonic backscatter from multiphase polycrystalline solid", in *Review of Progress in Quantitative NDE*, Vol. 12B, eds. D.O. Thompson and D.E. Chimenti (Plenum, New York, 1993) p. 1719-1726.
4. F. J. Margetan, T. A. Gray, and R. B. Thompson, "A techniques for quantitatively measuring microstructure induced ultrasonic noise" in *Review of Progress in Quantitative NDE*, Vol. 10B, eds. D.O. Thompson and D.E. Chimenti (Plenum, New York, 1991) p. 1721-1728.

5. F. J. Margetan, Thompson, R. B., and Yalda-Mooshabad, I., "Backscattered microstructural noise in ultrasonic tone-burst measurements", in *Journal of Nondestructive Evaluation*, Vol. 13, pp. 111-136, 1994.
6. F. J. Margetan, R. B. Thompson and I. Yalda-Mooshabad, "Modeling ultrasonic microstructural noise in titanium alloy", in *Review of Progress in Quantitative NDE*, Vol. 12B, eds. D.O. Thompson and D.E. Chimenti (Plenum, New York, 1991) p. 1735-1742.
7. F. J. Margetan and R. B. Thompson, "Microstructural noise in titanium alloys and its influence on the detectability of hard-alpha inclusion", in *Review of Progress in Quantitative NDE*, Vol. 11B, eds. D.O. Thompson and D.E. Chimenti (Plenum, New York, 1992) p. 1717-1724.
8. F. J. Margetan, Kim Y. Han, I. Yalda, Scot Goettsch and R.B Thompson, "The practical application of grain noise models in titanium billet and forgings", in *Review of Progress in QNDE*, Vol. 14B, eds. D.O. Thompson and D.E. Chimenti (Plenum, New York, 1995) p. 2129.
9. Thompson, R. B., Margetan, F. J., Rose, J. H., and Han, K. Y., "Influence of microstructure on ultrasonic backscattering noise in titanium alloys," in *Nondestructive Testing and Evaluation*, Vol. 8-9, pp. 485-496, 1992.
10. Yalda-Mooshabad, I. and R. B. Thompson, "Influence of texture and grain morphology on the two-point correlation of elastic constants: theory and implication on ultrasonic attenuation and backscattering", in *Review of Progress in QNDE*, Vol. 14B, eds. D.O. Thompson and D.E. Chimenti (Plenum, New York, 1996) p.1939.
11. Yalda-Mooshabad, I., Thompson, R. B., and Margetan, F., "Predicting ultrasonic grain noise in polycrystals: a Monte Carlo model", in *J. Acoust. Soc. Am.*, Vol. 99, pp. 3445-3455, 1996.
12. Han, Y. K. and Thompson, R. B., "Ultrasonic backscattering in duplex microstructures: Theory and application to titanium alloys", in *Metallurgical Transactions*, Vol. 28A, pp. 91-104 (1997).
13. Han, Y. K., Ph.D. Thesis, Iowa State University, Ames, IA, 1994.
14. F. J. Margetan, P. Haldipur, Linxiao Yu, R. B. Thompson, A. Degtyar, and H. Wasan, "Backscattered ultrasonic noise measurements in jet-engine nickel alloys", in *Review of Progress*

- in *QNDE*, Vol. 20B, eds. D.O. Thompson and D.E. Chimenti (Plenum, New York, 2001), p. 1314-1321.
15. Paul Panetta, "Backscattering and attenuation during the propagation of ultrasonic waves in duplex titanium alloys", Ph.D. thesis, Iowa State University, Ames, IA, 1999.
  16. Yanming Guo, "Effects of material microstructure and surface geometry on ultrasonic scattering and flaw detection", Ph.D. thesis, Iowa State University, Ames, IA, 2003.
  17. Linxiao Yu, F. J. Margetan, R. B. Thompson, and Andrei Degtyar, "Survey of ultrasonic properties of aircraft engine titanium forgings", in *Review of Progress in QNDE*, Vol. 21B, eds. D.O. Thompson and D.E. Chimenti (Plenum, New York, 2002), p. 1510-1517.
  18. Linxiao Yu, R.B. Thompson, Frank J. Margetan and Andrei Degtyar, "Modeling ultrasonic grain noise within Ti-6Al-4V forgings", in *Review of Progress in QNDE*, Vol.22B, eds. D.O. Thompson and D.E. Chimenti (Plenum, New York, 2003), p.1339-1346.
  19. Anxiang Li, Ron Roberts, Pranaam Haldipur, Frank J. Margetan, and R. B. Thompson, "Computational study of grain scattering effects in ultrasonic measurements", in *Review of Progress in QNDE*, Vol. 22B, eds. D.O. Thompson and D.E. Chimenti (Plenum, New York, 2003), p.117-124.
  20. G. Ghoshal and J.A. Turner, "Numerical model of ultrasonic backscatter response in polycrystals", Presented in the conference of *Review of Progress in QNDE*, Golden, Colorado 2004.
  21. P. Haldipur, F. J. Margetan, R. B. Thompson, "Looking for multiple scattering effects in backscattered ultrasonic grain noise from jet-engine nickel alloys", Presented in the conference of *Review of Progress in QNDE*, Golden, Colorado 2004.
  22. N. S. Neidell and M. Turhan Taner, "Semblance and other coherency measures for multichannel data", in *Geophysics*, Vol. 36, No. 3 (June 1971), P482-497.

23. Aleksandar Dogandzic and Nawanat Eua-Anant, "Defect detection in correlated noise", in *Review of Progress in QNDE*, Vol. 23A, eds. D.O. Thompson and D.E. Chimenti (Plenum, New York, 2004). P.628-635.
24. Walker F. William, "Significance of correlation in ultrasonic signal processing", in *Proc. SPIE Vol. 4325, Medical Imaging 2001: Ultrasonic Imaging and Signal Processing*, eds. Michael F. Insana; K. Kirk Shung. P159-171.
25. F. J. Margetan, E. Nieters, L. Brasche, L. Yu, A. Degtyar, H. Wasan, M. Keller and A. Kinney, "Fundamental studies of titanium forging materials - engine titanium consortium II", FAA Technical Center, Atlantic City, N. J., (2004, in review).
26. A. Minachi, F. J. Margetan, R.B. Thompson, "Reconstruction of a piston transducer beam using muti-Gaussian beam (MGB) and its application", in *Review of Progress in QNDE*, eds. D.O. Thompson and D.E. Chimenti, Vol.17 (1998), p. 907.
27. R. B. Thompson and T. A. Gray, "A model relating ultrasonic scattering measurements through liquid-solid interfaces to unbounded medium scattering amplitudes", in *J. Acoust. Soc. Am.*, Vol. 74, pp. 1279 - 1290, 1983.
28. R. B. Thompson and E. F. Lopes, "The effects of focusing and reflection on Gaussian ultrasonic beams", in *Journal of Nondestructive Evaluation*, Vol. 4, pp. 107-123, 1984.
29. Linxiao Yu, F. J. Margetan and R. B. Thompson, Unpublished experimental results of the grain noise correlation in titanium alloy forging materials, performed at the Center for NDE at Iowa State University, Ames, Iowa.
30. D. K. Hsu, D. O. Thompson and R. B. Thompson, "Evaluation of porosity in aluminum alloy casting by single-sided access ultrasonic backscatter", in *Review of Progress in QNDE*, eds. D.O. Thompson and D.E. Chimenti, Vol.5B (1986), p. 1633.
31. Subroutines used to calculate the *SCC* of the measured grain noise were developed by Dr. F. J. Margetan at the Center for NDE at Iowa State University, Ames, Iowa.

32. Subroutines used to calculate the beam profiles were developed by Dr. F. J. Margetan at the Center for NDE at Iowa State University, Ames, Iowa.
33. H. T. O'Neil, "Theory of focusing radiators", in *J. Acoust. Soc. Am.*, Vol. 21, p516–526 (1949).
34. R.B. Thompson, Frank J. Margetan, "Use of elastodynamic theories in the stochastic description of the effect of microstructure on ultrasonic flaw and noise signals", in *Wave motion*, 36 (2002) p.347-365.
35. Linxiao Yu, PhD thesis, "Understanding and improving ultrasonic inspection of jet-engine titanium alloy", Iowa State University, Ames, Iowa. 2004.



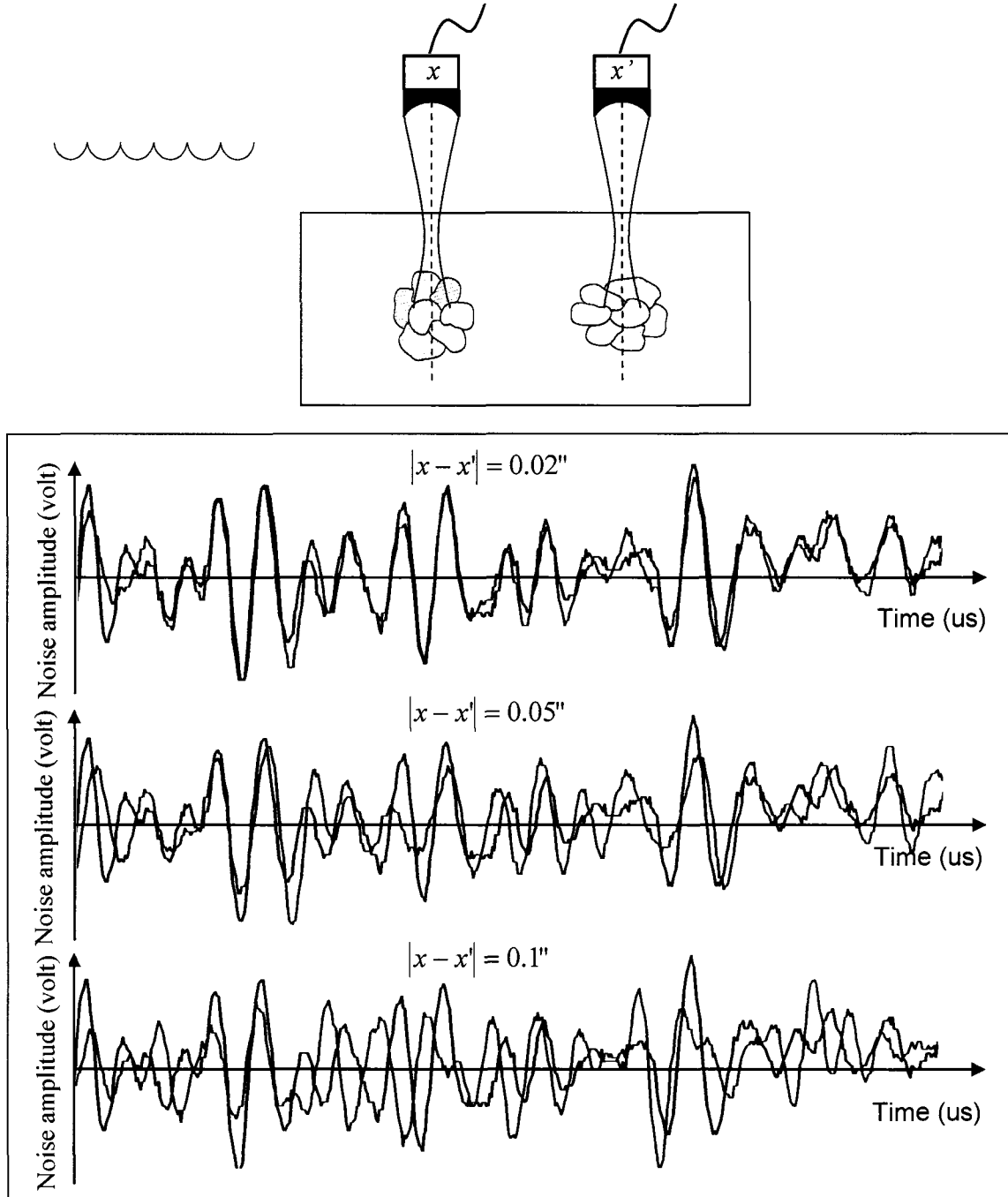


**FIGURE 1.** Grain noise signal acquisition set up (upper panel) and correlated noise waveforms at different transducer locations (bottom panel). For the first grain noise waveform pair,  $|x - x'| = 0.02''$ ,  $SCC = 0.94$ ; when  $|x - x'| = 0.05''$ ,  $SCC = 0.73$ ; when  $|x - x'| = 0.1''$ ,  $SCC = 0.43$ .

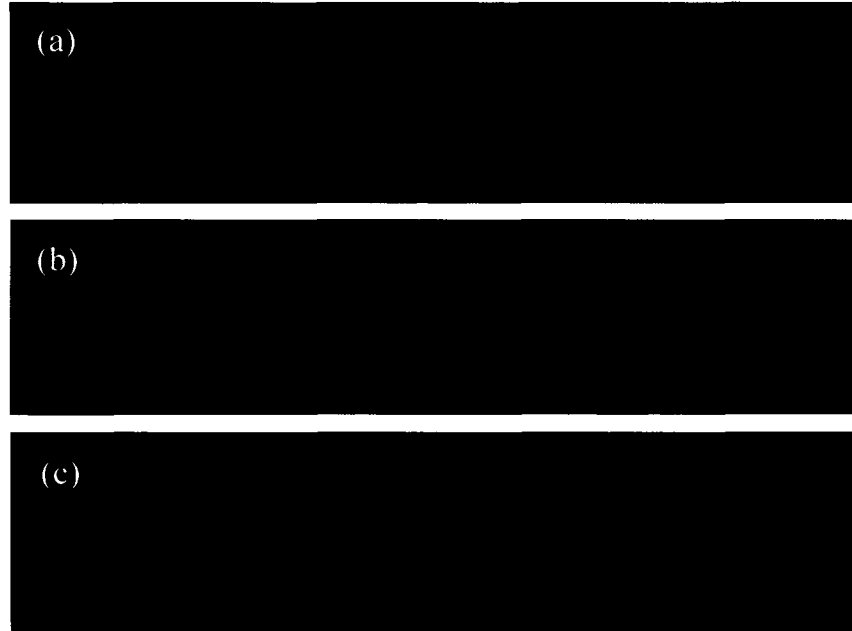


**FIGURE 2.** Experimental and simulated gated-peak noise in a titanium alloy specimen with varying microstructure from one end to the other. (a) Measured GPN; (b) Simulated GPN, SCL = 0.045"; (c) Simulated GPN, SCL = 0.015".

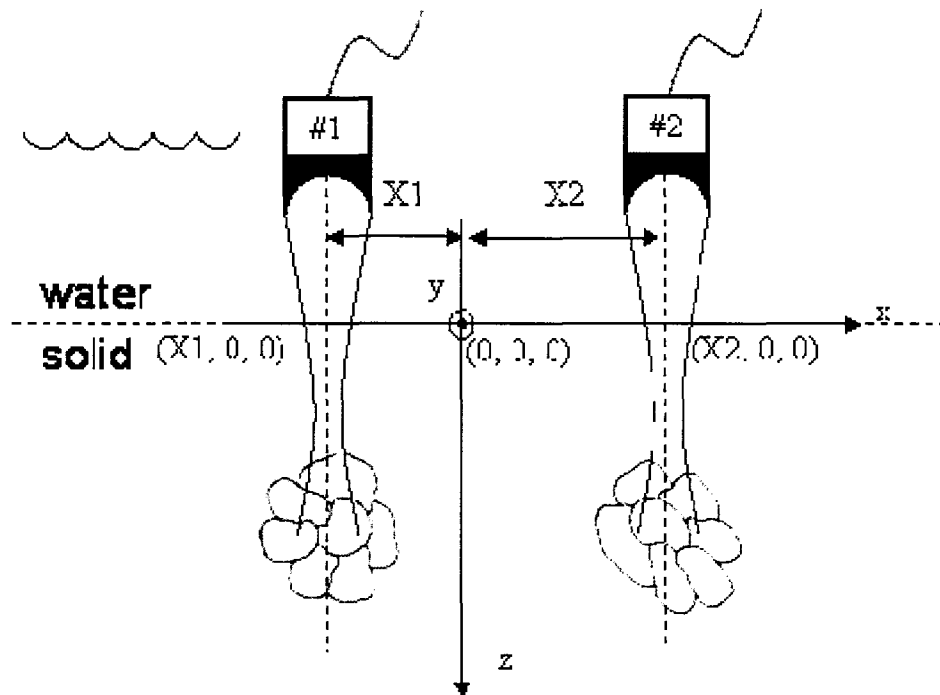


**FIGURE 3.** Coordinate system used to derive the theory. Transducer #1, central ray locates at  $(x_1, 0, 0)$ ; Transducer #2, central ray locates at  $(x_2, 0, 0)$ .

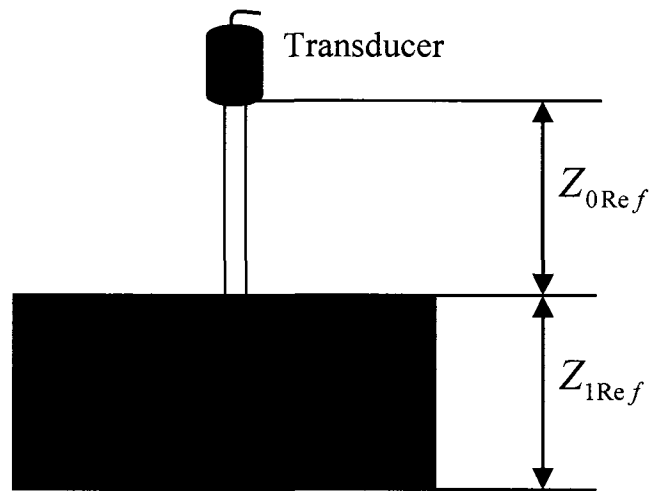


**FIGURE 4.** Introducing a reference signal to extract the system and transducer efficiency.

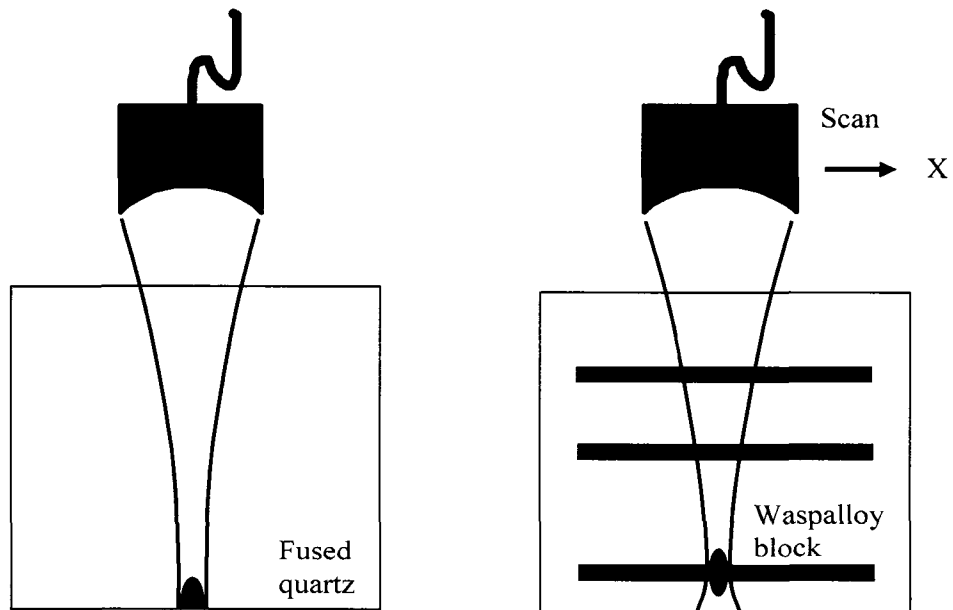


**FIGURE 5.** Experimental set ups for acquiring the reference signal (FQ back wall signal) and backscattered grain noise signals from a waspalloy specimen. The horizontal color bars in the right graph indicate the corresponding depths (time gates), from where the spatial correlations of the measured grain noise signals are evaluated.

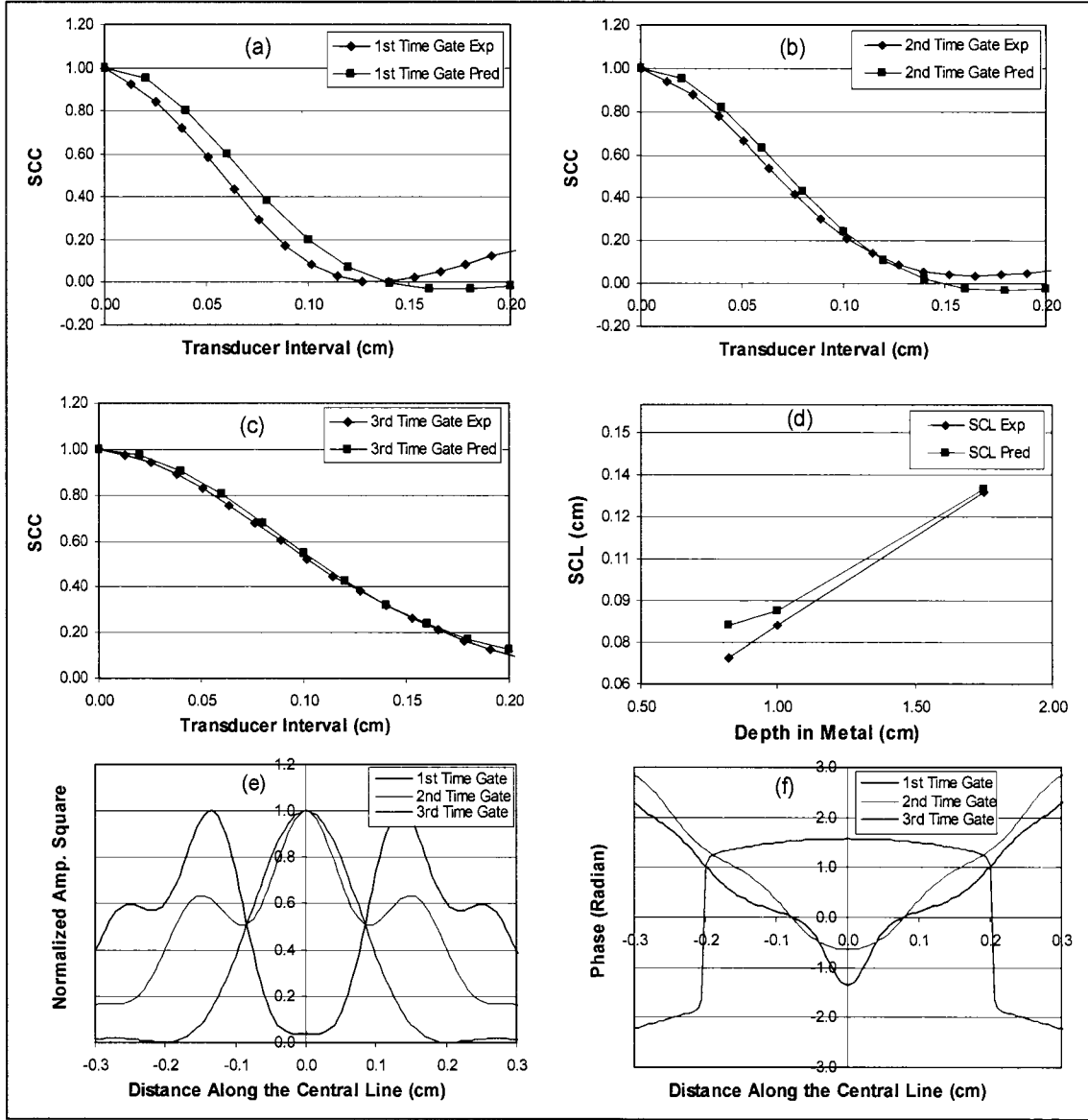


**FIGURE 6.** Comparisons between theoretical and experimental grain noise spatial correlations. (a) 1st time gate; (b) 2nd time gate, half depth of the specimen; (c) 3rd time gate, focal zone; (d) Experimental and predicted *SCLs* for the 3 time gates; (e) The profiles of the amplitude square along the central line of the interested time gate; (f) The phase profiles along the central line of the interested time gate.

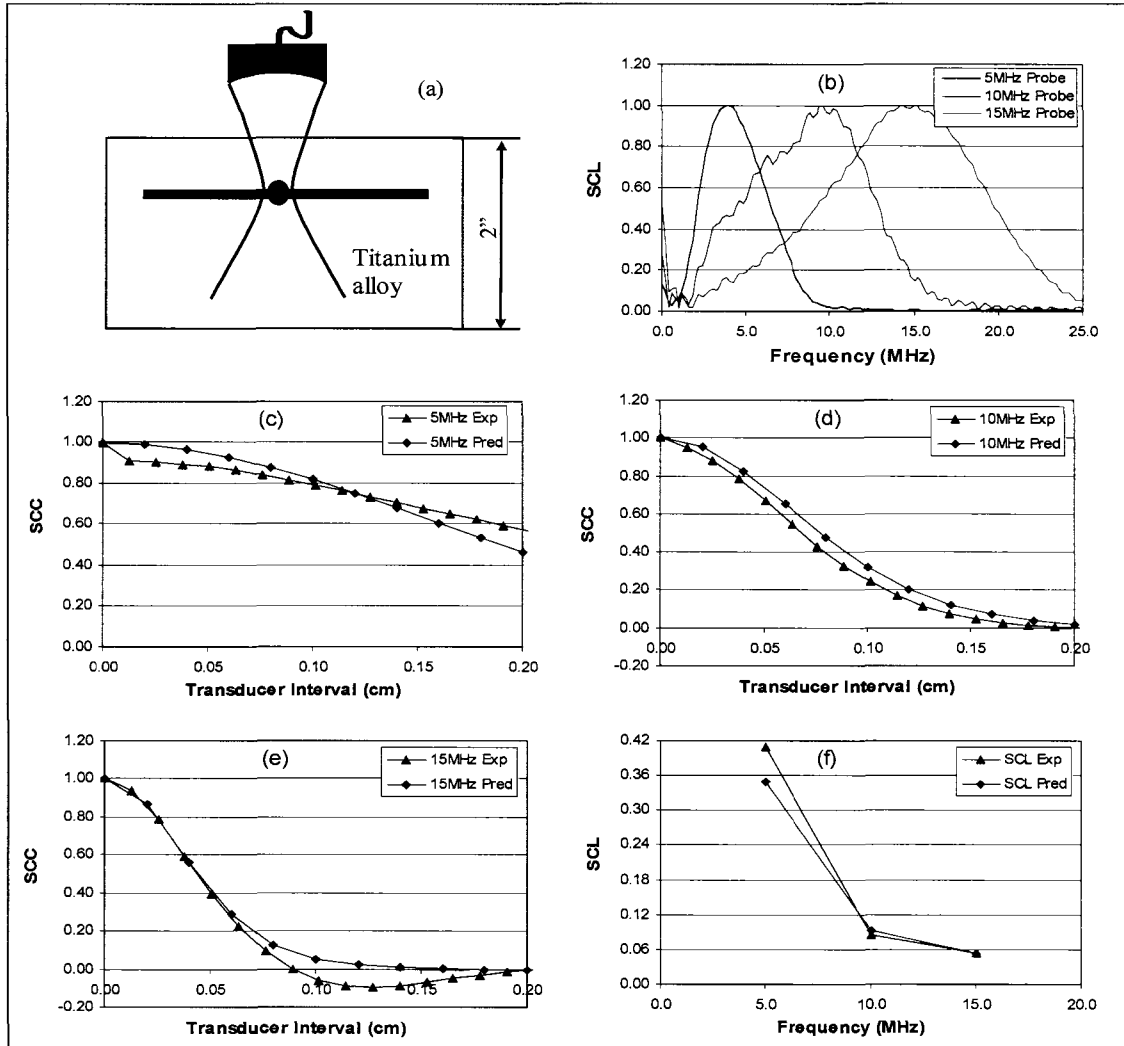


**FIGURE 7.** The transducer central frequency effects on the grain noise spatial correlation. (a) Experiment setup; (b) The spectra of the 3 transducers; (c-e) The experimental and predicted grain noise spatial correlations using the 3 transducers; (f) The experimental and predicted grain noise spatial correlation lengths using the 3 transducers; (g) The profiles of the amplitude square along the central line of the interested time gate; (h) The phase profiles along the central line of the interested time gate.

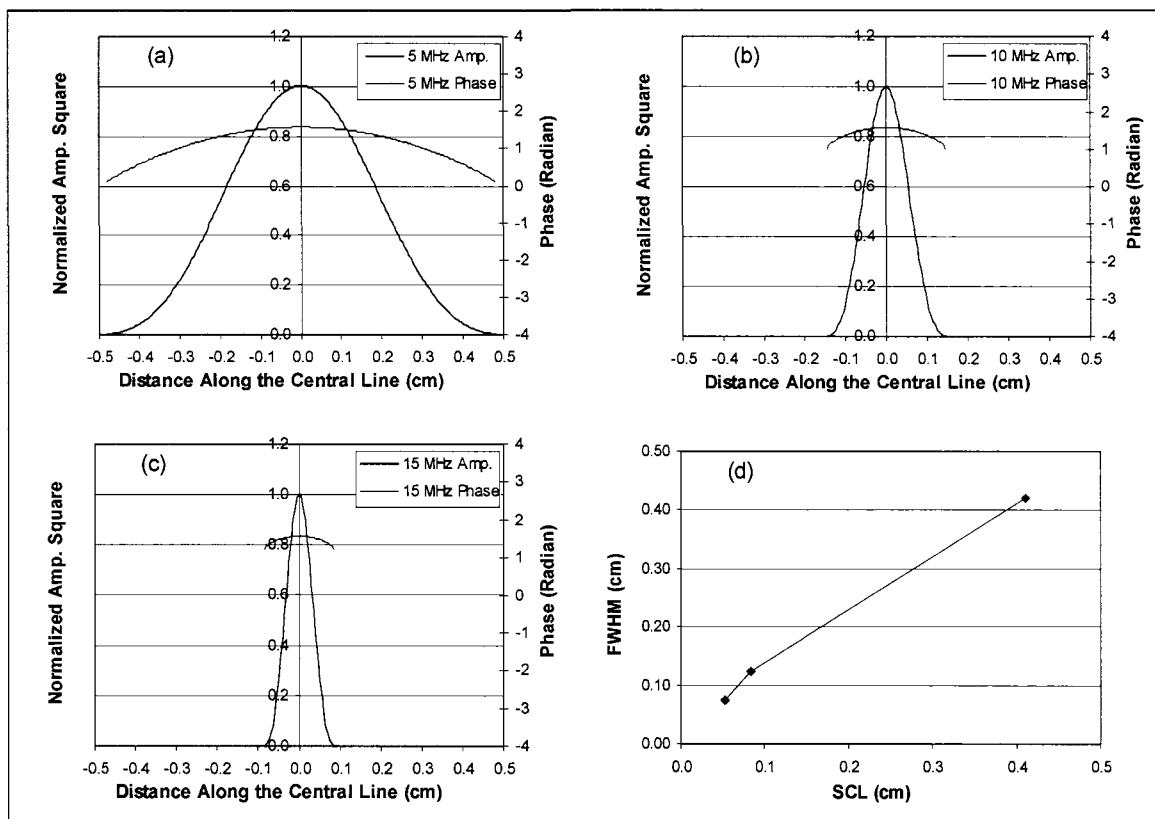


**FIGURE 8.** The beam profiles for 3 transducers. (a) The amplitude and phase profiles for the 5 MHz transducer; (b) The amplitude and phase profiles for the 10 MHz transducer; (c) The amplitude and phase profiles for the 15 MHz transducer; (d) The measured noise SCLs using the 3 transducers and FWHMs of the corresponding amplitude profiles.

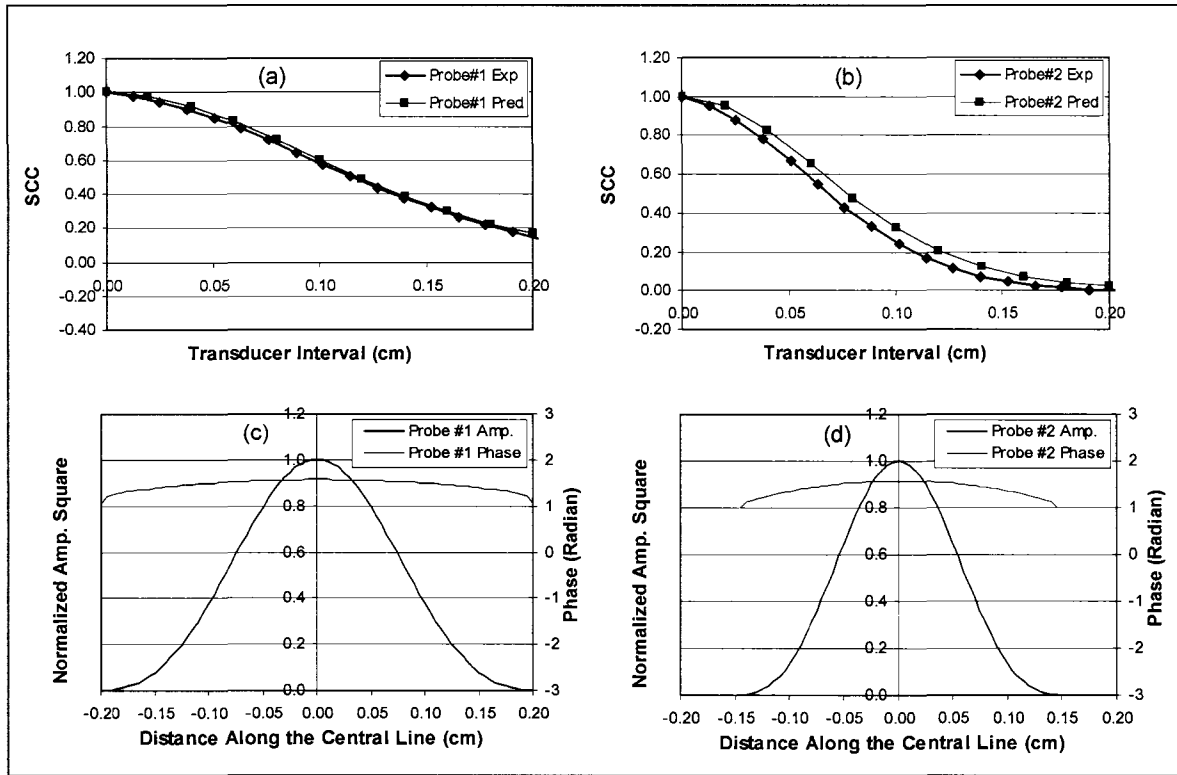


**FIGURE 9.** The transducer focal parameters effects on the grain noise spatial correlation. (a) The experimental and predicted grain noise spatial correlations for probe #1; (b) The experimental and predicted grain noise spatial correlations for probe #2; (c) The profiles of the amplitude square and phase for probe #1; (d) The profiles of the amplitude square and phase for probe #2.

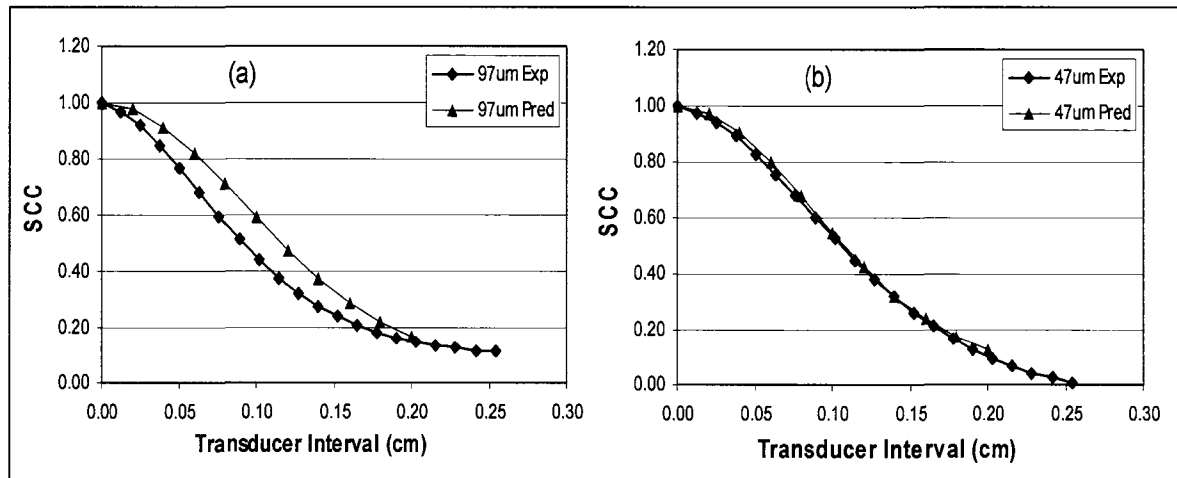


**FIGURE 10.** The grain size effects on the grain noise spatial correlations. (a) Simulation setups; (b) The predicted grain noise spatial correlations at 3 different grain sizes.

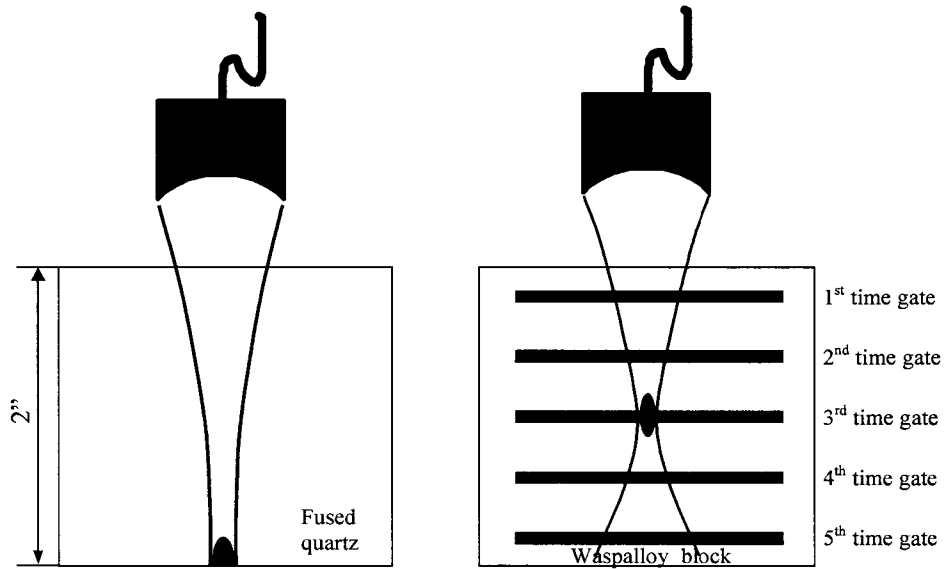


**FIGURE 11.** The simulation setups. Reference block: 2"-thick FQ, the beam is focused on back-wall; specimen: 2"-thick waspalloy, the beam is focused at 1" below the front surface.

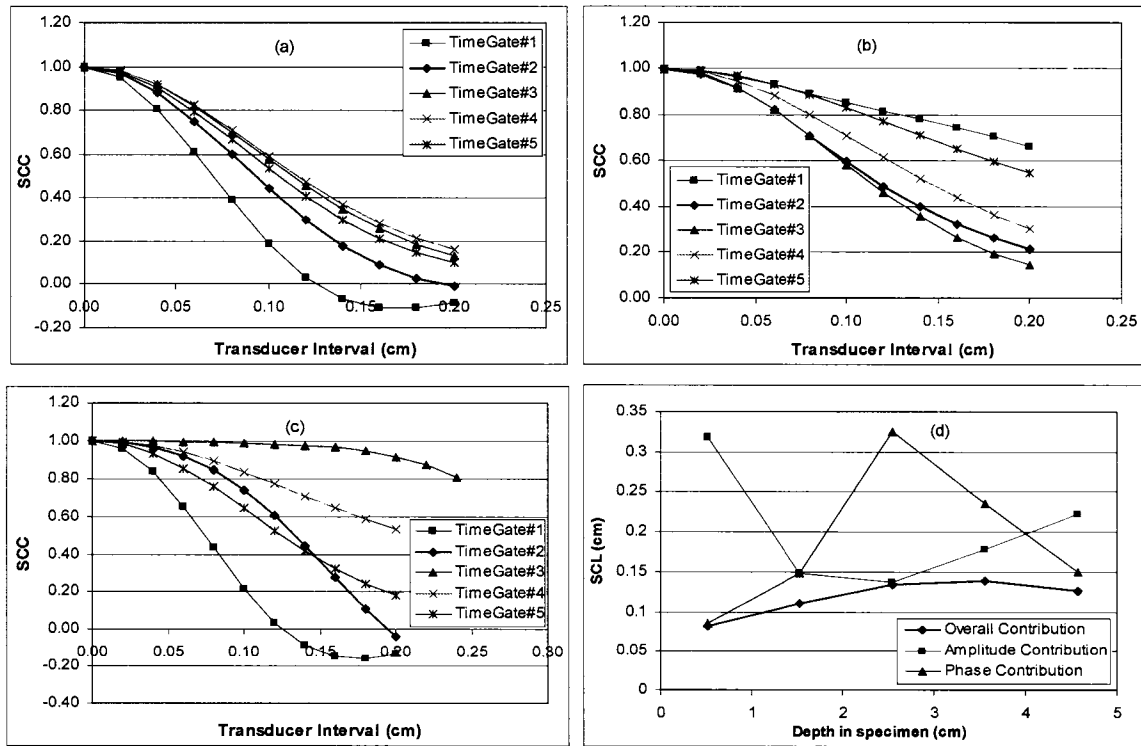


**FIGURE 12.** The calculated grain noise spatial correlations contributed: (a) the overall beam overlap; (b) the amplitude overlap only; (c) the phase overlap only. (d) The deduced SCLs from (a-c).



## APPENDIX: THEORY FOR BACKSCATTERED ULTRASONIC GRAIN NOISE

### SPATIAL CORRELATION

The section 2 of this chapter outlined the derivation of the theory for the backscattered grain noise spatial correlation. A detailed version is given below. To make this appendix self-contained, some figures and equations in the section 2 were repeated.

The coordinate system used to derive the theory is shown in Figure A1. The grain noise signals from a metal specimen are collected using an immersion UT system. When the transducer central ray is aligned with the  $Z$ -axis, the transducer response  $\delta\Gamma$  at frequency  $f$  due to the presence of grain scatterer within a volume  $\Omega$  can be written as Eq. (A1) [1-5]:

$$\delta\Gamma(f) = \frac{j\omega}{4P(\omega)} \int_{\Omega} d^3\vec{r} \left[ \omega^2 \delta\rho(\vec{r}) u_{1i}(\vec{r}) u_{2i}(\vec{r}) - \delta C_{ijkl}(\vec{r}) u_{1i,j}(\vec{r}) u_{2k,l}(\vec{r}) \right] \quad (\text{A1})$$

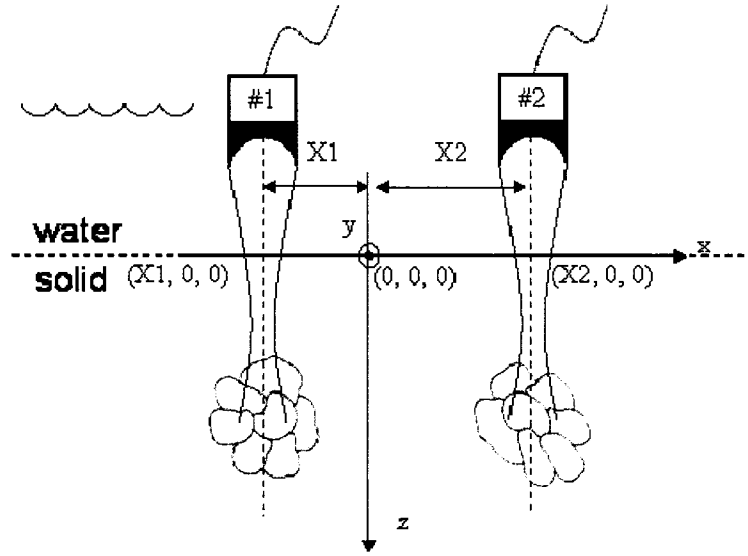


**FIGURE A1.** Coordinate system used to derive the theory. Transducer #1, central ray locates at  $(x1, 0, 0)$ ; Transducer #2, central ray locates at  $(x2, 0, 0)$ .

Here  $\omega$  is the angular frequency.  $P(\omega)$  is the exciting electrical power from the pulser.  $\delta\rho(\vec{r})$  and  $\delta C_{ijkl}(\vec{r})$ , as defined as in Eq. (A2) and Eq. (A3), are the variations of the density and elastic constant at the specified point  $\vec{r}$  from the homogeneous medium.  $C_{ijkl}(\vec{r})$  and  $\rho(\vec{r})$  are the spatially varying elastic constant tensor and density of the inhomogeneous medium at the location  $\vec{r}$ .  $C_{ijkl}^v$  and  $\rho^v$  are the counterparts of  $C_{ijkl}(\vec{r})$  and  $\rho(\vec{r})$  for the homogeneous medium.  $u_{1i}(\vec{r})$  and  $u_{2i}(\vec{r})$  are wave displacements that would exist at the location  $\vec{r}$  with (total) and without (incident) the inhomogeneities.  $u_{1i,j}(\vec{r})$  and  $u_{2k,l}(\vec{r})$  is the spatial derivatives of  $u_{1i}(\vec{r})$  and  $u_{2i}(\vec{r})$ . Note that the summation of convention is assumed for repeated subscript indices.

$$\delta\rho(\vec{r}) \equiv \rho(\vec{r}) - \rho^v \quad (\text{A2})$$

$$\delta C_{ijkl}(\vec{r}) \equiv C_{ijkl}(\vec{r}) - C_{ijkl}^v \quad (\text{A3})$$

$$u_{1i}(\vec{r}) = u_{2i}(\vec{r}) \quad (\text{A4})$$

In the “Born” approximation, stated in Eq. (A4), one assumes that the total field (incident field plus scattered field) equal to the incident field. If one makes the additional assumption that the density variations throughout the interested volume  $\Omega$  are negligible, Eq. (A1) can be simplified as Eq. (A5):

$$\delta\Gamma(f) = \frac{-j\omega}{4P(\omega)} \int_{\Omega} d^3\vec{r} \left[ \delta C_{ijkl}(\vec{r}) \varepsilon(\vec{r})^2 \right] \quad (\text{A5})$$

where,  $\varepsilon(\vec{r})$  is the elastic strain at the location  $\vec{r}$ .

As illustrated in Figure A1, backscattered grain noise signals,  $\delta\Gamma(t, \vec{x1})$  and  $\delta\Gamma(t, \vec{x2})$ , the Fourier transformations of  $\delta\Gamma(f, \vec{x1})$  and  $\delta\Gamma(f, \vec{x2})$  respectively, are acquired at two

transducer positions  $(x1, 0, 0)$  and  $(x2, 0, 0)$ . The spatial correlation between the grain noise signals is defined as in Eq. (A6):

$$\begin{aligned} C(\vec{x1}, \vec{x2}) &= \left\langle \int \delta\Gamma(t, \vec{x1}) \delta\Gamma(t, \vec{x2}) dt \right\rangle \\ &= \left\langle \int dt \int_{-\infty}^{\infty} df \int_{-\infty}^{\infty} df' \left[ \delta\Gamma(f, \vec{x1}) \delta\Gamma(f', \vec{x2}) e^{j2\pi t(f+f')} \right] \right\rangle \end{aligned} \quad (A6)$$

Changing variable  $f' = -f''$ , and using the reality property of the grain noise signal i.e.  $\delta\Gamma(-f'', \vec{x2}) = \delta\Gamma^*(f'', \vec{x2})$ , we can rewrite Eq. (A6) as:

$$\begin{aligned} C(\vec{x1}, \vec{x2}) &= \left\langle \int_{-\infty}^{\infty} df \int_{-\infty}^{\infty} df'' \left[ \delta\Gamma(f, \vec{x1}) \delta\Gamma^*(f'', \vec{x2}) \right] \delta(f - f'') \right\rangle \\ &= \left\langle \int_{-\infty}^{\infty} df \left[ \delta\Gamma(f, \vec{x1}) \delta\Gamma^*(f, \vec{x2}) \right] \right\rangle \end{aligned} \quad (A7)$$

The “ $\langle \dots \rangle$ ” notation represents spatial ensemble average and the superscript “ $*$ ” represents complex conjugate. Put Eq. (A5) into Eq. (A7), we can find:

$$\begin{aligned} C(\vec{x1}, \vec{x2}) &= \left\langle \int_{-\infty}^{\infty} df \left\{ \left[ \frac{\omega^2}{16P(\omega)P(\omega)^*} \right] \right. \right. \\ &\quad \left. \left. \int_{-\infty}^{\infty} d^3\vec{r1} \left[ \delta C_{ijkl}(\vec{r1}) \varepsilon_0^2(\vec{r1} - \vec{x1}) \right] \int_{-\infty}^{\infty} d^3\vec{r2} \left[ \delta C_{ijkl}(\vec{r2}) \varepsilon_0^{*2}(\vec{r2} - \vec{x2}) \right] \right\} \right\rangle \end{aligned} \quad (A8)$$

Note that, the  $\vec{\varepsilon}(\vec{r})$  term in Eq. (A5) is the general expression, and the  $\varepsilon_0(\vec{r1} - \vec{x1})$  and  $\varepsilon_0(\vec{r2} - \vec{x2})$  are the specific forms for transducer locations  $\vec{x1}$  and  $\vec{x2}$ . Changing the variables as in Eq. (A9) and Eq. (A10) and following the argument that:  $d\vec{r1} d\vec{r2} = d\vec{r} d\vec{s}$  [5], we can rewrite Eq. (A8) as Eq. (A11).

$$\vec{r} = \frac{\vec{r1} + \vec{r2}}{2} \quad (A9)$$

$$\vec{s} = \vec{r2} - \vec{r1} \quad (A10)$$

$$C(\vec{x1}, \vec{x2}) = \left\langle \int_{-\infty}^{\infty} df \left\{ \left[ \frac{\omega^2}{16P(\omega)P(\omega)^*} \right] \int_{-\infty}^{\infty} d^3\vec{r} \left[ \delta C_{ijkl}(\vec{r} - \frac{\vec{s}}{2}) \varepsilon_0^2(\vec{r} - \frac{\vec{s}}{2} - \vec{x1}) \right] \int_{-\infty}^{\infty} d^3\vec{s} \left[ \delta C_{ijkl}(\vec{r} + \frac{\vec{s}}{2}) \varepsilon_0^{*2}(\vec{r} + \frac{\vec{s}}{2} - \vec{x2}) \right] \right\} \right\rangle \quad (A11)$$

When the beam is aligned with the z-axis, the elastic displacement field at location  $(x, y, z)$  in the solid (water path is  $Z_0$ ) can be written in the form of Eq. (A12):

$$u(f, x, y, z) = u_0 T_{01} e^{-jk_0 Z_0} e^{-(\alpha_0 Z_0 + \alpha_1 Z)} p(f, x, y, z) e^{-jk_1 Z} \quad (A12)$$

$u_0$  is the particle displacement at the transducer face.  $T_{01}$  is the plane wave transmission coefficient through the water/solid interface. The  $p(f, \vec{r})$  term accounts for the effect of diffraction and focusing on the beam strength. The plane wave propagation and attenuation are described by  $e^{-jkz}$  and  $e^{-(\alpha_0 Z_0 + \alpha_1 Z)}$ .  $\alpha_0$  and  $\alpha_1$  are the wave attenuation coefficients of water and metal respectively.  $k_0$  and  $k_1$  are the magnitude of wave numbers in water and metal respectively. The corresponding elastic strain can be written as:

$$\varepsilon(f, x, y, z) = \frac{\partial u}{\partial z} = -jk_1 u_0 T_{01} e^{-jk_0 Z_0} e^{-(\alpha_0 Z_0 + \alpha_1 Z)} p(f, x, y, z) e^{-jk_1 Z} \quad (A13)$$

Note that, Eq. (A13) is an approximation. We assume that the primary contribution to the  $\frac{\partial}{\partial z}$  operation is from the phase factor  $e^{-jk_1 Z}$  and neglect the small x- and y- components of the displacement field for the longitudinal beam. Similar arguments can be found in reference [6], in which the author approximated the longitudinal displacement field by differentiating the corresponding velocity potential [7].

$$\begin{aligned}
\varepsilon(f, x, y, z)^2 &= -\frac{\omega^2}{v_1^2} u_0^2 T_{01}^2 e^{-j2k_0 Z_0} e^{-2(\alpha_0 Z_0 + \alpha_1 Z)} p(f, x, y, z)^2 e^{-j2k_1 Z} \\
&= -\frac{V_0^2}{v_1^2} T_{01}^2 e^{-j2k_0 Z_0} e^{-2(\alpha_0 Z_0 + \alpha_1 Z)} p(f, x, y, z)^2 e^{-j2k_1 Z}
\end{aligned} \tag{A14}$$

where  $V_0^2$  is the vibration velocity of the particles on the transducer surface, which is related to the  $P(\omega)$  factor and the transducer efficiency  $\beta(\omega)$  as [7]:

$$\frac{V_0^2}{P(\omega)} = \frac{2\beta(\omega)}{\pi a^2 \rho_0 v_0} \tag{A15}$$

Replace the strain terms in Eq. (A11) with Eq. (A14), one can find that:

$$\begin{aligned}
C(\vec{x1}, \vec{x2}) &= \frac{T_{01}^4}{16v_1^4} \left\langle \int_{-\infty}^{\infty} df \left\{ \left[ \frac{\omega^2 V_0^4 e^{-4\alpha_0 Z_0}}{P(\omega) P(\omega)^*} \right] \right. \right. \\
&\quad \left. \int_{-\infty}^{\infty} d^3 \vec{r} \left[ e^{-4\alpha_1 r_3} \right] \right. \\
&\quad \left. \left. \int_{-\infty}^{\infty} d^3 \vec{s} \left[ \delta C_{ijkl}(\vec{r} - \frac{\vec{s}}{2}) \delta C_{ijkl}(\vec{r} + \frac{\vec{s}}{2}) p^2(\vec{r} - \frac{\vec{s}}{2} - \vec{x1}) p^{*2}(\vec{r} + \frac{\vec{s}}{2} - \vec{x2}) e^{2jk_1 s_3} \right] \right\} \right\rangle
\end{aligned} \tag{A16}$$

With the relationship in Eq. (A15), Eq. (A16) can be written as:

$$\begin{aligned}
C(\vec{x1}, \vec{x2}) &= \frac{T_{01}^4}{4v_1^4 \pi^2 a^4 \rho_0^2 v_0^2} \left\langle \int_{-\infty}^{\infty} df \left\{ \left[ \omega^2 e^{-4\alpha_0 Z_0} |\beta(\omega)|^2 \right] \right. \right. \\
&\quad \left. \int_{-\infty}^{\infty} d^3 \vec{r} \left[ e^{-4\alpha_1 r_3} \right] \right. \\
&\quad \left. \left. \int_{-\infty}^{\infty} d^3 \vec{s} \left[ \delta C_{ijkl}(\vec{r} - \frac{\vec{s}}{2}) \delta C_{ijkl}(\vec{r} + \frac{\vec{s}}{2}) p^2(\vec{r} - \frac{\vec{s}}{2} - \vec{x1}) p^{*2}(\vec{r} + \frac{\vec{s}}{2} - \vec{x2}) e^{2jk_1 s_3} \right] \right\} \right\rangle
\end{aligned} \tag{A17}$$

Eq. (A17) is the exact expression for the backscattered grain noise spatial correlation, within the “Born” approximation. If the material elastic properties vary rapidly with respect to the wave field ( $p(f, \vec{r})$  term),  $C(\vec{x1}, \vec{x2})$  can be further approximated as:

$$\begin{aligned}
C(\vec{x1}, \vec{x2}) = & \frac{T_{01}^4}{4v_1^4 \pi^2 a^4 \rho_0^2 v_0^2} \int_{-\infty}^{\infty} df \left\{ \left[ \omega^2 e^{-4\alpha_0 Z_0} |\beta(\omega)|^2 \right] \right. \\
& \int_{-\infty}^{\infty} d^3 \vec{r} \left[ e^{-4\alpha_1 r_3} \right] \left[ p^2(\vec{r} - \vec{x1}) p^{*2}(\vec{r} - \vec{x2}) \right] \\
& \left. \left\langle \int_{-\infty}^{\infty} d^3 \vec{s} \left[ \delta C_{ijkl}(\vec{r} - \frac{\vec{s}}{2}) \delta C_{ijkl}(\vec{r} + \frac{\vec{s}}{2}) e^{2jk_1 s_3} \right] \right\rangle \right\}
\end{aligned} \tag{A18}$$

Note that, by this approximation, the first order effect of the grain size has been factored out of the integral of  $\int_{-\infty}^{\infty} d^3 \vec{s} [ ]$  in Eq.(A17). The  $\left\langle \int_{-\infty}^{\infty} d^3 \vec{s} \left[ \delta C_{ijkl}(\vec{r} - \frac{\vec{s}}{2}) \delta C_{ijkl}(\vec{r} + \frac{\vec{s}}{2}) e^{2jk_1 s_3} \right] \right\rangle$  term in Eq.(A18) is the spatial Fourier transformation of the two-point correlation of elastic constants, which is directly proportional to the backscattering coefficient  $\eta$ , or the square of *FOM* of the metal specimen. The *FOM* of a particular microstructure can be calculated using the program developed in earlier work [4, 5, 8, 9, 10]. Since  $p(f, \vec{r})$  are beam spread terms, the volume integral of  $p^2(\vec{r} - \vec{x1}) p^{*2}(\vec{r} - \vec{x2})$  that appears as a factor in Eq.(A18) physically means the overlap of the incident ultrasonic beams at the two transducer positions, which can be evaluated using the Multi-Gaussian beam model [11]. Since we do not have explicit expression for the system and transducer efficiency, the grain noise spatial correlation can not be directly computed using Eq. (A18).

To overcome this problem, we follow the calibration procedure proposed in reference [7]. As shown in Figure A2, a fused quartz (FQ) specimen is used as a reference block, and the back-wall signal of the reference block (the incident beam is normal to the sample front surface) is acquired using the same UT measurement system. According to the reference [7], the measured back-wall signal spectrum  $\Gamma_{Ref}(f)$  can be written as:

$$\Gamma_{Ref}(f) = \beta(f) T_{01} T_{10} R_{11} D(Z_{0Ref}, Z_{1Ref}, f) e^{-j[k_0 Z_{0Ref} + k_1 Z_{1Ref}]} e^{-[2\alpha_0 Z_{0Ref}]} \tag{A19}$$

Here  $\beta$  is the system and transducer efficiency. The subscript “Ref” indicates values for the reference experiment. The subscripts “0” and “1” indicate water and solid.  $T_{01}$  and  $T_{10}$  are the

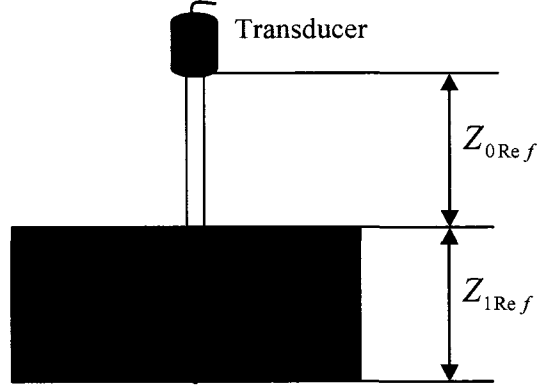


**FIGURE A2.** Introducing a reference signal to extract the system and transducer efficiency.

liquid-solid and solid-liquid interface plane wave transmission coefficients at normal incidence.  $R_{ll}$  is the plane wave reflection coefficient of the back solid-liquid interface at normal incidence. The term  $D(Z_{0Ref}, Z_{1Ref}, f)$  accounts for the effects of diffraction, which can be evaluated by using the Multi-Gaussian beam model [11].  $k_0$  and  $k_1$  are the wave numbers in water and FQ respectively.  $Z_{0Ref}$  and  $Z_{1Ref}$  are the water path and thickness of the FQ. It is assumed that the attenuation of the FQ block is negligible.

Plug Eq. (A19) into Eq. (A18), we can find:

$$C(\vec{x1}, \vec{x2}) = \frac{4 T_{01}^4 v_1^2 \rho_1^2}{a^4 \rho_0^2 v_0^2 (T_{01}^2 T_{10}^2 R_{11}^2)_{Ref}} \int_{-\infty}^{\infty} df \left\{ \frac{[FOM^2 e^{-4\alpha_0 d} |\Gamma_{Ref}(\omega)|^2]}{k_1^2 |D(Z_{0Ref}, Z_{1Ref}, f)|^2} \int_{-\infty}^{\infty} d^3 \vec{r} [e^{-4\alpha_1 r_3}] [p^2(\vec{r} - \vec{x1}) p^{*2}(\vec{r} - \vec{x2})] \right\} \quad (A20)$$

The “ $d$ ” term is the water path difference used when acquiring the grain noise signal and the reference signal,  $d = Z_0 - Z_{0Ref}$ . In practical inspection, we are interested in the correlation of the backscattered ultrasonic grain noise within a very small depth range (along  $z$ -axis). Because the depth range (or the corresponding time gate) of interest is very small (0.12”, or 1us), the effect of specimen attenuation can be approximated by the attenuation at the center of the time gate ( $e^{-4\alpha_1 Z_c}$ ).

The  $\alpha_1$  is the attenuation coefficient of the specimen and  $z_c$  is the depth corresponding to the center of the time gate. The final form of the grain noise spatial correlation is:

$$C(\vec{x1}, \vec{x2}) = \frac{4 T_{01}^4 v_1^2 \rho_1^2}{a^4 \rho_0^2 v_0^2 (T_{01}^2 T_{10}^2 R_{11}^2)_{Ref}} \int_{-\infty}^{\infty} df \left\{ \left[ \frac{|\delta\Gamma_{Ref}(f)|^2 e^{-4\alpha_0 d} e^{-4\alpha_1 z_c} FOM(f)^2}{k^2 |D(Z_{0Ref}, Z_{1Ref}, f)|^2} \right] \int_{-\infty}^{\infty} d^3 \vec{r} \left[ p^2(\vec{r} - \vec{x1}) p^{*2}(\vec{r} - \vec{x2}) \right] \right\} \quad (A21)$$

The coefficient outside the integral in Eq.(A21) is a scaling factor. Since we are interested in the normalized value, this scaling factor is not important.

## REFERENCES

1. J. H. Rose, "Ultrasonic backscattering from polycrystalline aggregates using time-domain linear theory", in *Review of Progress in Quantitative NDE*, Vol. 10B, eds. D.O. Thompson and D.E. Chimenti (Plenum, New York, 1991) p. 1715-1720.
2. J. H. Rose, "Ultrasonic backscatter from microstructure", in *Review of Progress in Quantitative NDE*, Vol. 11B, eds. D.O. Thompson and D.E. Chimenti (Plenum, New York, 1992) p. 1677-1684.
3. J. H. Rose, "Theory of ultrasonic backscatter from multiphase polycrystalline solid", in *Review of Progress in Quantitative NDE*, Vol. 12B, eds. D.O. Thompson and D.E. Chimenti (Plenum, New York, 1993) p. 1719-1726.
4. Han, Y. K. and Thompson, R. B., "Ultrasonic backscattering in duplex microstructures: Theory and application to titanium alloys", in *Metallurgical Transactions*, Vol. 28A, pp. 91-104 (1997).



5. Han, Y. K., "Relationship between the ultrasonic grain noise and microstructure in two-phase microstructures", Ph.D. Thesis, Iowa State University, Ames, IA, 1994.
6. R. B. Thompson and E. F. Lopes, "The effects of focusing and reflection on Gaussian ultrasonic beams", in *Journal of Nondestructive Evaluation*, Vol. 4, pp. 107-123, 1984.
7. R. B. Thompson and T. A. Gray, "A model relating ultrasonic scattering measurements through liquid-solid interfaces to unbounded medium scattering amplitudes", in *J. Acoust. Soc. Am.*, Vol. 74, pp. 1279 - 1290, 1983.
8. Paul Panetta, "Backscattering and attenuation during the propagation of ultrasonic waves in duplex titanium alloys", Ph.D. thesis, Iowa State University, Ames, IA, 1999.
9. Yanming Guo, "Effects of material microstructure and surface geometry on ultrasonic scattering and flaw detection", Ph.D. thesis, Iowa State University, Ames, IA, 2003.
10. Linxiao Yu, R.B. Thompson, Frank J. Margetan and Andrei Degtyar, "Modeling ultrasonic grain noise within Ti-6Al-4V forgings", in *Review of Progress in QNDE*, Vol.22B, eds. D.O. Thompson and D.E. Chimenti (Plenum, New York, 2003), p.1339-1346.
11. A. Minachi, F. J. Margetan, R.B. Thompson, "Reconstruction of a piston transducer beam using muti-Gaussian beam (MGB) and its application", in *Review of Progress in QNDE*, eds. D.O. Thompson and D.E. Chimenti, Vol.17 (1998), p. 907.

## CHAPTER 3. MICROSTRUCTURE-INDUCED ULTRASONIC SIGNAL FLUCTUATIONS IN TITANIUM ALLOY

A paper to be submitted to the Journal of Nondestructive Evaluation

Linxiao Yu, R. B. Thompson, F. J. Margetan and Yurong Wang

Center for Nondestructive Evaluation

Iowa State University

Ames, IA 50011

**ABSTRACT.** In ultrasonic inspections of some jet-engine alloys, microstructural inhomogeneities act to significantly distort the amplitude and phase profiles of the incident sonic beam, and these distortions lead in turn to ultrasonic signal variations. For example, in pulse/echo (P/E) inspections, the nominally-identical standard defects, such as arrays of flat-bottom-holes (FBH) located at a given depth, have quite different responses. Similarly, the back-wall signal amplitude is often seen to fluctuate dramatically when scanning a transducer parallel to a flat specimen. The stochastic nature of the ultrasonic response has important implications in practical NDT/E, and tools to estimate fluctuation levels are needed. In this study, we first explicitly demonstrate various beam distortions induced by the microstructure, i.e., two types of amplitude distortion: the lateral “drift” of the center-of-energy about its expected position; the distortion of pressure amplitude about its expected pattern; and two types of wave-front distortion (“wrinkling” and “tilting”). An analytical relationship is then derived to correlate the back-wall P/E spectrum at one transducer location to the through-transmitted field. Based on the analytical relationship, a quantitative Monte-Carlo model is developed to predict the back-wall amplitude fluctuations seen in ultrasonic P/E inspections. Our modeling approach is demonstrated using rectangular coupons of jet-engine Titanium alloys, and predicted back-wall fluctuation levels at 3 frequencies for both planar and focused transducer are shown to be in good agreements with experiments. In the last section of this paper, the same modeling approach is used to simulate flaw signal fluctuation. The predicted fluctuation levels are compared with that obtained

from the simulated data. Qualitative agreements are observed. As a novel way of modeling ultrasonic signal fluctuations, the approach outlined in this paper suggests many possibilities for future research.

## 1. INTRODUCTION

In ultrasonic inspections of some jet-engine alloys, microstructural inhomogeneities act to significantly distort the amplitude and phase profiles of the incident sonic beam. As reported in earlier work [1-3], these distortions can lead to large ultrasonic signal fluctuations in some circumstances. As a specific example, Figure 1 shows a pulse/echo C-scan image (rectified peak amplitude) of a 3"-cube (7.62 cm) of Ti-17 billet material containing nine nominally-identical #1 (diameter: 1/64", 0.0397cm) flat-bottom-holes (FBH). The transducer used in the inspection had a 10-MHz center frequency, 2" (5.08cm) diameter and 15" (38.1cm) focal length, and the water path was chosen to focus the beam about 0.75" (1.905cm) above the FBH plane. The obvious variations of the shapes, sizes and amplitudes of the individual FBH images indicate that the incident beam has experienced significant distortion during propagation to the defect plane. As a result, the nine nominally-identical defects have quite different peak responses.

Another commonly seen manifestation of microstructure-induced beam distortion is the variation of back-wall signal amplitude that occurs when a transducer is scanned across a flat specimen. Figure 2 displays the spectral amplitudes (at 3 frequencies: 3.52MHz, 4.49MHz, 6.05MHz) of the back-wall signal seen in scans of a 2"-thick titanium billet specimen through the axial direction. Two different 5-MHz transducers are used in the experiments. The pictures in the upper panel are the results when using a 1/4"-diameter (0.635cm) planar transducer and a water path of 5 cm, placing the specimen back-wall in the far field of the transducer's radiation field. The pictures in the bottom row are results when using a focused transducer. The focused transducer had a 0.75" (1.905cm) diameter, 8" (20.23cm) geometrical focal length and the water path was chosen to approximately focus the sound beam on the specimen back wall. To quantify the signal fluctuations, we introduce

a dimensionless “fluctuation level”, which is defined as the ratio of the standard deviation (STD,  $\sigma$ ) of the signal amplitudes observed at different positions over their mean ( $\mu$ ). The back-wall amplitude fluctuation levels are quite different for the two cases (20.2%, 25.9%, 31.7% for the planar transducer at 3.52MHz, 4.49MHz and 6.05MHz respectively, and 3.5%, 5.8%, 8.0% for the focused transducer). The examples shown in Figure 1-2 and the earlier work [1-3] clearly indicate that the ultrasonic signal fluctuations depend on many factors including the sample microstructure, the size of the reflector, and the inspection parameters (such as the frequency, transducer focal characteristics, and water path).

The stochastic nature of the ultrasonic response has obvious implications in practical NDT/E. For example, back-wall signal fluctuation may lead to inaccuracy in DAC (Distance-amplitude-correction) values when using back wall signal to estimate the attenuation difference between the calibration standard and the part to be inspected. A critical defect may be missing during an inspection because local microstructural inhomogeneities conspire to reduce the amplitude of the echo from the defect to below the inspection threshold. Thus the flaw signal amplitude fluctuations will broaden the flaw signal distribution curve, which is one of the most important components in the estimation of probability of detection (POD) [4, 5].

We adopt the point of view that the inhomogeneous metal microstructure distorts the incident ultrasonic beam, which, in turn, lead to various signal fluctuations. The relationship between microstructure and the severity of the beam distortions is the topic of a separate on-going study [6]. In the present work we investigate the relationship between beam distortions and signal fluctuations. The goals of this paper are five-fold: (1) to measure through-transmitted distorted fields and explicitly demonstrate various beam distortion effects. (2) To derive an analytical relationship to correlate the back-wall P/E amplitude at one frequency at a given transducer location to the through-transmitted field. (3) To extract the key statistical variables which characterize the distorted field. (4) To develop, based on

(2) and (3), a quantitative Monte-Carlo model predicting the back-wall amplitude fluctuations seen in ultrasonic pulse/echo inspections. (5) To similarly simulate the flaw signal fluctuations following the modeling approach developed in (4) for back-wall signals. The experiments performed in this work were carried out using the same planar and focused transducer as used to produce Figure 2.

The inputs to the Monte-Carlo model include statistical descriptions of various beam distortion effects. We consider two types of amplitude profile distortion, namely: the lateral “drift” of the center-of-energy (pressure square) about its expected position; the distortion of pressure amplitude about its expected pattern; and two types of wave-front distortion (“wrinkling” and “tilting”). The precise meaning of these distortions will be discussed later. The model inputs are deduced by analyzing through-transmission measurements in which the sonic beam emerging from an immersed metal specimen is mapped using a small receiver. The mapped field is compared to the model prediction for a hypothetical homogeneous metal having the same sound speed and energy attenuation rate, and statistical parameters describing the distorted field are deduced using the MLE (maximum likelihood estimation) technique. The modeling approach will be demonstrated using rectangular coupons of jet-engine titanium alloys. Predicted back-wall fluctuation levels at 3 frequencies for both the planar and focused transducer inspections will be compared with the experimental data shown earlier in Figure 2. The modeling approach will then be further tested by using simulated data [6] for three types of model microstructures, and comparing predictions of the Monte-Carlo model with the results of more direct computations. In the last section of this paper, our modeling will be used to simulate signal fluctuations from crack-like reflectors. The predicted fluctuation levels will again be compared with those obtained from the simulated data in reference [6].

## **2. MICROSTRUCTURE-INDUCED BEAM DISTORTIONS**

Microstructure-induced beam distortions are believed to be the primary source of the ultrasonic signal fluctuations seen in inspections of jet-engine titanium alloys. Such alloys often contain large-scale components (macrograins) whose dimensions are large compared to a sonic wavelength [1]. Velocity differences between neighboring macrograins can lead to significant beam distortions [2]. By using the through- transmission (TT) beam mapping setup shown in Figure 3, we can explicitly show various beam distortion effects. For a fixed transmitter location, we scan a small receiver (pinducer) to map the transmitted beam as it emerges into water. At each pinducer location, the RF waveform is acquired. If the pinducer diameter is small compared to the scale of the lateral variations in the emerging pressure field, the received signal is proportional to the local pressure. The transmitted pressure field (amplitude and phase) at any frequency of interest can be extracted by performing FFT operations on the received RF waveforms.

We use the same two transducers and experimental setup as used in acquiring the data for Figure 2. The transducer parameters and the water path were intentionally selected to ensure the incident beams have different beam patterns at the back wall. The pinducer scanning increment is 0.004" (0.01016 cm), which is approximately 1/3 of the wavelength in water (~0.03 cm at 5 MHz). We believe the scanning resolution is high enough to adequately capture the field variations induced by the microstructure. Figure 4 shows examples of pressure fields transmitted through fused-quartz (FQ) and Ti-alloy blocks, with the former serving as a microstructure-free reference. The amplitude profile through the FQ is the expected near-Gaussian shape, while the amplitude profile through the Ti-alloy specimen is clearly distorted. The phases profiles shown in the bottom row in Figure 4 are wrapped between  $\pm\pi$ , and the phase jumps are the results of phase wrapping. Compared to FQ, the amplitude and phase profiles of the through-transmitted beam are noticeably distorted by propagating through the Ti-billet specimen in the axial direction. As observed in our earlier

work, this propagation direction typically leads to the mostly severe signal fluctuations because billet macrograins tend to be elongated in the axial direction [1].

Based on our experimental observations, we have identified four categories of beam distortion effects which we believe play key roles in ultrasonic signal fluctuations. These are illustrated in Figure 5 where hypothetical distorted pressure fields are compared with those of a perfectly homogeneous medium with the same ultrasonic velocity and attenuation. As shown in Figure 5(a-b), the amplitude profile distortions include center-of-energy drift and the amplitude profile “wrinkling”. Such amplitude distortions can be clearly seen in the upper row pictures in Figure 4. The phase distortions we consider consist of 2 effects: wave-front tilting and wave-front “wrinkling”. The effects of wave-front “wrinkling” is noticeable in the phase profile of the beam through the titanium billet specimen shown in Figure 4(d).

Figure 6 further illustrates the phase distortion effects using our measured data. The  $\Delta P$  variable shown in Figure 6(a-b) is the difference between the measured phase of the through-transmitted field from titanium specimen and the phase for a hypothetical homogeneous medium; thus  $\Delta P$  has contributions from both wave-front tilting and wave-front “wrinkling”. Figure 6(a) shows  $\Delta P$  profile before tilting correction. The 2 central lines along the scanning and indexing directions of the  $\Delta P$  profile are plotted in Figure 6(b), allowing the systematical wave-front tilting to be clearly seen. Figure 6(c) shows the two-dimensional  $\Delta P$  profile after a tilting correction has been applied. Figure 6(d) displays the remaining phase difference along the central lines in the scanning and indexing directions after the tilting correction. The tilting correction is achieved by an optimization procedure, in which a planar surface (governed by 3 direction cosine angles,  $\alpha$ ,  $\beta$ ,  $\gamma$ ) is sought to minimize the integrated values of the square of tilted  $\Delta P$ . The remaining phase differences after tilting correction are identified as the  $\Delta\Phi$  values indicated in Figure 5(d).

### 3. MODELING APPROACH

### 3.1 PREDICTION OF P/E OF BACK-WALL SIGNAL USING THROUGH-TRANSMITTED FIELD

As is evident in Figures 2, the pulse/echo back-wall signal can vary substantially when scanning the transducer parallel to the back surface. However, the back-wall signal at a particular transducer location can be predicted by using the data obtained from through-transmission beam mapping. Based on the Thompson-Gray measurement model [7] and Auld's electro-mechanical reciprocity relationship [8], one can show that the back-wall P/E spectrum at angular frequency  $\omega$  at one transducer location above a titanium alloy specimen can be approximated by Eq. (1):

$$\Gamma_{Ti}^{PE}(\omega) = \beta_T(\omega) T_{01}^{Ti} R_{11}^{Ti} T_{10}^{Ti} Att P \iint C_{Ti}(x, y, \omega)^2 dx dy \quad (1)$$

Here,

$\beta_T(\omega)$ : Transducer efficiency coefficient;

$T_{01}^{Ti} R_{11}^{Ti} T_{10}^{Ti}$ : Plane wave transmission and reflection coefficients. "0": water, "1": titanium;

$Att = e^{-2\alpha_0 Z 0^{Ti} - 2\alpha_1^{Ti} Z 1^{Ti}}$ : Attenuation contribution to the wave propagation,  $Ti$ : titanium alloy, and  $\alpha$  is attenuation coefficients and  $Z$  is beam path;

$P = e^{-2ik_0 Z 0^{Ti} - 2k_1^{Ti} Z 1^{Ti}}$ : Propagation effects in phase delay,  $k$ , wave number;

$C_{Ti}(x, y, \omega)$ : A diffraction-related term describing the deviation of the beam profile from a plane wave, evaluated at location  $(x, y)$  along the back wall in titanium

By introducing the corresponding equation for the back-wall spectrum in FQ reference block (denoted by "FQ" in the superscript or subscript) and dividing the two equations, the transducer efficiency coefficient can be canceled. The P/E back-wall spectrum of titanium alloy is then related to the back-wall spectrum of FQ by Eq. (2):

$$\frac{\Gamma_{PE}^{Ti}(\omega)}{\Gamma_{PE}^{FQ}(\omega)} = \frac{T_{01}^{Ti} R_{11}^{Ti} T_{10}^{Ti} ATT^{Ti} P^{Ti}}{T_{01}^{FQ} R_{11}^{FQ} T_{10}^{FQ} ATT^{FQ} P^{FQ}} \frac{\iint C_{Ti}(x, y, \omega)^2 dx dy}{\iint C_{FQ}(x, y, \omega)^2 dx dy} \quad (2)$$



The spectrum of the through-transmitted signal, received by the pin-probe in pitch/catch mode at any one pin-probe position,  $\Gamma_{PC}^{Ti}(x_i, y_i, \omega)$ , is proportional to the particle displacement (sound pressure)  $U(x_i, y_i, \omega)$  at that position, i.e.:

$$\Gamma_{PC}^{Ti}(x_i, y_i, \omega) \propto \beta_R(\omega) U(x_i, y_i, \omega) \propto \beta_R(\omega) \beta_T(\omega) T_{01}^{Ti} T_{10}^{Ti} Att' P' C_{Ti}'(x_i, y_i, \omega) \quad (3)$$

Here,

$\beta_R(\omega)$ : Pinducer efficiency coefficient;

$Att' = e^{-\alpha_0 Z_0 - \alpha_1 Z_1}$ : Same definition as in Eq. (1), one way beam path;

$P' = e^{-k_0 Z_0 - k_1 Z_1}$ : Same definition as in Eq. (1), one way beam path;

$C_{Ti}'(x, y, \omega)$ : Same definition as in Eq. (1), evaluated along the surface just beyond back-wall in water.

Squaring both sides of Eq. (3) and integrating along the surface just beyond back-wall in water, we can show that:

$$\frac{\iint \Gamma_{PC}^{Ti}(x_i, y_i, \omega)^2 dx dy}{\iint \Gamma_{PC}^{FQ}(x_i, y_i, \omega)^2 dx dy} \propto \frac{(T_{01}^{Ti} T_{10}^{Ti})^2}{(T_{01}^{FQ} T_{10}^{FQ})^2} \frac{ATT^{Ti} P^{Ti}}{ATT^{FQ} P^{FQ}} \frac{\iint C_{Ti}'(x, y, \omega)^2 dx dy}{\iint C_{FQ}'(x, y, \omega)^2 dx dy} \quad (4)$$

Since the thickness of the water layer in between the pin-probe and FQ or metal block is

very small (0.05"), we can assume that  $\frac{\iint C_{Ti}'(x, y, \omega)^2 dx dy}{\iint C_{FQ}'(x, y, \omega)^2 dx dy}$  in Eq. (4) is proportional to

$\frac{\iint C_{Ti}(x, y, \omega)^2 dx dy}{\iint C_{FQ}(x, y, \omega)^2 dx dy}$  in Equation (2). Under this assumption, we can finally correlate the

P/E back-wall spectrum in the titanium alloy with the through-transmitted fields measured beneath both blocks:

$$\Gamma_{PE}^{Ti}(\omega) = \Gamma_{PE}^{FQ}(\omega) \frac{T_{01}^{FQ} T_{10}^{FQ}}{R_{11}^{FQ}} \frac{R_{11}^{Ti}}{T_{01}^{Ti} T_{10}^{Ti}} \frac{\iint \Gamma_{PC}^{Ti}(x_i, y_i, \omega)^2 dx dy}{\iint \Gamma_{PC}^{FQ}(x_i, y_i, \omega)^2 dx dy} \quad (5)$$

To test Eq. (5), RF back-wall echoes and their associated spectra were measured at several locations in a Ti-billet specimen. At those transmitter locations, the through-transmitted field emerging from the metal block was mapped using the pinducer, and a reference field was similarly mapped beneath the FQ block. At each transmitter position, Eq. (5) was then used to predict the pulse/echo back-wall spectrum and associated RF signal. The predicted spectrum and RF signal were compared with those directly measured in pulse/echo mode. Results for transmitter locations are shown in Figure 7. We note that the two signals are quite different in the peak-to-peak amplitudes ( $V_{pp} = 58$  and 205 respectively; 255 units = 1 volt). The two signals are well predicted by our formalism in both the time and frequency domain, although some noise due to numerical calculation can be seen. If we extend this idea to many transmitting transducer locations, we can estimate the statistics of the back-wall signal fluctuation from knowledge of the distorted field at those locations. This exercise indicates that we should be able to predict the back-wall signal fluctuations if we can properly model the stochastic characteristics of the distorted fields at different transmitter locations. Thus, the next step is to introduce random variables which describe the beam distortions, and the distribution functions which govern their values.

### 3.2 STATISTICAL VARIABLES CHARACTERIZING DISTORTED FIELDS

If we consider the back-wall signal fluctuation in the frequency domain, the back-wall spectrum varies from location to location. The set of back-wall P/E spectrum seen at different transducer locations may be regarded as resulting from a stochastic process. As indicated in upper portion of Figure 8, the back-wall spectrum at each transducer location can be regarded as one “realization” of a stochastic process. For one particular frequency  $\omega$

within one “realization”, we know that the P/E spectrum is related to the through-transmitted field at that frequency by Eq. (5), i.e., to the amplitude  $A(\omega, x, y)$  and phase  $\Phi(\omega, x, y)$  of the transmitted field. We model the total through-transmitted field as a result of superimposing of two fields: a field transmitted through a hypothetical homogeneous metal sample having the proper average velocity and attenuation, and a randomly varying field which describes the beam distortions due to the microstructure, i.e.

$$A(\omega, x, y) = A_0(\omega, x, y) \left\{ 1 + \frac{\Delta A(\omega, x, y)}{A_0(\omega, x, y)} \right\} \quad (6)$$

$$\Phi(\omega, x, y) = \Phi_0(\omega, x, y) + \Delta P(\omega, x, y) \quad (7)$$

$\Delta A$  is defined as in Figure 5.  $\Delta P$  includes both the phase variation caused by wave-front tilting and wave-front “wrinkling”. The hypothetical homogeneous field ( $A_0, \Phi_0$ ) can be predicted from the measured FQ field by employing a suitable beam model. For this purpose, we have used the so-called Multi-Gaussian beam model with 15 (Gaussian) expansion functions [17, 18]. The prediction of  $A_0(\omega, x, y)$  and  $\Phi_0(\omega, x, y)$  in this manner requires the knowledge of the velocity and attenuation of the homogeneous metal. These quantities are determined by measurements. Velocity is determined by measuring the time delays between successive back-wall reverberations averaged over different lateral positions of the planar transmitting probe. Attenuation as a function of frequency is determined by integrating the square of the through-transmitted response over area to determine the total energy carried by the emerging sound beneath both the FQ and titanium specimen, and then assuming that the attenuation of FQ is negligible. The detailed procedure is discussed in reference [2].

The lower panel of Figure 8 illustrates the procedure used to deduce the random field at each transmitting probe location. For example, at transducer location #1, the random field at

each point  $(x, y)$  in the pinducer scan pattern is deduced by comparing the hypothetical homogeneous field  $(A_0(\omega, x, y), \Phi_0(\omega, x, y))$  with measured through-transmitted field. To characterize the random field, we introduce the following random variables (see Figure 5):  $\Delta D$  to describe the shift in the center of energy from its expected position;  $\Delta A/A_0$  to describe amplitude “wrinkling” (after the center-of-energy drift has been removed);  $\theta$  to describe the systematical “tilting” of the wave-fronts; and  $\Delta\Phi$  to describe the phase “wrinkling” after the “tilting” correction by rotation through the tilting angle  $\theta$ . Here  $\Delta D$  and  $\theta$  are “global” variables, while  $\Delta A/A_0$  and  $\Delta\Phi$  are determined separately at each pinducer location  $(x, y)$ . If the total field  $(A, \Phi)$  is measured at a sequence of transmitter positions (1~N), the statistical descriptions of the random variables can be estimated. The importance of the statistical descriptions of the random variables will be discussed later.

The random field variables are determined in the following order:  $\Delta D$ ,  $\Delta A/A_0$ ,  $\Delta P$  (the combination of wave-front “tilting” and “wrinkling”),  $\theta$ ,  $\Delta\Phi$  (wave-front “wrinkling” only). Note that, the center-of-energy drift of the through-transmitted field is determined first, even though it does not directly affect the integral in Eq. (5). Because a simple lateral shift of distorted beam does not affect the values of the integrals in Eq. (5). As discussed earlier, the phase tilting angle  $\theta$  is determined by an optimization procedure to locate a planar surface, governed by 3 direction cosine angles, to minimize the phase variation. However, because of the axial symmetry of the homogeneous beam, it is equivalent to using just one direction cosine angle to characterize the wave-front tilting. We select the direction cosine angle relative to the beam propagation direction.

The spatial correlations of  $\Delta A/A_0$  and  $\Delta\Phi$  are also of interests because they are describe how rapidly each variable varies in space. We characterize the spatial variations of these variables by using their average auto-correlation functions along the scanning and indexing directions. The spatial correlation length (SCL) is defined as the distance over which the auto-correlation function falls by  $1/e$  [9].

The statistical description of some variables may depend on the way we choose to manipulate the data. For example, when dealing with  $\Delta\Phi$ , we have to define the phase origins (zero phase) for both the hypothetical homogeneous field and the measured distorted field. We select the position corresponding to the energy center of the field as the phase origin. Based on our measured data, the distributions of  $\Delta A/A_0$ ,  $\Delta\Phi$  and  $\theta$  generally can be roughly approximated as Gaussian distributions, and the parameters (means and variances) that characterize these distributions have been estimated from the through-transmitted data using the “maximum likelihood estimation” (MLE) technique [19]. When estimating parameters for the  $\Delta A/A_0$  and  $\Delta\Phi$  distributions, we weight the data using the energy spatial distribution of the hypothetical homogeneous field ( $|A_0(w, x_i, y_i)|^2$ ). This is done to limit the contributions from the data points with very small energy, which can have quite large  $\Delta A/A_0$  values.

The “goodness” of the Gaussian approximation is qualitatively evaluated using a quantile-by-quantile plot (QQplot) [20]. Figure 9 illustrates the histograms and QQplots of  $\Delta A/A_0$  and  $\Delta\Phi$  at 4.49 MHz for both the planar and focused transducer cases. The through-transmission measurements were made on a Ti-17 billet specimen with beam propagation in the axial direction. As discussed early, the elongated large-scale macrograins in such specimens tend to seriously distort the incident beam. The water path for planar transducer case is again 5 cm and the water path for the focused transducer case was selected to approximately focus the sound beam on the specimen back wall. If the distributions governing  $\Delta A/A_0$  and  $\Delta\Phi$  were perfect Gaussian, the QQplots in Figure 9 would be straight lines [20].

As is clear from Figure 9, the details of beam distortion are different for planar and focused beams, and their statistical parameters are consequently different. Through-transmission beam mapping measurements were carried out at 9 locations in the Ti-billet block using planar transmitter, and at 11 locations using focused transmitter. At each

transmitter location, the measurements yield many values of  $\Delta A/A_0$  and  $\Delta\Phi$ , but only one value each of  $\Delta D$  and  $\theta$ . Thus our measurements are too sparse to accurately estimate the distribution governing  $\Delta D$  and  $\theta$ . Unlike that of  $\Delta D$ , the distribution governing  $\theta$  plays a role in the estimation of P/E signal fluctuations using Eq. (5). We will assume that  $\theta$  is also governed by a Gaussian distribution, specified by its mean and standard deviation for a small number of measurements.

The statistical parameters governing the distributions of these variables were determined at 3 different frequencies within the bandwidths of the transmitters and receiver: 3.52 MHz, 4.49 MHz and 6.05 MHz. Since the back-wall signal fluctuation levels are quite different at different frequencies, we expect these parameters vary with frequency. The manner in which the statistical parameters change with frequency is summarized in Figure 10. For both the planar and focused transmitter cases, the standard deviations (square root of variances) of  $\Delta A/A_0$ ,  $\Delta\Phi$  and  $\theta$  generally increase with frequency; the SCL of  $\Delta A/A_0$  and  $\Delta\Phi$  decreases with frequency. These results are sensible because beam distortions are expected to be more severe when the wavelength is shorter compared with the microstructure scale.

As noted above, we use SCLs to describe how rapidly  $\Delta A/A_0$  and  $\Delta\Phi$  vary in space. It is illuminating to compare the measured SCLs with the beam diameter, since the latter sets the scale of variations in the absence of microstructure. The -6dB beam diameter at the back-wall at each frequency of interest has been calculated for the transmitted field of the hypothetical uniform metal. Figure 11 summarize the relationship between the beam diameters and the SCLs of  $\Delta A/A_0$  and  $\Delta\Phi$  at 3 frequencies. As expected, the beam diameters for both the planar and focused probe cases decrease with frequency. SCLs generally increase with beam diameter (or decrease with frequencies), but their values are much smaller than the corresponding beam diameters. For example, the SCLs are roughly one tenth of the beam diameter for the focused transducer case. Such results are consistent with the observations for the SCLs of the backscattered signal from grain microstructure or porosity in some earlier studies [15, 16]. A separate theoretical and experimental

investigation has been carried out to more quantitatively understand the spatial correlation of the backscattered grain noise [21].

### 3.3 PREDICTION OF BACK-WALL SPECTRUM AMPLITUDE FLUCTUATION

Once we have in hand the distributions governing the random beam distortions, we can use Eq. (5) to predict the back-wall fluctuation level, which was defined as the ratio of the standard deviation of back-wall signals over their mean. The prediction makes use of a “Monte-Carlo” simulation [14]. Specifically, for each transmitter position we first generate a synthetic distorted field just below the metal back-wall obeying the proper statistics. We then use Eq. (5) to predict the back-wall spectrum. The process, which makes use of random number generator, is repeated 200 times, corresponding to 200 transmitter positions, or 200 realizations of the microstructure. The fluctuation level of the back-wall spectrum amplitude is estimated from the results of the 200 simulations.

The detailed procedure for a given frequency is as follows. Step 1: In accordance with their distributions (as specified by the mean, STD and SCL), we generate two-dimensional random “rough surfaces” over the back-wall grid to simulate  $\Delta A/A_0$  and  $\Delta\Phi$  (wave-front “wrinkling”) as function of  $x$  and  $y$ . To ensure the generated surfaces have the statistics specified, we use the “spectrum method”, which can be found in the literature [9-13, 22] dealing with the wave scattering from random rough surfaces. The spatial correlation functions of the 2D random “rough surfaces” are approximated as Gaussian correlation functions (GCF). Examples are shown in Figure 12. The measured spatial correlation functions (MCF) for  $\Delta A/A_0$  and  $\Delta\Phi$  at 4.49 MHz, normalized to unity, are compared with GCFs having the same SCLs. Generally, Gaussian functions are seen to be reasonable approximations for the measured spatial correlation functions of the random variables of interests ( $\Delta A/A_0$  and  $\Delta\Phi$ ). Step 2: Using a random number generator, a wave-front tilt angle is selected in accordance with its governing distribution. Step 3: Using Eq. (6) and (7), we

reconstruct the through-transmitted field by applying all of the above distortion variables to the model-predicted field transmitted through a homogeneous metal. An example of one such predicted through-transmitted field for a planar at 4.49 MHz is in Figure 13. There the simulated field (amplitude and phase) is compared with one measured distorted field. Even though reconstructing one single ensemble member is not a meaningful characterization of a stochastic process, we do see the similarity between the general features of the measured and the reconstructed fields. We take this as confirmation that our understandings of the various beam distortion effects are appropriate. Step 4: We predict the pulse/echo back-wall spectrum amplitude at one transmitter location by integrating the square of the pressure of the reconstructed distorted field over the back wall, in the fashion of Eq. (5). Step 5: We repeat the process for many members of the “ensemble” (hypothetical transmitter positions) so that the fluctuation level of the back-wall spectrum can be evaluated.

#### **4. COMPARISON BETWEEN THEORY AND EXPERIMENT**

To test the modeling approach, we have used it to predict the statistical characteristics (mean and STD) of the back-wall responses shown earlier in Figure 2. Recall that a single Ti-billet specimen was used, and measurements were made with two transducers, one planar and one focused, resulting in quite different fluctuation levels. For each transducer, the required beam distortion parameters were deduced from through-transmission measurements at about 10 positions, and model calculations of P/E amplitude were made for 200 simulated transducer positions. The predicted and experimental results are summarized in Figure 14. The upper two panels present results for the planar transducer case and the results for the focused transducer are shown in the bottom panels. The measured and the predicted mean amplitudes at 3 frequencies are shown in the left-hand side panels and the measured and predicted fluctuation levels are shown in the right hand panels. Generally, the model was found to work very well in both cases for all the 3 frequencies. The modeling approach has been further tested by using simulated data, as discussed in



reference [6]. Predicted P/E fluctuation levels for three types of model microstructures were found to be in good agreement with the results of more direct computations. This indicates that our modeling approach can successfully relate beam distortion parameters to signal fluctuation levels.

## **5. SIMULATION OF ULTRASONIC FLAW SIGNAL FLUCTUATIONS**

The fluctuation of ultrasonic responses from small internal flaws is of great interest in industrial inspections. As discussed in the previous section of this paper, complete understanding of flaw signal fluctuations is essential in flaw characterization and POD estimation. Several experimental investigations [1, 3, 15] have been carried out to directly measure flaw signal fluctuations in specific microstructures. In these experiments, a limited number (typically 9) of identical FBHs were drilled in a specimen of interest, and the peak response from each FBH was measured. Multiple measurement trials were conducted using different beam focal conditions at the FBH depth. The different beam focal conditions were achieved by either changing the water or the metal path or both. To be consistent with practical operations in industry, a 2 two-dimensional raster scan of the transducer above the specimen was made and peak FBH amplitudes were deduced from C-scan images of each FBH. The FBH signal fluctuations level (standard deviation/mean) was then estimated from the measured 9 peak amplitude values for each focal condition studied.

For rough preliminary estimates of defect signal fluctuation levels, 9 measured responses may be sufficient if the locations of the 9 FBHs are randomly selected and the sample is macroscopically homogeneous. However, a larger number of FBH responses is desired for more detailed statistical analysis. This may be prohibitively expensive in practice due to the cost of fabricating specimens containing FBH defects. An alternative approach is to measure beam distortion parameters in a representative sample of material, and to then use our Monte-Carlo approach to estimate signal fluctuation levels for FBH (or other) defects.

Under the Kirchhoff approximation, the pulse/echo response from a small crack-like reflector larger than a few wavelengths can be evaluated in the same way as shown in Eq. (5), except that the integral of  $\iint \Gamma_{TI}^{PC}(x_i, y_i, \omega)^2 dx dy$  is evaluated over the crack surface instead of over the entire back wall [18]. To demonstrate our approach, we assume the flaw to be a square flat bottom hole (SFBH), and we consider 3 different full widths for the SFBH (point reflector, 1, 4 times of the wavelength at 3.5 MHz in metal). The square shape was chosen to simplify numerical integration. Because of the good earlier agreements between the measured and the predicted back-wall signal fluctuations, we assume the same beam-distortion statistical parameters as used before. For each simulation trial, we first generate a through-transmitted distorted field along the back-wall grid. Then to simulate peak amplitude detection in scanning inspections, we “scan” the SFBH along the back-wall until the integral  $\iint \Gamma_{TI}^{PC}(x_i, y_i, \omega)^2 dx dy$  over the SFBH achieves its maximum value. As before, each generated distorted field corresponds to one microstructural ensemble, so we can repeat the simulation for many microstructural ensembles. The resulting peak responses can be used to estimate the “flaw” signal fluctuation level.

Figure 15 qualitatively demonstrates the simulation processing. All the images shown in Figure 15 are for the case of a planar transducer operated at a fixed frequency of 6MHz. The pictures in the top panels are for the hypothetical homogeneous field in the absence of microstructure. Figure 15(a) displays the field amplitude (pressure square) with the relative scale of the indicated SFBH. Figure 15(b) is the resulting SFBH “C-scan” image when we scan the SFBH through the homogeneous field. In general, when the reflector is much larger than the beam diameter, the resulting C-scan image is determined largely by the flaw shape;

while when the reflector is smaller than the beam diameter, the c-scan image mirrors the beam amplitude pattern. For the case shown in Figure 15b, the beam diameter is close to the SFBH side length but it is smaller than the SFBH diagonal length. We can clearly see the square “envelope” of the SFBH in the amplitude pattern of Figure 15(b). The bottom panels of Figure 15 display corresponding results for one generated distorted field. Because the field is distorted, the SFBH scanned image is no longer symmetrical, and the “squarish” pattern is less distinctive.

Figure 16 summarizes the simulation results. For comparison, we regard the back-wall as a large reflector, and the back-wall fluctuation level is also shown (corresponding to the largest reflector). The assumed beam distortion parameters are the same as those measured in the early beam mapping experiments in the Ti-billet block. Figure 16 shows the predicted SFBH signal fluctuation levels at 3 frequencies for both planar probe and focused probe inspections. The predicted signal fluctuation level is seen to depend on the reflector size, inspection frequency and the probe focal condition at the SFBH depth (2”). No direct test of these predictions is possible since the specimen contains no SFBH defects.

An indirect test of our modeling approach can be made by comparison to the prediction of other models. Figure 17 summarizes one such comparison. The two-dimensional generated microstructures to be considered are shown in Figure 2 of reference [6] (random medium (1) and random medium (2)). The distorted sonic field in the metal was calculated in reference [6] based on a 2D scalar model and the insonifying sound was 5 MHz, from a planar transducer. From the distorted field, the P/E signal from a one-dimensional crack-like reflector could be inferred, and signal fluctuation levels could be determined by combining several hundred such grain ensembles. Our method was applied to such 2D problems, with the directly-calculated distorted fields serving as the “experimental data” that was used to determine the various statistic parameters. These statistics parameters were then used to generate synthetic distorted field from which peak flaw signal amplitude were predicted (for

one-dimensional scanning). Signal fluctuation levels computed by the two methods are compared in Figure 17 for 1D crack-like reflector of different lengths. We note that the results from our Monte-Carlo modeling approach are in reasonable agreement with the simulated data but tend to overestimate the fluctuation level. Note that the fluctuation level from small reflector depends not only on the microstructure but also on the reflector size.

## 6. SUMMARY AND FUTURE WORK

Beam distortions induced by the metal microstructure are believed to be the source of ultrasonic signal fluctuations seen in many inspections of titanium-alloy, jet-engine materials. Such beam distortions were systematically investigated in this paper. Key beam distortion effects (center-of-energy drift, amplitude profile “wrinkling”, phase-front tilting and phase-front “wrinkling”) were demonstrated and quantified using through-transmission beam mapping techniques. An analytical relationship was derived to correlate the P/E spectrum at one transducer location to the through-transmitted field exiting the metal specimen. Based on the analytical relationship, a quantitative Monte-Carlo model was proposed as a means for predicting back-wall (pulse/echo) signal fluctuations, given certain statistical variables that describe the pressure-field distortions. The model was tested and found to be in good agreement with the experiment. Following the same modeling approach, efforts were made to predict flaw signal fluctuations although the corresponding measurements are unavailable. The simulation indicates that the signal fluctuation level for a collection of identical reflectors depends on the microstructure, inspection frequency, reflector size and the transducer focal condition at the reflector depths.

The principal contribution of this study is to demonstrate that the statistical parameters describing various beam distortion effects are physically meaningful quantities for the microstructure-induced ultrasonic signal fluctuations. The work described in this paper is the first step toward a comprehensive theory. The next step involves describing how a specific microstructure and experimental set-up (transducer focal characteristics, frequency) lead to

specific beam distortion statistics. Initial efforts along these lines are discussed in article [6]. That work also critiques and validates our approach to fluctuation modeling for three specific simulated (model) microstructures.

## ACKNOWLEDGEMENTS

This material is based upon work supported by the Federal Aviation Administration under Contract #DTFA03-98-D-00008, and performed at Iowa State University's Center for NDE as part of the Engine Titanium Consortium program, through the Airworthiness Assurance Center of Excellence.

## REFERENCES

1. P. D. Panetta, F. J. Margetan, I. Yalda and R. B. Thompson, "Observation and interpretation of microstructurally induced fluctuations of back-surface signals and ultrasonic attenuation in titanium alloys", *Review of Progress in QNDE* Vol. 16B, eds. D.O. Thompson and D.E. Chimenti, (Plenum Press, N.Y., 1997), p. 1547-1554.
2. F.J. Margetan, P.D. Panetta, and R.B. Thompson, "Ultrasonic signal attenuation in engine titanium alloys", *Review of Progress in QNDE* Vol.17B, eds. D.O. Thompson and D.E. Chimenti, (Plenum, New York, 1998) p. 1469-1476.
3. F. J. Margetan, H. Wasan, and R. B. Thompson, "An experimental study of microstructure-induced ultrasonic signal fluctuations in jet-engine titanium alloys", *Review of Progress in QNDE* Vol.19B, eds. D.O. Thompson and D.E. Chimenti, (AIP, Melville NY, 2000) p.1433-1440.
4. Alan P. Berens, Metal Handbook, Vol. 17, 9<sup>th</sup> Edition: Nondestructive Evaluation and Quality Control. ASM International, Materials Park, Ohio 44073. p.689-701.

5. R.B. Thompson, Frank J. Margetan, "Use of elastodynamic theories in the stochastic description of the effect of microstructure on ultrasonic flaw and noise signals", *Wave motion* 36 (2002) p.347-365.
6. A. Li, L. Yu, R. Roberts, F. J. Margetan and R. B. Thompson, "A 2-D numerical simulation study of microstructure-induced ultrasonic beam distortions", *Review of Progress in QNDE* Vol.23B, eds. D.O. Thompson and D.E. Chimenti, (AIP, Melville NY, 2004) p.1178-1186.
7. R. B. Thompson and T. A. Gray, "A model relating ultrasonic scattering measurements through liquid-solid interface to unbounded medium scattering amplitudes", *J. Acoust. Soc. Am.* 74, (1983), p.1279.
8. B. A. Auld, "General electromechanical reciprocity relations applied to the calculation of elastic wave scattering coefficients", *Wave Motion* 1, 1979, p.3.
9. J. A. Ogilivy, Theory of wave scattering form random rough surfaces, Adam Hilger, Bristol, Philadelphia and New York, 1991.
10. L. Tsang, J.A. Kong, K.H. Ding, and C.O. Ao, Scattering of electromagnetic waves, volume ii: numerical simulations, John Wiley and Sons Inc., New York, 2001.
11. N. Garica and E. Stoll, "Monte-Carlo calculation for electromagnetic-wave scattering from random rough surface", *Physical Review Letters*, Vol. 52, Number 20, 1984. p. 1789.
12. Richard S. Keiffer and Jorge C. Novarini, "A time domain rough surface scattering model based on diffraction: application to low-frequency backscattering from two-dimensional sea surfaces", *J. Acoust. Soc. Am.* 107, (2000), p. 27.
13. Karl F Warnick and Weng Cho Chew, "Numerical simulation for rough surface scattering", *Waves in Random Medium*, 11 (2001).
14. M. E. J. Newman and G. T. Barkema, Monte-Carlo methods in statistical physics, Oxford University Press Inc., New York, 1999.

15. Frank Margetan, Linxiao Yu, Bruce Thompson. Unpublished technical report on FBH and Back wall fluctuation levels in three Ti 6Al-4V forging materials, Sept 2002 Center for NDE at Iowa State University.
16. D.K. Hsu, D.O. Thompson, R.B. Thompson, "Evaluation of porosity in aluminum alloy casting by single-sided access ultrasonic backscatter", *Review of Progress in QNDE*, eds. D.O. Thompson and D.E. Chimenti, Vol.5B (1986), p1633-1642.
17. A. Minachi, F. J. Margetan, R.B. Thompson, "Reconstruction of a piston transducer beam using muti-Gaussian beam (MGB) and its application", *Review of Progress in QNDE*, eds. D.O. Thompson and D.E. Chimenti, Vol.17 (1998), p. 907.
18. A. Minachi, F. J. Margetan and D.K. Hsu, "Delamination sizing in composite materials using the Gaussian-Hermite beam model", *Ultrasonics*, Vol. 31, No.4, p.237 (1993).
19. W.Q. Meeker, L.A. Escobar, Statistical methods for reliability data, John Wiley and Sons, Inc., New York, 1998.
20. J. Neter, M.H. Kutner, C.J. Nachtsheim, W. Wasserman, Applied linear statistical models (4<sup>th</sup> edition), Chicago: Irwin, c1996.
21. R. B. Thompson, Linxiao Yu and F. J. Margetan, "A formal theory for the spatial correlation of backscattered ultrasonic grain noise", *Review of Progress in QNDE*, 2004, Golden, Colorado.
22. Vincent Lupien, "The role of scale structure in scattering from random rough surfaces", *J. Acoust. Soc. Am.* 105 (4), (1999), p. 2187.

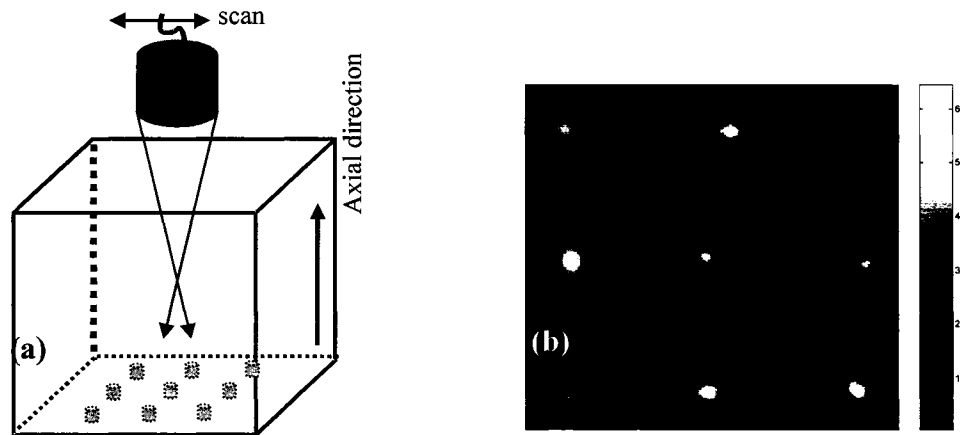


**FIGURE 1.** Ultrasonic signals of 9 nominally-identical FBHs in a Ti-alloy specimen. The C-scan image displays the rectified peak signal amplitude in a time gate centered at the FBH depth.

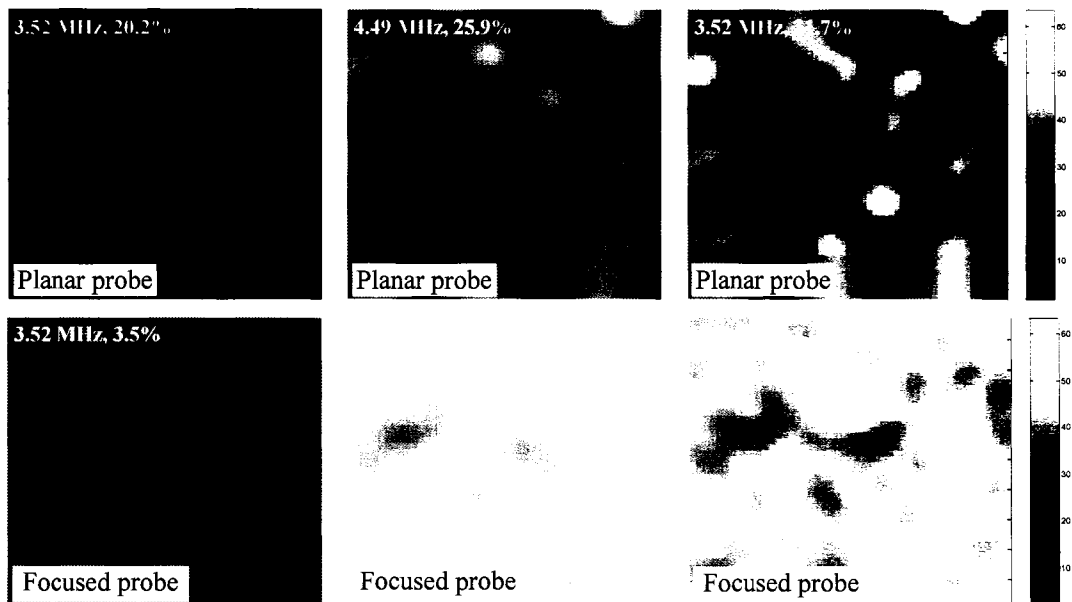


**FIGURE 2.** Back-wall spectral amplitudes at 3 frequencies for two-dimensional scans over a flat Ti-alloy specimen. Upper panel: planar transducer. Bottom panel: focused transducer.



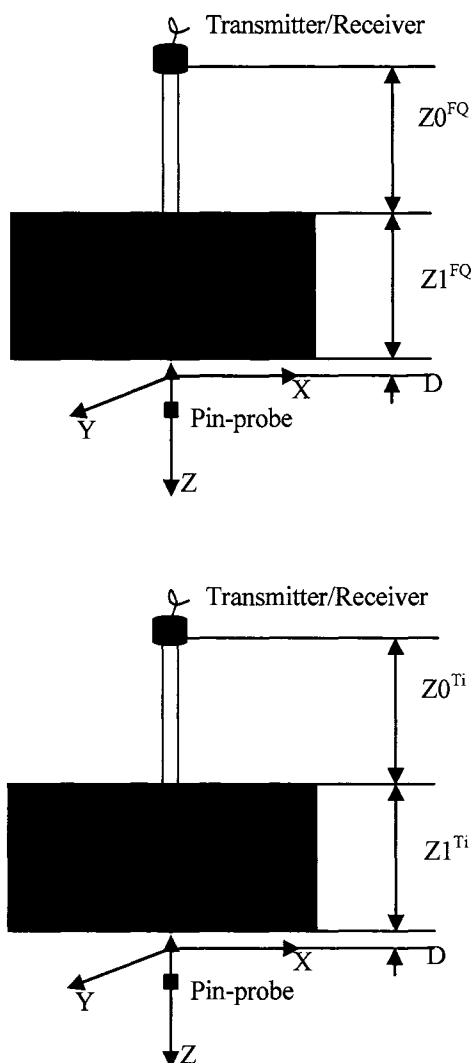


**FIGURE 3.** Through-transmission beam mapping setup. A fused quartz block serves as a homogeneous, non-attenuating reference. The small receiver (pinducer) has a diameter is 0.04" (0.1016 cm).

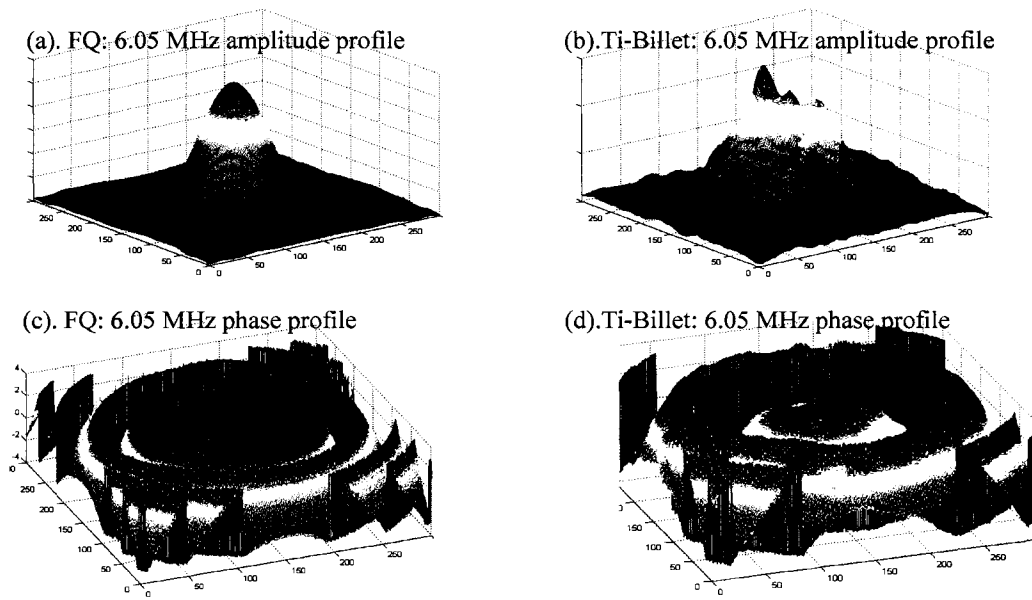


**FIGURE 4.** Through-transmitted amplitude and phase profiles observed in beam-mapping experiments using a fused-quartz block and 2"-thick Ti-alloy specimen. A  $\frac{1}{4}$ "-diameter planar transducer was used, and results are shown for the 6.05-MHz component of the received signal as a function of the lateral scanning coordinates X and Y (in units of 0.004 inches). Phase is wrapped between  $\pm \pi$ .

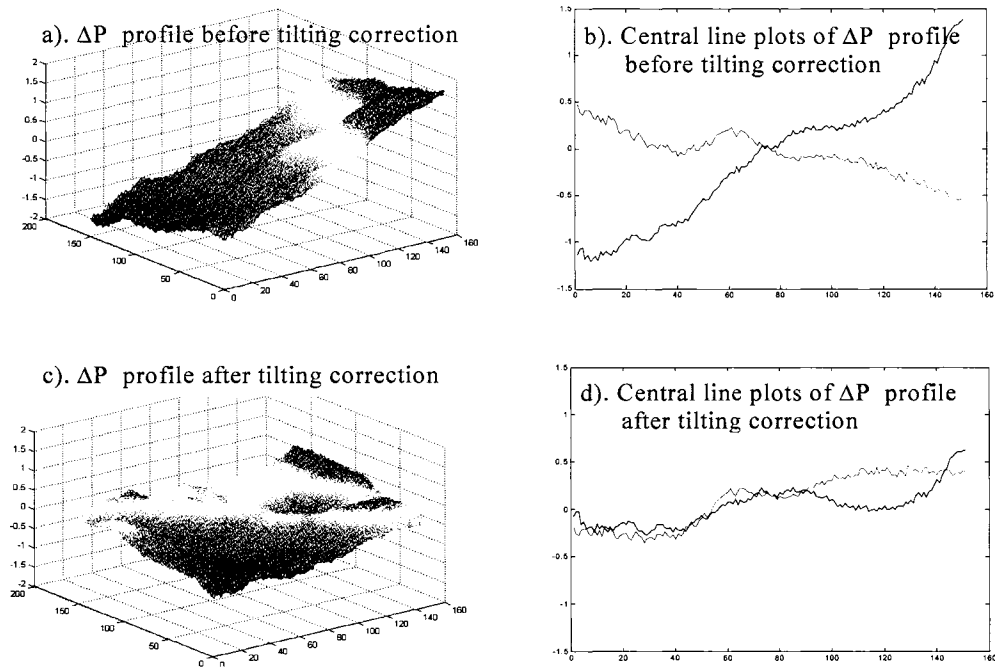


**FIGURE 5.** Four categories of beam distortion effects: a). drift of the center of energy; b). “wrinkling” of amplitude profiles; c) wave-front tilting; d). wave-front “wrinkling”. The overall wave-front distortion is denoted as  $\Delta P$ .

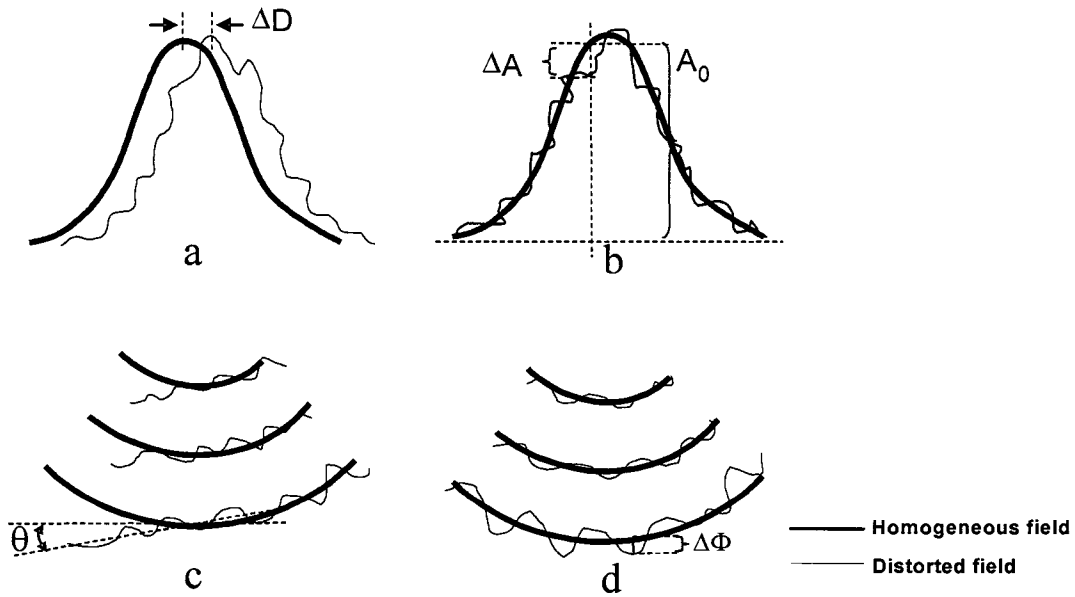


**FIGURE 6.** Wave-front tilting and “wrinkling” for a planar transducer case. Results are shown for the 4.49 MHz component of the through-transmitted beam.

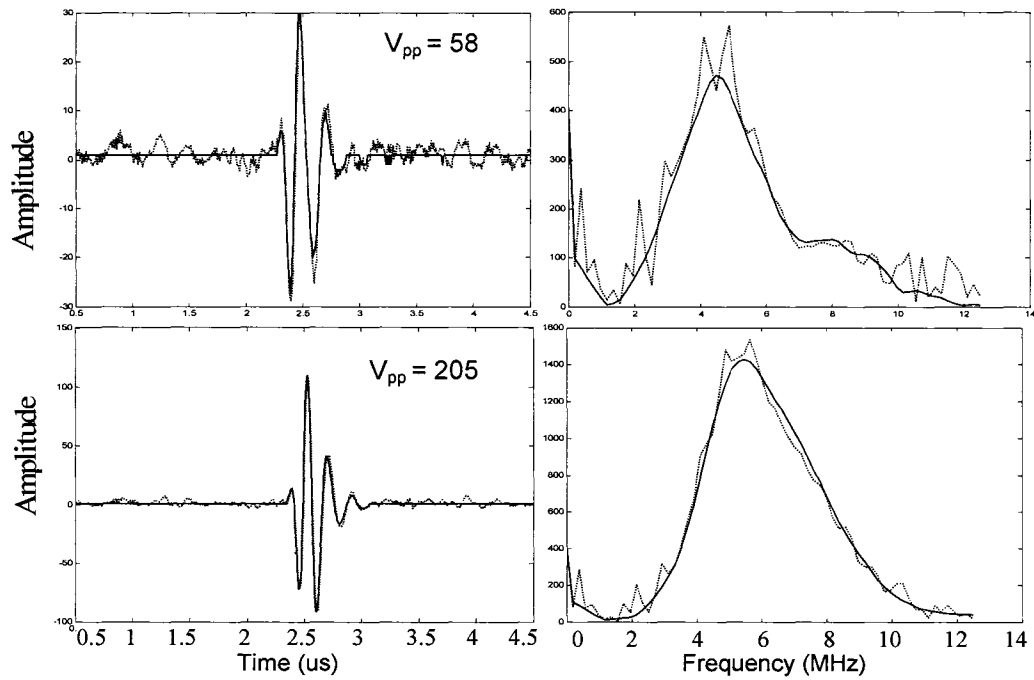


**FIGURE 7.** Predicted back-wall signals and spectra at two locations in a Ti-billet specimen. The 5 MHz, 0.25" diameter planar transducer was used. Dash lines: model predictions; Solid lines: experiment.

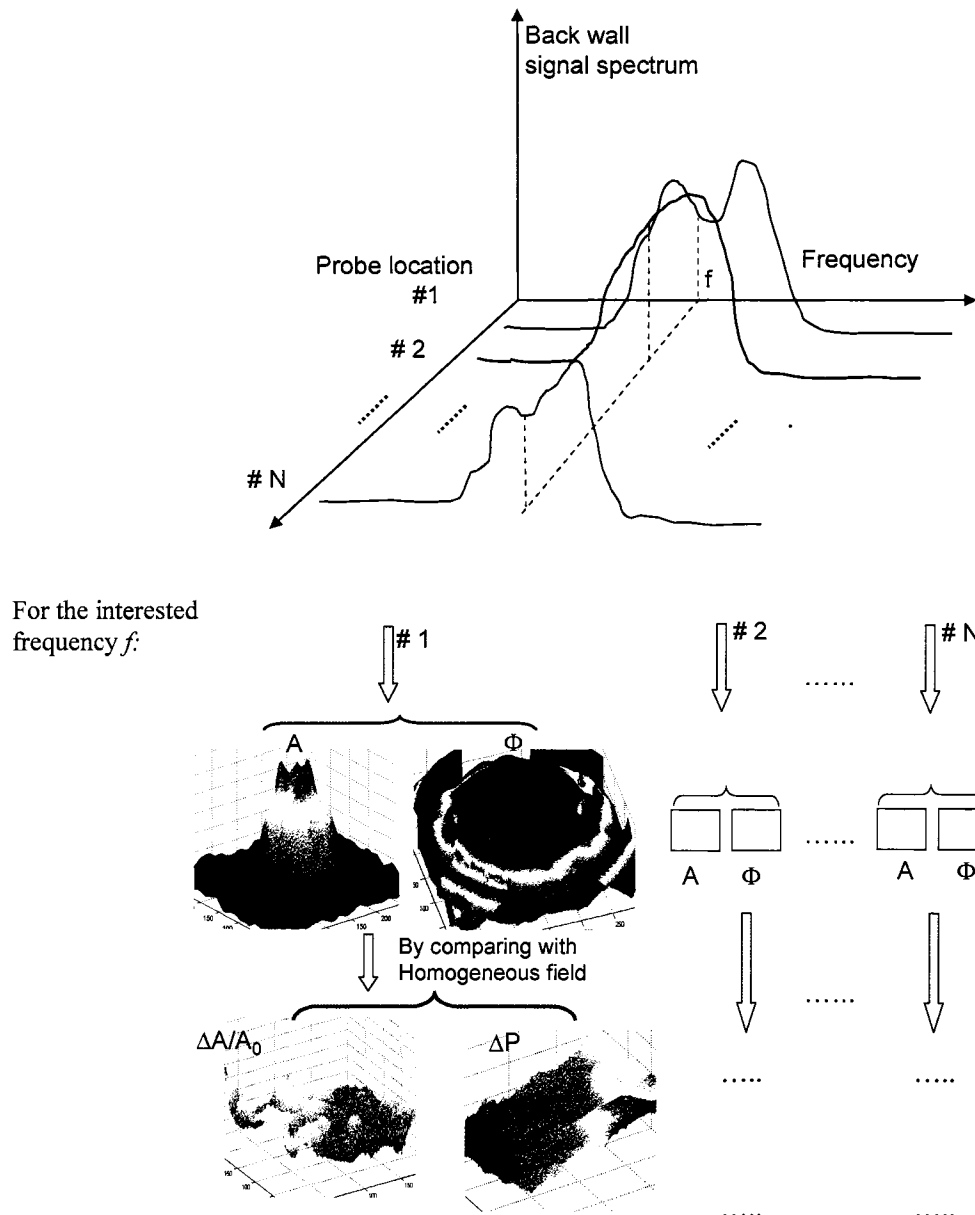


**FIGURE 8.** The procedure used to measure beam distortion variables (at a given frequency) from through-transmission data.

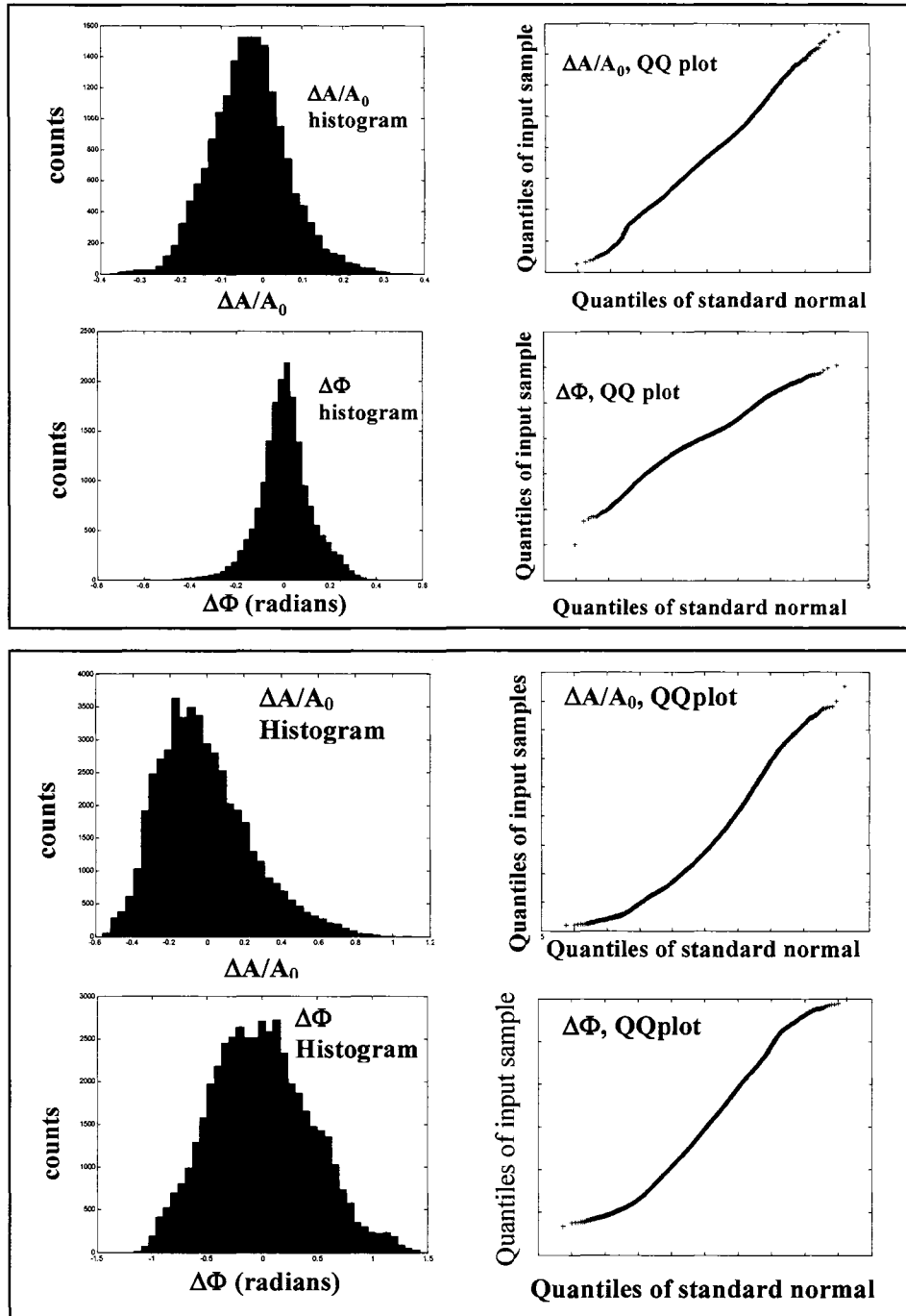


**FIGURE 9.** Histograms and QQplots of the beam-distortion variables  $\Delta A/A_0$  and  $\Delta\Phi$  at 4.49 MHz for through-transmitted measurements made using focused (upper panel) and planar (lower panel) transmitting probe. Sample: Ti-17 billet sample, axial direction, 2" thick. Reference block: 2"-thick FQ.

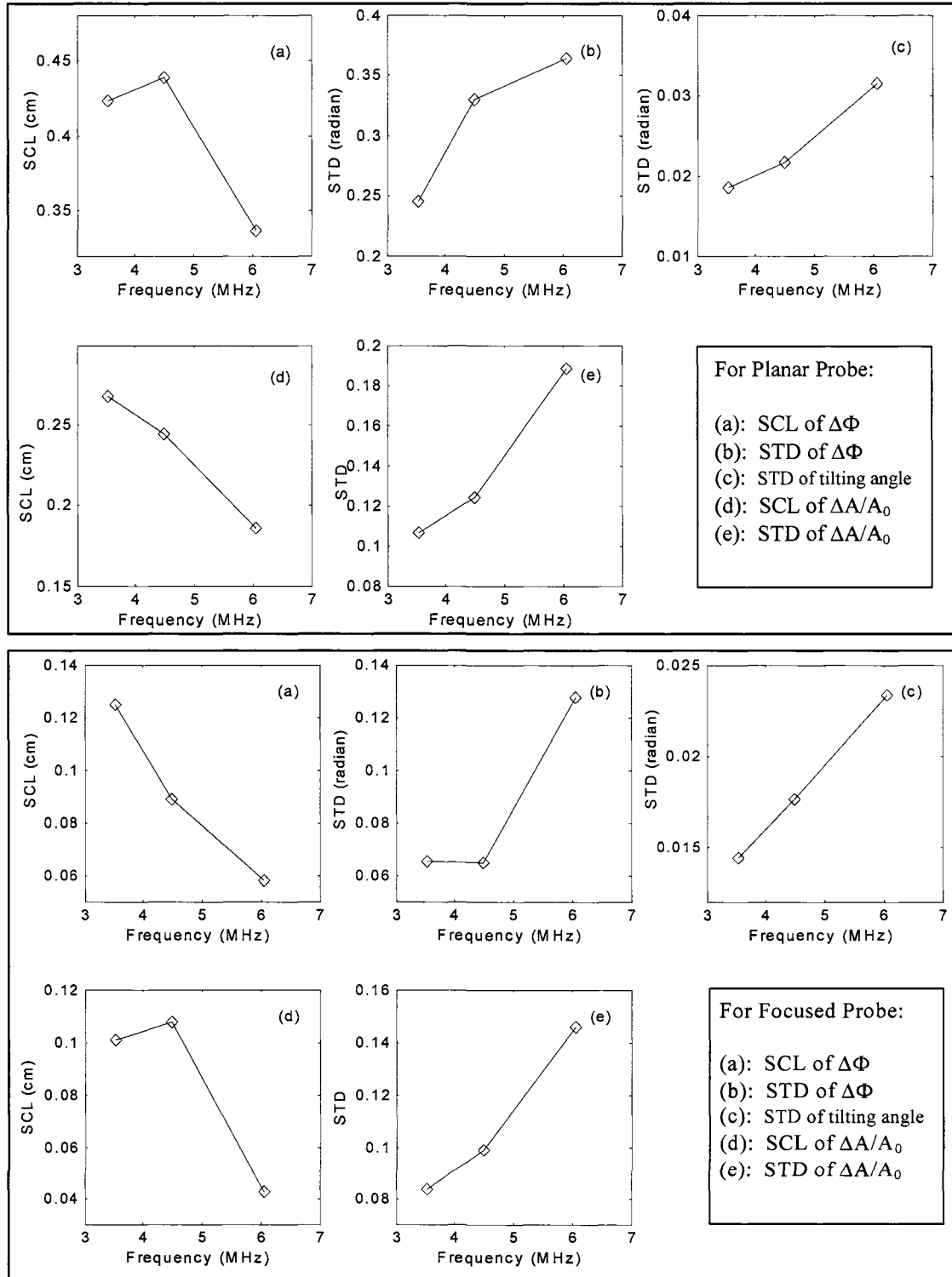


**FIGURE 10.** How the statistical parameters governing beam distributions vary with frequency. Upper panel: planar transducer; Lower panel: focused transducer.

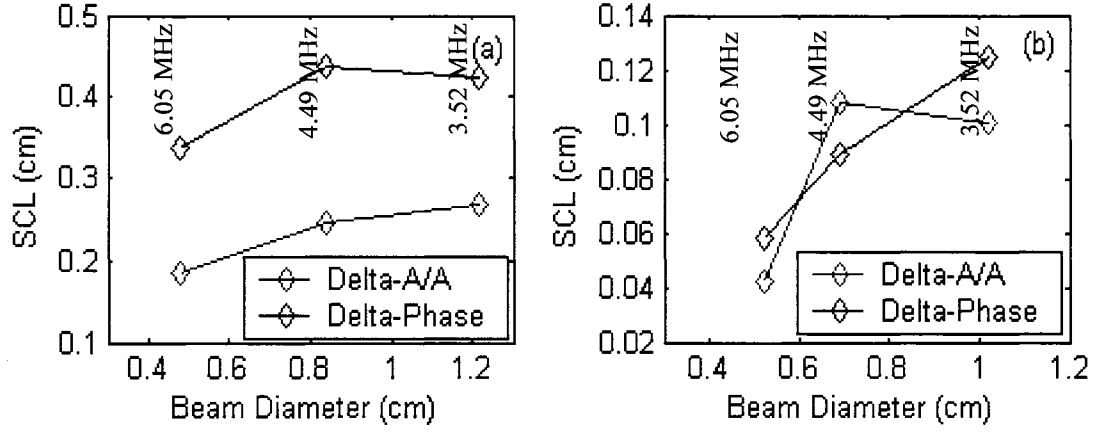


**FIGURE 11.** The relationship between beam diameter and SCLs of  $\Delta A/A_0$  and  $\Delta\Phi$  at 3 frequencies. a). planar transducer; b) focused transducer. For each data point, the corresponding frequency is indicated near the top of each graph.

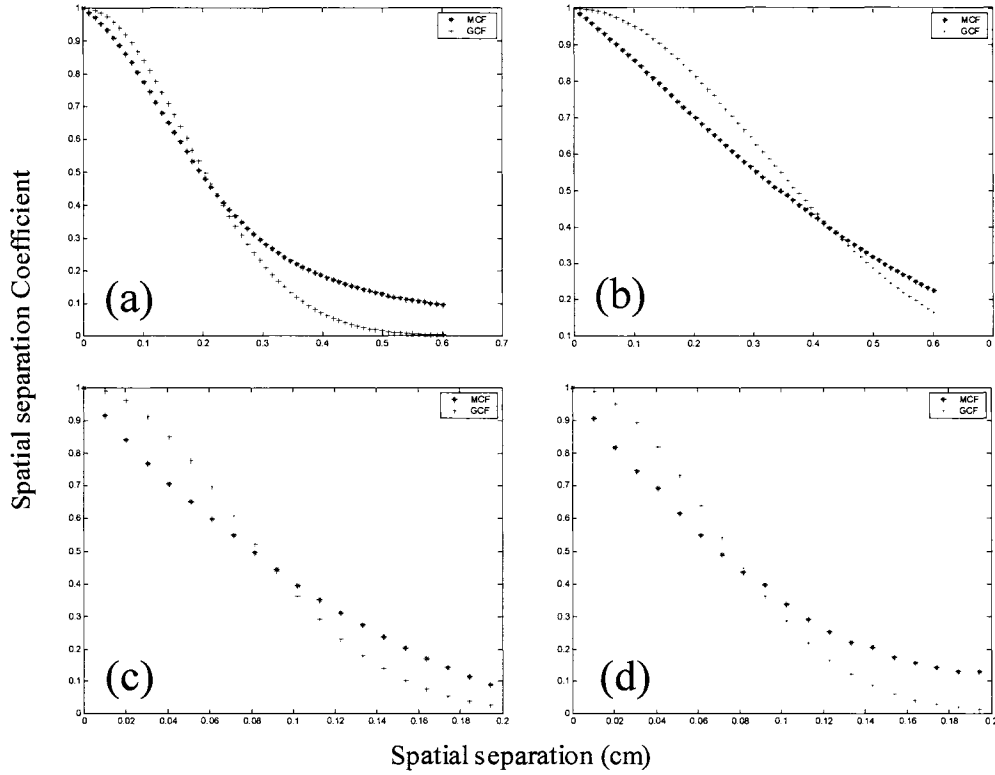


**FIGURE 12.** The measured spatial correlation functions and the approximate Gaussian correlation functions used in our model calculation at 4.49 MHz. (a) Planar transducer  $\Delta A/A_0$ ; (b) Planar transducer  $\Delta\Phi$ ; (c) Focused transducer  $\Delta A/A_0$ ; (d) Focused transducer  $\Delta\Phi$ .



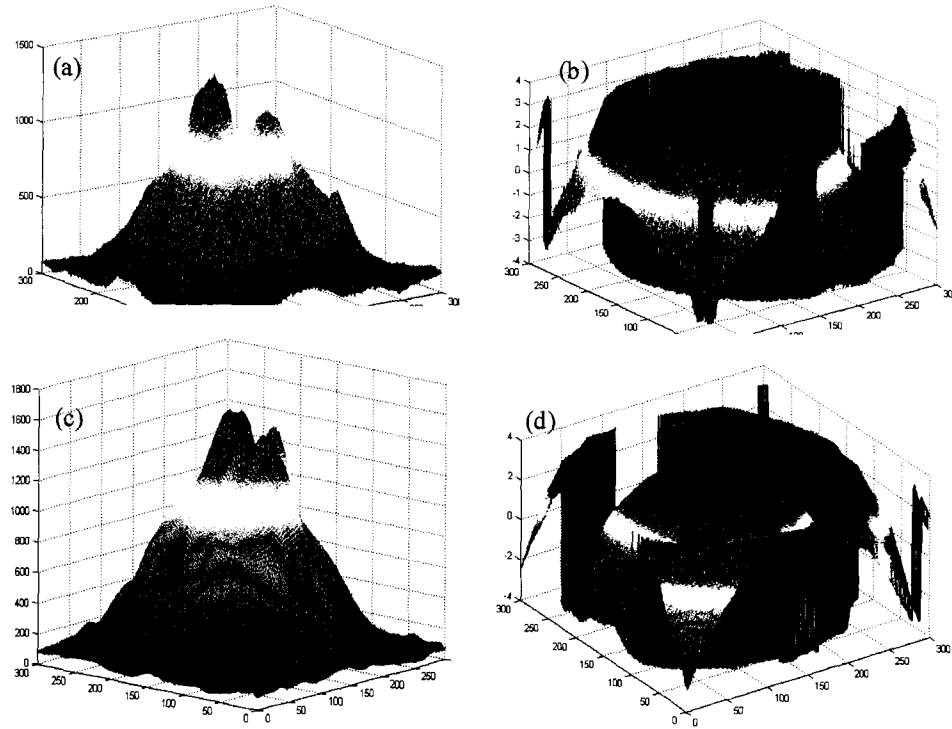


**FIGURE 13.** The measured and simulated through-transmitted field for the planar transducer case, 4.49 MHz component. Top panel: (a) measured amplitude phase profile; (b) measured phase profile; Bottom panel: (c) predicted amplitude profile; (d) predicted phase profile.

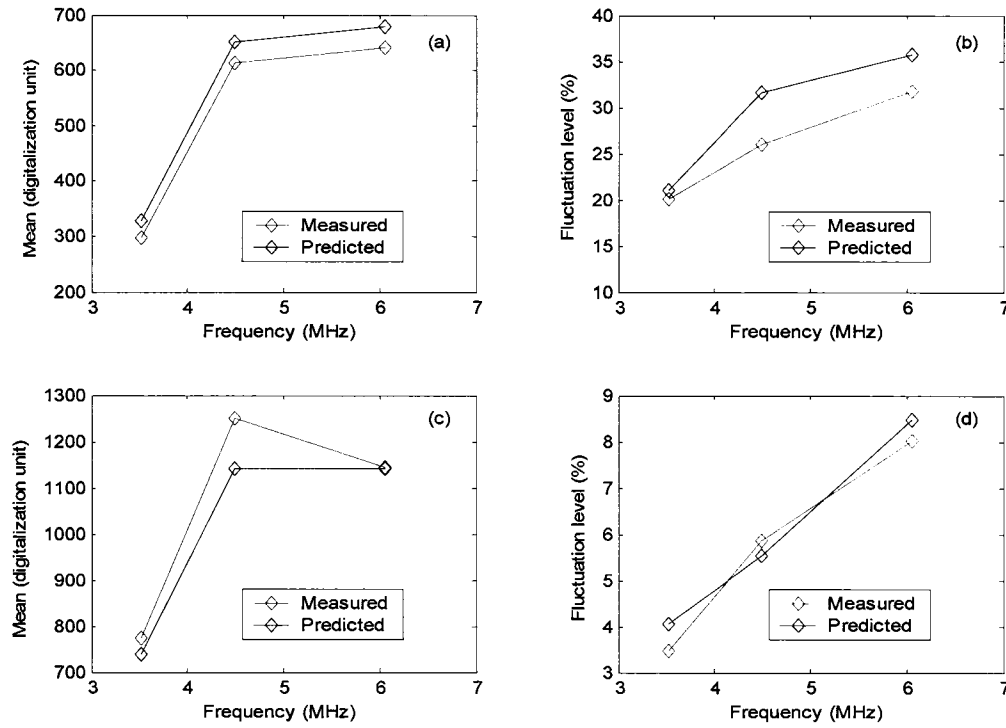


**FIGURE 14.** Back-wall signal fluctuations: comparison between experiments and predictions. (a) Planar transducer: measured and predicted mean values of the back-wall spectrum; (b) Planar transducer: measured and predicted fluctuation level of the back-wall spectrum; (c) Focused transducer: measured and predicted mean values of the back-wall spectrum; (d) Focused transducer: measured and predicted fluctuation level of the back-wall spectrum.

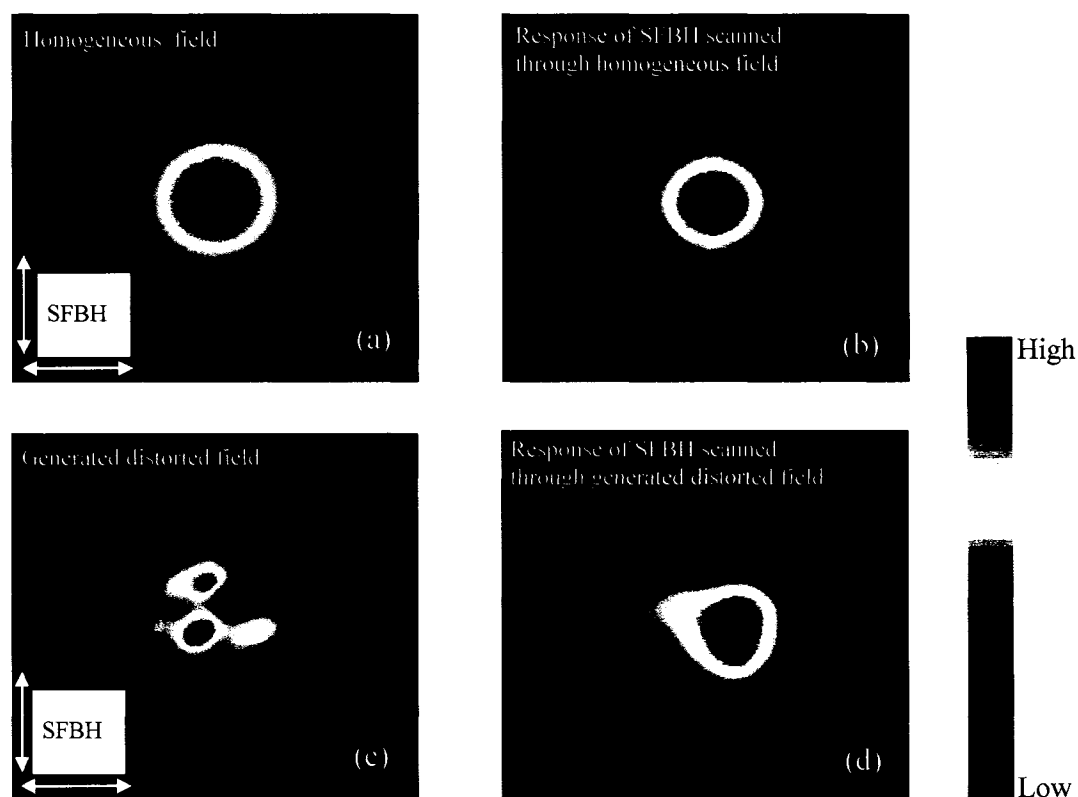


**FIGURE 15.** Flaw signal amplitude simulation for one ensemble. a). The hypothetical homogeneous field (pressure squared) and the relative size of the SFBH; b). The resulting “c-scan” image when the SFBH is scanned through the homogeneous field; c). The generated through-transmitted field (pressure square) when the inhomogeneous microstructure is present; d). The resulting “c-scan” image when the SFBH is scanned through the generated field.

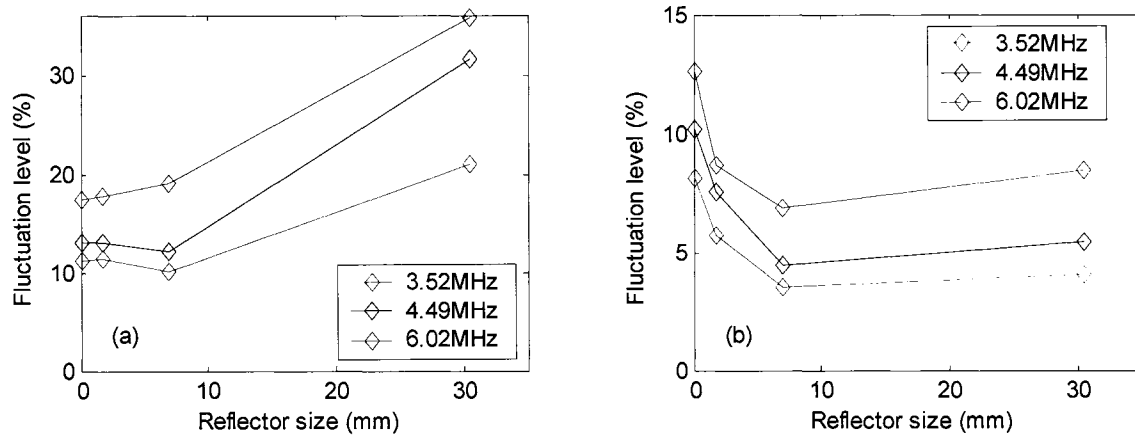


**FIGURE 16.** The fluctuation levels of small reflectors with different sizes at 3 frequencies (3.52MHz, 4.49MHz, 6.02MHz). The same data as considered for the back-wall signal fluctuation. (a) planar transducer; (b) focused transducer.

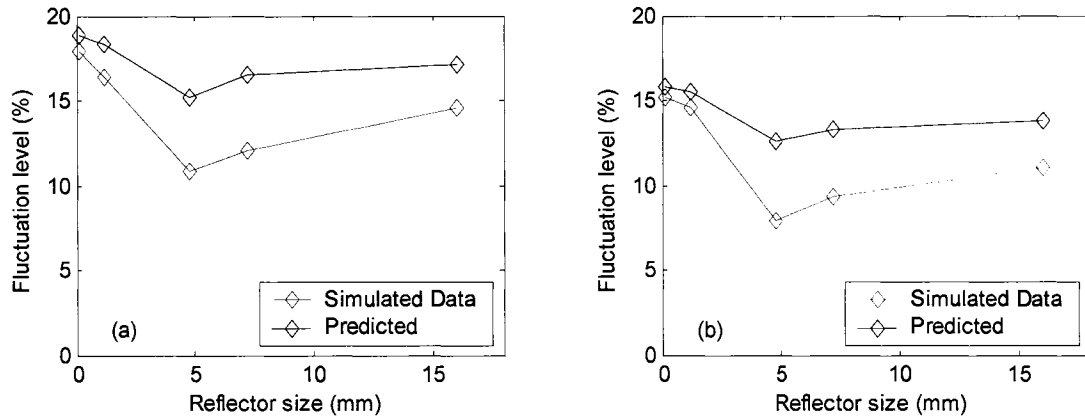


**FIGURE 17.** The fluctuation levels of small crack-like reflectors of different sizes at 5MHz. The “simulated” data are from reference [6], while the “predicted” values result from our Monte-Carlo approach. (a) the microstructure elongation is parallel to the beam propagation; (b) the microstructure elongation is perpendicular to the beam propagation.

## GENERAL CONCLUSIONS

This dissertation covers three aspects of the ultrasonic nondestructive evaluation of jet-engine titanium rotating components: the ultrasonic properties variation in Ti-6Al-4V forgings, with the emphasis on the backscattered ultrasonic grain noise; the spatial correlation of the backscattered ultrasonic grain noise; and the microstructure-induced signal fluctuations. Our research developed a more complete understanding of these problems and laid out a basis to guide the solutions that would address the deleterious effects the grain noise and beam fluctuations have on inspection.

In the part of our research presented in chapter 1, our experimental studies provided fundamental understanding of the ultrasonic properties of the titanium forging and documented the manner in which the material ultrasonic properties vary with inspection position and direction. The experimental investigation laid out a foundation to guide the development and application of improved inspection systems. This paper presented some novel ideas of how to extract useful microstructural information, such as the grain morphology and local texture, from a forging simulation software. A model is developed to correlate the grain noise signals with the microstructural variations due the inhomogeneous plastic deformation associated with the forging processing. Reasonable good agreements have been achieved. The modeling efforts provide a basis to develop algorithms to interpret the received signals, and to quantify the inspection capability, for example, to determine the POD.

In the part of our research in chapter 2, an existing backscattered grain noise theory is extended, leading to a formal theory predicting the spatial correlation of the backscattered grain noise. The theory was derived in its general form and also presented in a special form for a Gaussian beam. The theory indicates that, for a given inspection system under appropriate approximation, the material microstructure and the overlap of the incident sound

filed (both the amplitude and phase profiles) are the important controlling physical parameters for the spatial correlation of the backscattered grain noise. The theory is numerically evaluated for different experimental circumstances, and the results are compared with the measurements. Excellent agreements between the predictions and experiments are observed. This part of our research provided a theoretical tool to predict the grain noise spatial correlations at different inspection scenarios, which have important implications to the practical ultrasonic inspection.

In the third chapter, we explicitly demonstrated various beam distortion effects due to the inhomogeneous microstructure of the jet-engine titanium alloy and confirmed that the beam distortions are the physical sources of the observed fluctuations in ultrasonic signals from back surface and flat-bottom holes. Key beam distortion effects (center-of-energy drift, amplitude profile “wrinkling”, phase-front tilting and phase-front “wrinkling”) were quantified using through-transmission beam mapping techniques. An analytical relationship is derived to correlate the P/E spectrum at one transducer location to the through-transmitted field. Based on the analytical relationship, a quantitative Monte-Carlo model is proposed as a means for predicting back-wall (pulse/echo) signal fluctuations, given certain statistical variables that describe the pressure-field distortions. The model was tested and found to be in good agreement with the experiment. Following the same modeling approach, a first effort was made to simulate the flaw signal fluctuations. The simulation indicated that the fluctuation level from a small reflector depends on the microstructure, reflector size, inspection frequency and the probe focal condition in the metal. The principal contribution of this study is to demonstrate that the statistical parameters describing various beam distortion effects are physically meaningful quantities for the microstructure-induced ultrasonic signal fluctuations. How these parameters change at different experimental scenarios are to be studied in the future.